Title

Motion and Arrest of a Molten Liquid on Cold Substrates

Author

Tavakoli, Faryar

Publication Date

2014

UNIVERSITY OF CALIFORNIA
Los Angeles

Motion and Arrest of a Molten Liquid on Cold Substrates

A Dissertation Submitted in Partial Satisfaction of the
Requirements for Degree of Doctoral of Philosophy
in Mechanical Engineering

by

Faryar Tavakoli-Dastjerdi

2014

ABSTRACT OF THE DISSERTATION

Motion and Arrest of a Molten Liquid on Cold Substrates

By

Faryar Tavakoli-Dastjerdi

Doctor of Philosophy in Mechanical Engineering

University of California, Los Angeles, 2014

Professor H. Pirouz Kavehpour, Chair

Spreading of liquid drop on cold solid substrates followed by solidification involves heat transfer, fluid dynamics, and phase change physics. Coupling of these physical phenomena, although present in many industrial applications and nature, renders the physical understanding of the process challenging. Here, the key aspects of molten liquid spreading and solidifying on cold solid substrate are examined experimentally and theoretically. A novel hypothesis of spreading solidifying drops on cold solid substrates is introduced that emphasizes on early stages of the drop solidification at the solid–liquid–gas interface. The derived equations of the drop motion and arrest, stemmed from the development of the presented hypothesis, are in accord with obtained empirical results. The hypothesis is then thoroughly tested with new sets of experiments: i) Drop impact experiments, ii) Inclined plate experiments.

In addition, the solidification of static supercooled drops and the initiation mechanism of an intermittent stage (recalescence) are addressed. Also, a peculiar delay-freezing property of hydrophobic surfaces is examined under varying liquid flow rates and substrate temperatures. Moreover, a new phenomenon of cold-induced spreading of water drops on hydrophobic surfaces due to premature condensation followed by thin-film formation at the trijunction is explored and the effect of physical parameters such as relative humidity, the substrate temperature, initial contact angle, surface roughness, and drop volume are investigated. This study will significantly advance the current understanding of dynamic interaction between molten liquid and cold solid substrates.

Dedication

To my parents and my dear brother (Maziar)

Table of Contents

List of Figure

List of Tables

Acknowledgement

First and foremost, I would like to thank my advisor Professor Pirouz Kavehpour for his constructive guidance, unlimited attention, encouragement, and patience. I extend my thanks to Professor Jeff. D. Eldredge, Professor Ivan Catton, and Professor Joseph M. Teran for serving on my thesis committee. I would also like to acknowledge Professor Stephen H. Davis for his contribution and input. My experience at UCLA has been rendered more pleasant by my graduate colleagues and friends. I would like to specially thank Reza Lakeh for his friendship, Gaby for her addictive smile, Kasra for his energizing sarcasm, and my very dear friend Rommina Ghavami, whose her contributions and impact are indescribable. I wish you all the best of luck in your future life.

Last but definitely not the least, I would like to thank my beloved parents (Majid and Forough) and my dear brother (Maziar). I really hope that one day we can rejoin. They all truly sacrificed immensely for my success and well-being. I am forever indebted to them for their endless love and unwavering support. I dedicate this dissertation to them.

Vita

2008	B.S (Materials Science and Engineering), Sharif University of Technology, Iran.
2008-2010	Graduate Research Assistant, Northeastern University, Boston, MA.
2010	M.S. (Mechanical Engineering), Northeastern University.

CHAPTER 1

Introduction

The non-isothermal spreading of a plethora of different liquids over a cold smooth solid surface appears in many areas of modern industry. The studies on the subject experienced a rapid growth after the prominence of spray coating and microelectronics manufacturing. However, accurate control of the processes involving molten liquid requires further rigorous enhancement of the knowledge framework. The solidifying spreading drops on cold substrates is a multiphysics problem, including fluid dynamics and heat transfer, with a combination of strong deformations, and complicated wetting behavior at the contact line. Liquid spreading and solidification contains multitude of major challenges in scientific research and is simultaneously associated to multiple industries.

1.1 Motivation

The motivation for the study of non-isothermal spreading followed by phase change stems from variety of fields and emerging technologies. Some of the applications, which encompasses molten drop deposition and solidification processes are thermal spray coating [1], rapid prototyping [2], 3D printing [3,4], plastic electronics [5] and solder jetting in microelectronics [6]. This system is also present in geophysical flows such as lava flows and gravity currents [7], and glaciers [8]. Every application by itself considers some unique dynamics favorable. For instance, in herbicide treatment, rebound of pesticide drops should be avoided for maximum efficiency [9]. We will now discuss a few of these applications in detail.

A central application for the study of spreading and solidifying fluid bodies has been MicroElectroMechanical Systems (MEMS). For instance, an electronics surface mounting technique called flip-chip method is used to stack up multiple wafers during the final processing step to interconnect the chip pad to external circuitry. This method use neither masks nor screens. In this method, liquid solder bumps are deposited on each of the wafers. Afterwards, wafers are flipped and positioned on top of each other. Then, solder bumps get melted when exposed to hot air which results in wafers attachment. Excellent solder wetting of electrical connections is desired in the flip chip method. Factors such as tin content [10] and substrate's type [11] determine the wetting dynamics of solders in the flip-chip method.

Another applications of solidifying spreading drops are inkjet and 3D printing [3,4]. In inkjet printing, jettability of the fluid can be assessed using couple of dimensionless values relating surface tension, viscosity and density. In general, optimum fluid properties need to be maintained. For instance, surface tension should be high enough that dripping from inkjet head is prevented but low enough that the ejected droplet can break free from the printer nozzle [12]. Some of novel 3D printers, manufactured by *Z* Corporation, use standard inkjet printing technology to fabricate parts layer by layer by depositing a liquid binder onto layers of solid powder. After each layer formation, the unused powder falls down an overflow chute into a container for reuse in the next layer fabrication. Instead of feeding paper, like in a 2D printer, printer head is moved over a bed of powder in 3D printers. The inkjet head repeats this process for all of the layers of the part. Moreover, sweep deposition of molten materials can be practical to lay down insulators or conductors on a motherboard or fabricate other 3D structures [3]. In this method, small–scale objects can be accurately manufactured using micrometer diameter drops being swept across the solid surface. After deposition, drops solidify into different shapes depending on mostly thermal characteristics of the solid target. The apparent contact angle of the liquid deposited found to be an important parameter to define the solidification contact angle and thus, the final shape of the deposited drops. For instance, 3D gold micro-wire using piezoelectric inkjet printing was fabricated [4] (Figure 1.1) to be used in emerging applications of micro-heaters, micro-reactors and solar cells. In other similar studies [13,14], metallic structures were built from distinct drop deposition on the solid target. To ensure good metallurgical bonding between an impacting metal droplet and a solidified column, many parameters should be adjusted to ensure that remelting of solidified column occurs upon impact. If the temperature is much lower than the melting point, droplets will fail to fuse with it; if it is too high, the liquid flows away from the point of impact. Solidification time of each drop needs to be optimized, because long or short periods of phase change will lead to unwanted or not fully straight 3D structures.

In thermal spray coating, molten materials are sprayed on top of a solid surface. The process leads to enhanced mechanical properties and structural refinement [15,16]. In coating industry, the surface area that a drop spreads over and then stops is usually calculated by pure observation and optimized by means of trial and error from which empirical relationships have been derived. Better control of these processes and systems requires fundamental understanding of heat transfer and fluid flow that transpire during the spreading and solidification of liquid droplets.

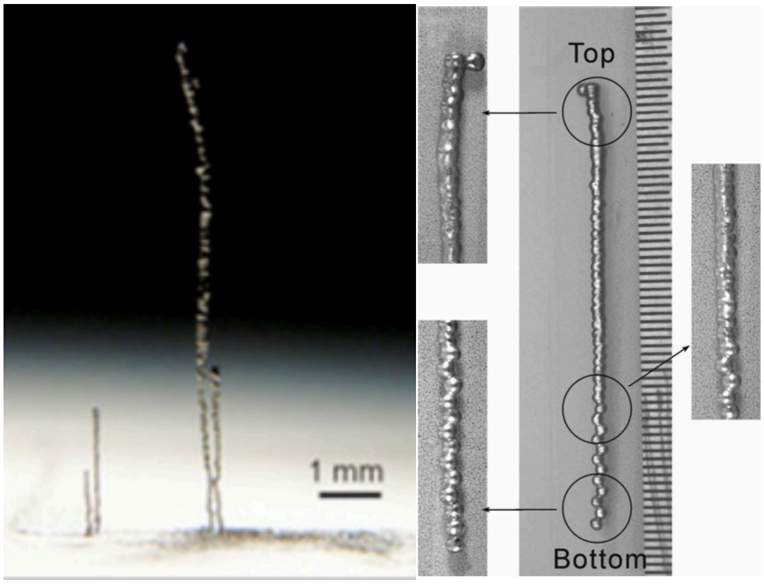

Figure 1.1: Typical shapes of printed 3D microstructures. The left picture shows printed 3D gold micro-wires[4] and the right one shows a solid column built from aluminum drops[13].

Welding is usually used to join metals by applying heat and melting the main object or a filler material. The shape of the weld pool, especially its spreading and contact angles, dictates the final quality of the welding operation [17]. From simulations and experiments [18], thermal diffusion, rather than capillary forces that dictates the dynamics, influences contact line speed of the weld pool.

In addition to practical exercises and industrial applications, the spreading and/or solidification of the drops eluded many pure scientists such as physicists and applied mathematicians through years. From scientific standpoint, the non-isothermal spreading of a liquid over a cold smooth solid surface, seemingly simple, is a complicated free-boundary physical problem characterized by the presence of a moving contact line and temperature gradients. The whole process can be governed by interplay of capillary, gravitational, viscous, thermocapillary forces, and phase change. Continuum formulation of both heat transfer and fluid flow contains singularities; from which fluid flow singularity is circumvented using appropriate ad hoc and other methods (which will be elaborated in upcoming chapters); however, some of the suggested methods avoid the stress singularity for modeling convenience with no physical interpretation. Heat flow singularity, in contrary, has not been resolved [19]. Cut-off length, beyond which continuum theory is applicable, is introduced to bypass heat flux singularity. In addition, the geometry of solidified layer ascending from the bottom of the drop is a subject of uncertainty. Planar and smooth fusion interface is usually assumed for simplicity [20-22]. However, concave interface is considered to be a realistic representation of the growing solidified layer from experiments [23,24].

1.2 Background

The spreading and solidification of liquid drops on cold substrates is a combination of fluid dynamics and heat transfer phenomena that is prevalent in the physical world. When a drop is gently deposited on a dry substrate, the process is generally driven by interfacial forces, although inertial and gravitational forces sometimes play significant roles. The unique geometric setup of liquids facilitates a variety of interesting processes. In the current research, we focus exclusively on the system of a drop being dispensed across a planar cold solid interface. More specifically, we study these systems under a low Weber (*We*) and Reynolds (*Re*) number conditions (see equations 1.1 and 1.2) where, the initial kinetic and potential energy of the drop are negligible compared to the surface energy of the interface. *Re* and *We* numbers are defined as

$$We = \frac{\rho v^2 l}{\sigma} \tag{1.1}$$

$$\mathrm{Re} = \frac{\rho v L}{\mu}\ , \tag{1.2}$$

where ρ = density, v = velocity, l = length, σ = surface tension . The Reynolds number is the ratio of a dynamic pressure, related to inertia, to a sheering stress, related to viscous effects. The Weber number is the ratio of inertial forces to surface tension forces. These parameters along with Stefan number, as thermal gradients are present, are the key factors in determining fluid flow and the subsequent arrest. The Stefan dimensionless number (*Ste*) is expressed as:

$$Ste = \frac{C_p(T_m - T)}{L_f}, \tag{1.3}$$

where C_p, T_m and L_f are specific heat, melting temperature of liquid and latent heat of fusion, respectively. T is prespreading temperature of the liquid. Stefan number scales the relative importance of the heat transfer process to phase change. In this thesis, higher value of *Ste* corresponds to colder temperature of the substrate.

Criteria are given for determining the relative effect of inertia, viscous, and capillary and these criteria are depicted in schematic maps (Figure 1.2). Each domain in a map roughly represents affecting parameters on the spreading and solidification of the contact line. Referring to one of these maps constructed by Schiaffino et al. [25], our experiments fall into the region of capillary driven inviscid flows. The mentioned map comprises four limits in (Weber (*We)*, Ohnesorge (*Oh*)) plane characterizing the impact and spreading regimes of droplets. Ohnesorge number is defined as:

$$Oh = \frac{\mu}{\sqrt{\rho \sigma a}} \tag{1.4}$$

where a is the characteristic length, typically drop diameter. Ohnesorge number signifies the relative importance of the forces that resist the droplet spreading. These four limiting lines intercept at (*We*,*Oh*)= (1,1).

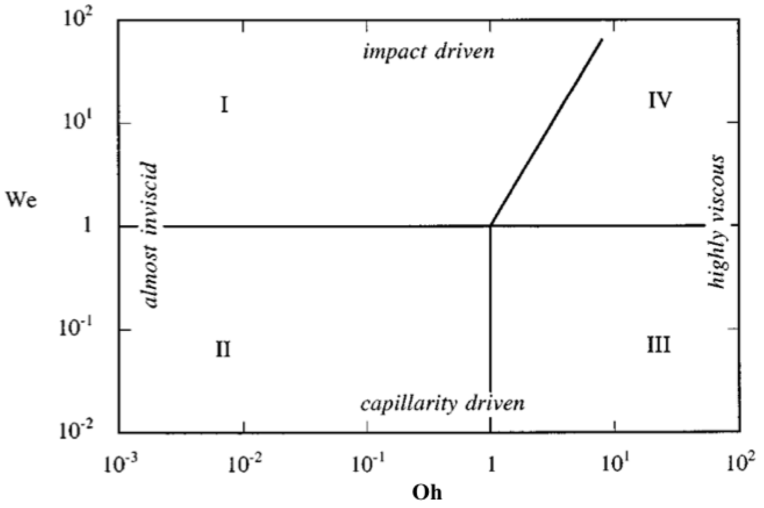

Figure 1.2: The four limits in the (*Oh*,*We*) plane displaying relative significance of governing driving and resisting forces [25].

The interaction between a drop and a solid substrate can be categorized, with respect to relative substrate's temperature to the liquid, into the following three categories: isothermal, non-isothermal spreading, and non-isothermal spreading followed by solidification.

1.2.1 Isothermal Spreading

Isothermal spreading is defined as an advancement of a liquid on a solid target at which both have the same temperatures throughout the event. Research on a droplet impact on the solid surfaces surged after the earliest investigation of Worthington [26] in 1877. This qualitative study noticed the role of surface wetting conditions on shape and flow patterns of the drops. The study also showed that increasing the velocity of the drop leads to a splash. Subsequently, unlike non-isothermal spreading of liquid followed by phase change, the impact of a droplet on solid surfaces and evolution of dynamic contact angle for isothermal spreading is extensively addressed in literature after emerging of spray technology (refer to the review paper [27]).

When the fluid advances on the solid and reaches an equilibrium condition at a specific time, a definitive contact angle is defined as an equilibrium contact angle at which three interfacial tensions are balanced out. This balance of interfacial forces is shown in a mathematical form, also known as the Young equation:

$$\cos\theta_e = \sigma_{sv} - \sigma_{sl}/\sigma \tag{1.5}$$

where σ_{sv} , σ_{sl} and σ refer to solid-vapor tension, solid-liquid tension and liquid surface tension, respectively. θ_e is the equilibrium contact angle. Classical Young equation, however, cannot explain dynamic feature of the spreading phenomenon, since advancing contact angle dynamics differs from equilibrium contact angle and the system is far from the equilibrium. Tanner [28] derived an equation to relate the contact line velocity to the dynamic contact angle. In that equation, contact line velocity is in a dimensionless form known as Capillary number, *Ca*, which shows the importance of surface and viscous forces:

$$Ca = \frac{U\mu}{\sigma} = K\left(\theta_a^3 - \theta_e^3\right) \tag{1.6}$$

where μ is viscosity, σ is surface tension, U is contact line speed, θ_a is apparent contact angle. The contact line speed may vary from less than 1 μm/s for a droplet spreading to 10 m/s or more for continuous high-speed coating processes, such as curtain coating [29]. The coefficient *K* depends on a competition between surface tension and viscosity, however it is usually considered to be a universal constant of 0.013 rad^{-3} over a wide range of conditions by Hoffman [30]. The Hoffman's law deemed universal for isothermal spreading of non-volatile liquids that completely wets the solid when permitted to spread spontaneously. This universal Hoffman curve, however, exhibits two main deviations at extremely high and low capillary numbers [31,32]. While the Tanner law predicts the late behavior of liquid spreading for viscous drops, it cannot be applied at short time scales.

Forced spreading is thermodynamically irreversible, i.e. some kind of dissipative force exerts on the system. None of the two main approaches of *hydrodynamic theory*, which considers viscous flow within the moving contact line as dissipative energy [33], and *molecular-kinetic theory* (MKT), in which atoms from the layer in contact with the surface assumed to be moving perpendicular and parallel to the surface being a source of contact-line friction [34], can fully theorize the isothermal spreading dynamics. The contrasting concept of molecular-kinetic theory deems attractive as it totally removes the mathematical stress singularity that appears in continuum theory near the contact line. Despite resolving this computational difficulty, Blake and Haynes model [34] appeared not to be fitted well to some experimental data. The limitation arises from a fact the model does not take into account viscous dissipation at mesoscopic region of contact section. In addition, from computational standpoint, simulations of drop spreading on a solid substrate are limited to tens of thousand of atom [35], which limits the time and size scale of the modeled systems.

The evolution of the wetting angle at molecular level, is governed by molecular forces, nonetheless; no relationship has been derived between macroscopic contact angle and microscopic one. Even for dynamic conditions, one simple approach, although unrealistic unless at low speeds [36], is to prescribe static values of contact line to microscopic ones [37]. In addition, the non-integrable singularity in the shear stress at the contact line results in a divergent integral for the drag force experienced by the solid entity. This singularity has often been referred to as the problem of the moving contact line by Dussan [33]. Using classical theory, infinite forces will be exerted on the solid substrate to the extent that “not even Herakles could sink a solid if the physical model were entirely valid, which it is not” [38]. This infinite forces are based on the assumption, supported by experiments [39], that contact line rolls rather than slips, which ultimately results in unrealistic physical results.

There have been some suggested alternative methods to bypass the stress singularity among which relaxing no-slip condition by imposing a slip law at the contact line on the solid substrate has been the most common method used [38,40,41]. The most common form of this condition is to assume that the velocity at wall is linearly proportional to the normal velocity gradients [38]. This can be shown as:

$$u\Big|_{z=0} = \varepsilon \frac{\partial u}{\partial z}\Big|_{z=0} \tag{1.7}$$

where u is the tangential velocity component at the surface and z is normal component. The prefactor, ε, varies for different settings of the problem and its value is zero when no-slip condition is applied. This form removes the velocity discontinuity, because the fluid slips near the solid-liquid-vapor point. Another approach to circumvent the stress singularity is to propose a thin layer (the precursor film) ahead of the contact line that wets the surface [42,43]. The thickness of this film is assumed to be less than a micrometer [44] and originated from van der Waals forces [45]. This precursor film removes the discontinuity and the supposed singularity. In this approach, no real contact angle is defined and only apparent contact angle is introduced. Some of these boundary conditions have been imposed for modeling convenience rather than relation to any justifiable physical theory.

Overall, it is unwise to draw definitive conclusions on the origins of dynamic contact angle from experimental results of contact angle measurements and computational results. In addition, to this main uncertainty regarding contact angle in isothermal spreading, factors such as humidity [46], size of solid substrate [47], annealing temperature of some metallic substrates [48], cleanness of the solid substrate [49], and atmospheric chemistry [50], which are not incorporated in the Tanner law (equation 1.6), affects the spreading dynamics.

1.2.2 Non-isothermal Spreading

The heat and fluid flow occurring during the spreading of a liquid droplet on a cold/hot substrate are neither typical, nor easy to examine experimentally. In addition, the coupling between heat transfer and fluid dynamics and the fact that dynamic wetting operates on scales ranging from macroscopic to molecular are only a few of the factors resulting in incomplete comprehension of this phenomenon.

The first work [51] on non-isothermal thin-film liquid flow taking vapor recoil, mass loss (or gain), thermocapillary, surface tension, and rupture instabilities into consideration is conducted by Burelbach et al. They concluded that the interactions among viscous forces, thermocapillary, and hydrostatic effects cause dimpling of the interface when a drop is heated nonuniformly from below. Ehrhard and Davis [52,53] investigated the non-isothernal spreading of droplets on a heated or cooled solid target without any consequent phase change. Ehrhard's work [52] experimentally confirmed the influence of thermocapillary effects on the evolution of spreading drops. When the solid substrate is heated, an interfacial flow is established from the contact line towards the droplet center that decreases the final equilibrium radius of the droplet as compared to isothermal case. On the other hand, a cold solid substrate induces an interfacial flow from the droplet center to the contact line that increases the final equilibrium radius. In another work of Ehrhard [53], it is found that gravitational forces dominate the non-isothermal spreading at longer times, whereas at shorter times, capillary forces control the spreading. Krahl et al. [54] confirmed the previous assertions and noted that for a cold liquid meniscus spreading over a hot solid wall, the contact angle apparently becomes significantly larger. Kabova et al. [55] numerically analyzed the thin film thickening on a heated inclined surface under linear dependence of viscosity and surface tension to temperature and reaffirmed the previous conclusions. The aforementioned studies unanimously support the dependence of the liquid spreading extent to the substrate temperature.

1.2.3 Non-isothermal Spreading Followed by Phase Change

Little experimental work has been done on the evolution of drop's apparent contact angle and base diameter when solidification is involved. Of those experiments, few results are available for the conditions of interest to us, that is for the slow deposition and solidification of liquid droplets. From theoretical standpoint, equations of continuity, energy of solid and liquid, and Navier-Stokes should be solved to provide accurate description of the process. The precise answers to the aforementioned equations are practically impossible due to the presence of multiple parameters, such as conduction through a contact resistance, deforming geometry of drops, solid-liquid transformation, and two distinct singularities. The two mathematical singularities at the contact line are introduced by fluid dynamics [45] and heat flux [19]. No theoretical mechanism has been suggested to circumvent the heat flux singularity at contact point and immediate adjacent region, unlike stress singularity. Schiaffino and Sonin [56] investigated the characteristic length at which an unknown physical mechanism bypass the heat flux singularity, and proposed the cut-off distance that brings their continuum theory into agreement with experimental results. Numerical simulations of simple solidification on a static 2D liquid droplet cooled from a point with different conditions at the trijunctions have been conducted by Ajaev and Davis [57,58]. Higher solidification rates are found for lower surface tension and larger solid-to-liquid conductivity ratios.

Subsequent to studying the solidification of the static drops, scholars progressed to investigate more complicated situations at which the solidification rate does not inhibit drop phase change, as it is then sufficient to solve only equations of fluid motion, considering that freezing starts only after it has come to maximum diameter [59]. The first analytical study considering both simultaneous fluid flow and solidification in quenching metal droplets has been done by Madejski [60]. His solidification model is taking viscous energy dissipation and surface tension into account. He asserted that spread factor depends upon Weber, Reynolds and Peclet numbers. His main assumption is that solidification starts at the moment of impact, without contemplating superheating and supercooling. Most crucially, the effect of surface wetting and advancing contact angles is neglected. Similarly, Pasandideh-Fard et al. [61] studied the impact and solidification of tin drops on a homogenous stainless steel using both experiments and numerical modeling. A complete numerical solution using the Navier-Stokes and energy equations was used to model the process. The measured values of contact angles from the experiments were used as a boundary condition for the numerical model. Accurate information on contact resistance is required for modeling maximum splat diameter. The effect of droplet solidification on the maximum spread diameter is determined by assuming that all kinetic energy stored in solidified layer is lost. Simpler model without considering viscous dissipation was derived by Watanabe et al [62]. They proposed that the solidification of a drop occurs after the droplet deformation, regardless of its initial values. The solidification time is two orders of magnitude higher than the deformation time. We should also note that to date, all solidification models assume the solidification occurs at melting temperature. Haferl et al. [63] numerically investigated impingement of molten solder drops onto smooth metallic surfaces in a reduced gravity environment to present information on fluid dynamics and heat transfer phenomena. It is mentioned that accurate comparison between numerical and experimental values of solidification times is not feasible, as visual determination of the solidification start is practically complicated.

The spreading of liquid droplets followed by phase change is retarded by two proposed theories. One occurs by freezing at the wetting line [64,65], and the other by the kinetic energy loss due to solidification, usually for impact experiments [61,66]. The latter effect found to be negligible if $\sqrt{Ste/\mathrm{Pr}} \ll 1$, where *Pr* (Prandtl number) is the ratio of momentum diffusivity to thermal diffusivity. Moreover, the effect of solidification at high *We* (~400) on spreading dynamics was questioned and the slight decrease in arrest diameter was attributed to surface tension [67]. The main questions arising in spreading and solidifying drops are: i) At what point will the molten wetting line stop and, ii) what would be the solidification contact angle.

Gao and Sonin [3] reshaped an ink-jet printer to dispense wax molten droplets on a dry cold target. It was postulated that as long as solidification completes much slower than spreading and the drop first establish a quasi-equilibrium shape, the solidification contact angle is a function of liquid, solid materials and substrate temperature. Attinger et al. [64] have presented the transient fluid dynamics and wetting of the novel solder jetting technology on the solid substrate. Their results suggest that solidification time depends non–monotonically on the substrate temperature. At lower *Ste*, the spread factor (ratio of final diameter to droplet diameter) was practically independent of the substrate temperature, however at higher *Ste*, spread factor was decreased. For molten paraffin wax droplets on aluminum surface, Bhola and Chandra [66] observed that arrested contact angle at relatively low *Ste* equals equilibrium contact angle, while larger contact angle and smaller footprint were formed at higher *Ste*. Increasing impact velocity and *Ste* were also found to promote droplet fragmentation. Droplet recoil was observed and attributed to surface tension pulling back the splat. In another study on the solidification contact angle of the molten micro-sized wax drops by Li et al. [68], the solidification angle decreased with increasing the solid target and drop temperatures. They found that applying thin layer of oil to the substrate surface increases equilibrium contact angle, but solidification contact angle is controlled by the resistance of the oil layer to the motion of the droplet contact line.

The only, and most recent, work comparatively analogous to ours is carried out by Schiaffino and Sonin [25,65]. Using a variety of fluids, they conducted low Weber deposition experiments looking into effects of different parameters on post-solidification shape of droplets. Small liquid droplets were manually released (controlled frequency) from a microliter syringe and allowed to fall onto a cold substrate temperature. They were only concerned with the *homologous* problem where the liquid and solid target are of the same material, simplifying that the liquid and solid phases have approximately the same specific heat, thermal conductivity, and density. Molten droplet deposition was investigated by dropping water on ice, liquid wax on solid wax, and mercury on frozen mercury. Prior to arrest, the relationship between the melt's apparent dynamic contact angle and contact-line speed appears to obey the Tanner-Hoffman law [28,30].

Most importantly, location of solidification initiation and dynamic growth front was assumed to originate from the basal plane of the liquid drop covering the trijunction (Figure 1.3). They contend that the moving drop stops spreading when the solidification front angle (θ_s) approaches the apparent dynamic angle (θ_0). When the solidification contact angle is near the value of the apparent contact angle, the spreading rate drastically decreases, and ultimately stops. θ_s is determined by the difference between the metling temperature and the temperature of the target over which the spreading occurs [56]. The assumption of basal solidification has been proposed for more viscous flows of lava and gravity currents [69,70]. Even for water, basal solidification is postulated when the substrate is permeable and porous [71], however, in none of theses studies, the basal solidification has been verified experimentally.

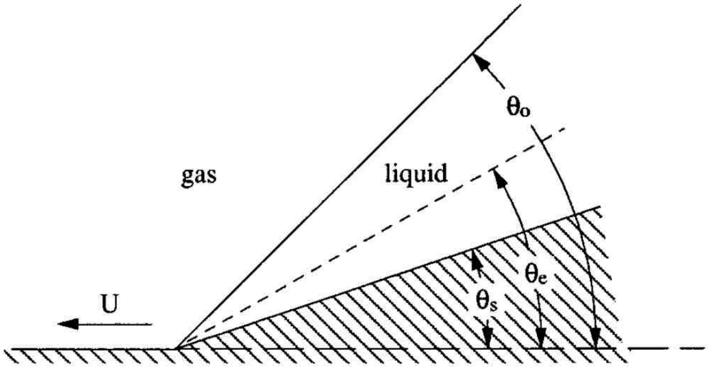

Figure 1.3: Suggested contact-line region in a melt advancing over a cold solid target [25]. The solid substrate temperature is lower than the fusion temperature of the liquid. θ_s is the solidification front angle, θ_0 is the liquid's apparent dynamic angle, and θ_e is the equilibrium contact angle.

For a given material, the relationship between the spreading factor, the dimensionless ratio between arrested footprint to the drop initial diameter (R^*/a), and Stefan number (*Ste*) was established empirically. R^*/a was found to be inversely proportional to the one-third power of *Ste* (Figure 1.4),

$$R^*/a \approx C.S^{-1/3} \ . \tag{1.8}$$

In the case of droplet deposition on materials of its own kind, provided that contact angle is neither close to zero nor to π. This relationship between arrested base diameter and *Ste* was also corroborated by experimental results of Duthaler [72]. The prefactor (*C*) is a function of physical parameters.

The basis for using power law equation for explaining the obtained empirical data is not physically justified, nonetheless, limiting behavior of the arrested footprint with *Ste* is mentioned as a reason for using the power law relationship.

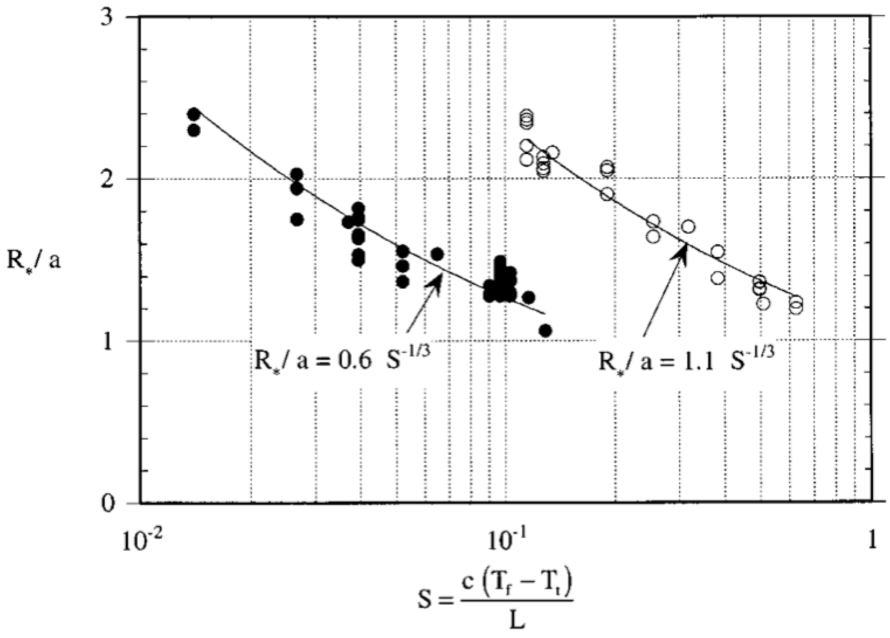

Figure 1.4: Correlations of dimensionless arrested base diameter $\left(R_*/a\right)$ to Stefan number (S) for water on ice and mercury on frozen mercury [25].

From geometrical relations and D^* versus *Ste* equation, an implicit equation was derived for θ^* in terms of *Ste*, however this equation was not fitted to their obtained data. Instead, the data for microcrystalline wax was fitted with the power law $\theta^* = 85S^{1/2}$, assuming that arrested contact angle is zero when $Ste \to 0$. A necessary condition for their analysis to be valid is for the drop to take spherical final shape.

The extent, at which different physical parameters is believed to influence the outcome of the solidifying spreading drops, is still divided between researchers. For instance, thermal contact resistance and convection in the droplet are usually neglected; nonetheless, some studies [73,74] suggest that thermal resistance changes significantly during solidification. Moreover, melt superheat appeared to play a minor role in determining post-solidification shape of the drop; however, other studies [75,76] find the effect of melt undercooling on spreading and solidification time to be tangible. For a droplet with large initial undercooling, the solidification took place at the faster rate than the melt spreading, which resulted in a spherical shape of final splat.

1.3 Thesis Organization

The remainder of the thesis is as follows. Chapter 2 addresses the experimental procedures and setup used for different experiments throughout this thesis. Moreover, the judicious method employed to evaluate the drop geometry during experiments is explained. Chapter 3 presents data on the isothermal liquid spreading on the glass substrates from the liquid source followed by scaling analysis of the data, which sets the stage for chapter 4. Chapter 4 addresses the experiments of spreading and solidification of liquid drops on cold solid substrates. In this Chapter, a new hypothesis regarding the origin of the initial solidified region is introduced. The hypothesis, then, is further developed to derive principal equations using dimensionless analysis and scaling. The obtained governing equations are compared to the empirical data. Our working hypothesis is then thoroughly tested in new set of experiments. Chapter 5 addresses the peculiar, yet still questionable, freezing-delay effect of hydrophobic surfaces on water liquid. Forced spreading of water on cold hydrophobic surfaces are performed and compared to freezing timescales on the hydrophilic surfaces. Chapter 6 sheds some light on a intermittent solidification stage of supercooled drops, also known as the recalescence, on cold solid targets. In Chapter 7, new phenomenon of cold-induced spreading of static water drops on hydrophobic surfaces, initiated by negative temperature gradients, is reported and the potential effects of different physical parameters are explored. Chapter 8 summarizes the thesis's most momentous conclusions and suggests some future work topics. Chapter 9 lists all of the references used in this thesis.

1.4 Thesis Objective

A few previous works on advancing molten contact line on cold substrates, show a strong relationship between the dynamics of the drop and some other physical parameters such as the substrate temperature, liquid viscosity, surface tension, and etc. Arbitrary physical equations are fitted to the empirical data obtained, but could not be related to any physical theory, considering the nature of the solidified layer postulated. In addition, two singularities of heat flux and fluid continuity makes the accurate solving of the problem physically unfeasible.

The main portion of this thesis is devoted to gain more insight on moving molten contact line followed by phase change on cold substrates and fill the gap between empirical data and the physical theory. We focus on providing a practical description of the spreading behavior followed by arrest and solidification conditions. This study is both experimental and theoretical in scope. We start by executing experiments of spreading solidifying drops and continue by presenting a novel hypothesis. The hypothesis focuses on near contact-line physics of the drop at early stages of the solidification. We further develop and rigorously test our hypothesis in new set of experiments and assess the results to identify whether the hypothesis still holds or get rejected. Experiments of supercooled drops on solid substrates and deviation of the outcome from other liquids provided incentive to examine the reason behind it. Furthermore, we found out that there exists intermittent stage of freezing which dictates time to freezing initiation of solidifying supercooled drops. Initiation and mechanism of this stage are further explored. Later in the thesis, the debated effect of hydrophobicity on freezing-delay is tested and different controlling regimes are defined. Finally, new phenomenon of temperature–induced spreading of static water drops on cooling hydrophobic surfaces is observed and various physical parameters such as the substrate temperature, relative humidity, surface roughness, liquid materials and drop volumes are investigated to recognize the principal mechanism.

CHAPTER 2

Materials and Methods

Physical parameters to be studied need to be accurately controlled and isolated to enable us to answer the current questions regarding the liquid drops spreading on cold solid substrates. To efficiently collect data and confidently interpret them, clear and organized experimental procedure needs to be planned. In this chapter, experimental procedure and set up are listed and elaborated.

2.1 Experimental Procedures and Materials

We focus on providing a practical description of the spreading behavior followed by arrest and solidification conditions. Two goals were kept in mind, while conducting our experiments. First, the series of materials used would have to be such that their properties would have to be identical apart from one or two variable that could be manipulated. This would allow us to parametrically study the effect of whatever property we thought was important. After preliminary research and experimentation, we decided that our fluids would be deionized (DI) water and a series of alkane hydrocarbons. These alkane hydrocarbons have similar physical properties except their melting points. A table of liquid used and their relevant properties is shown in Table 1. Latent heat and thermal diffusivity of the alkane hydrocarbons are acquired from [77]. For our solid targets, microcover glasses and copper sheet from VWR are used. The thermal properties of the solids used are listed in table 2. Multiple references [77-80] are used for the values in the table.

Secondly, it was our goal to make the experiments as reproducible as possible. In order to achieve this goal, extra care was taken in the way instruments were cleaned and the contamination of fluids and the substrates used was kept as low as possible. Since all of our proposed experiments dealt with surfaces, it was important to keep all materials free of foreign chemicals and residues, such as oils from our hands, and foreign objects, such as dust, both of which can cause significant changes in the surface tension and ultimately the outcome of the experiments.

The surface tension of fluids, σ, was measured using the DuNoüy ring method using a force tensiometer (K100, Krüss). The K100 force tensiometer performs high-precision, automatic and reliable measurements of surface tension. The surface tension resolution of K100 is 0.01mN/m. In the DuNoüy ring method, the liquid is raised until contact with the ring-shaped probe is registered. For every experiment, the ring was successively rinsed in acetone, methanol and, water, and then the ring was heated using bernzomatic micro flame butane torch until red-hot. We waited for the measuring probe to cool for approximately five minutes before each measurement. This probe is made of platinum-iridium and is attached to a precision balance (Figure 2.1.a). A force acts on the balance as soon as the probe touches the liquid surface. The sample is then lowered again so the liquid film produced beneath the ring is stretched. As the circumference of ring is known (ring diameter = 1.85 mm), the forced measured is used to calculate the surface tension of the liquid. In practice, the distance between the liquid surface and the ring is increased until the maximum force is reached (Figure 2.1.b). Then, calculation of surface tension is made according to the equation:

$$\sigma = \frac{F_{\max} - F_b}{W.\cos\theta} \tag{2.1}$$

where F_{max} is the maximum force, F_b is the weight of the liquid lifted, W is wetted circumference of the ring, and θ is the contact angle between the ring and the liquid. All of the surface tension measurements were performed at room temperature.

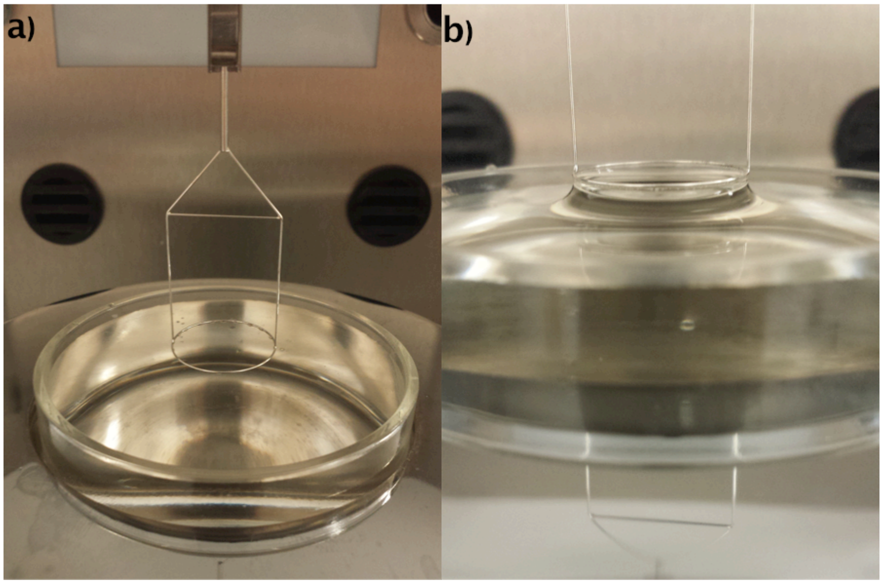

Figure 2.1: K100 tensiometer with the DuNoüy ring a) attached to the clamping spring just prior to the experiments, b) in contact with the liquid surface during the experiment.

Table 1: Properties of the fluids used in the solidifying spreading experiments. Surface tension values were measured directly with Krüss K100 tensiometer. For the other values in the table, multiple references [77-80] are used.

Fluid	**Density (kg/m^3)**	**Absolute Viscosity (kg/m.s)**	**Surface Tension (N/m)**	**Latent Heat (J/kg)**	**Specific Heat Capacity (J/gr.K)**	**Thermal Conductivity (W/m.K)**	**Melting Point (°C)**
Water	1000	1.00×10^{-3}	71.7	3.3×10^{5}	4.18	0.561	0
hexadecane	773	3.34×10^{-3}	29.23	2.29×10^{5}	2.31	0.21	18.6
pentadecane	769	3.70×10^{-3}	25.90	2.05×10^{5}	2.23	0.17	9.9
dodecane	780	1.34×10^{-3}	25.35	2.16×10^{5}	2.20	0.21	-10

Table 2: Thermophysical properties of the solids used. Values for microcover glass are from the VWR manufacturer and for copper are from [81].

Solid	Thermal Diffusivity (m^2/s)	Density ($kg/m^{3)}$	Latent Heat (J/kg)
Microcover Glass	8.4×10^{-7}	1800	N/A
Copper (99%)	1.16×10^{-4}	8933	1.76×10^{5}

A commercially available instrument, DSA100 Krüss GmbH, was used for recording the droplet spreading dynamics and subsequent evaluation. In principle, the DSA 100 machine consists of three main components:

- The specimen table with three manual knobs for accurate 3D positioning
- The video system with CCD camera, prism, light source and aperture
- A software-controlled multiple dosing unit

Actual image of the apparatus is shown in Figure 2.2. The more detailed schematics of the DSA is shown in Figure 2.3. This state-of-the-art apparatus provides accurate measurement of the dynamic contact angle and base diameter of the spreading fluid. The intelligent dosing system of DSA 100 permits liquids to be dispensed without the risk of contaminating the sample. The bright light with extremely low radiated heat provides us with the illumination that is required for measuring drop's evolution. This new type of light guidance eliminates all interference by unrelated light making the drop shape recognizable by DSA 100 software. The drop is illuminated from one side and a camera at the opposite side records an image of the drop.

In our experiments, a glass slide with dimensions of $50\times24\times0.15$ mm^3 (VWR microcover glass) was rinsed successively in acetone, methanol and DI water. For some cases, when needed, glass slides were cleaned with plasma cleaner. Plasma cleaning automatically and quickly removes organic contamination. Oxygen (O_2) plasma reacts with molecules deposited on the surface of the substrate, breaking them down, and turning them into volatile compounds. After being dried on hot plate, the glass slide was placed into a Krüss drop shape analyzer chamber, in which temperature and relative humidity are accurately controlled. The horizontality of a stage was carefully checked before the droplet spreading experiments using a level. A glass window covered three sides of the chamber and provided the observation porthole for CCD camera and illumination source. We are not concerned about the surface roughness of the glass substrate, because roughness of glass substrate is assumed to have negligible effect on arrest parameters, as long as characteristic angles are smaller than arrested and dynamic contact angles [72]. Even reported roughness increase caused by solution cleaning of glass substrate, although for 2 hours, is not in the order of magnitude of solidified contact angles [82].

Temperature of the solid targets can be adjusted by a Peltier element situated in DSA100 machine from -30 °C to 160 °C. A Peltier element is a thermoelectric device, which transfers heat from one of its sides to the other when electricity is applied. The cold side is then brought in contact with the substrate and cools it to a chosen temperature before or after, depending on the experiment, the water droplet is placed on it. Cooling rate is kept fairly constant by circulation of coolant water with predetermined temperature around the hot side of the Peltier element. Temperature readings of the Peltier element were accurate to ±0.5 °C established by FLIR® SC300 thermographic camera and k-type thermocouple. Humidity can be changed from 5 to 80% RH by humidity chamber located at the back of the stage which adjusts the inflow of nitrogen gas. At high relative humidity, condensation could occur on the viewing and measuring window below room temperature. In order to prevent condensation, the assembled tube connections are used to direct a stream of air through the chamber and past the windows. The main stage, on which the Peltier element and glass substrate are situated, can be moved in x, y and z directions. High-speed camera is used as a visualization technique to study droplet spreading dynamics and phase change. The camera is capable of recording each event with maximum of 89 frames per second with resolution 780×580 pixels. The camera can be aligned at an angle from +4° (above the surface) to -4° (below the surface) to the horizontal. In this thesis the viewing angle was set to +1°, unless otherwise stated.

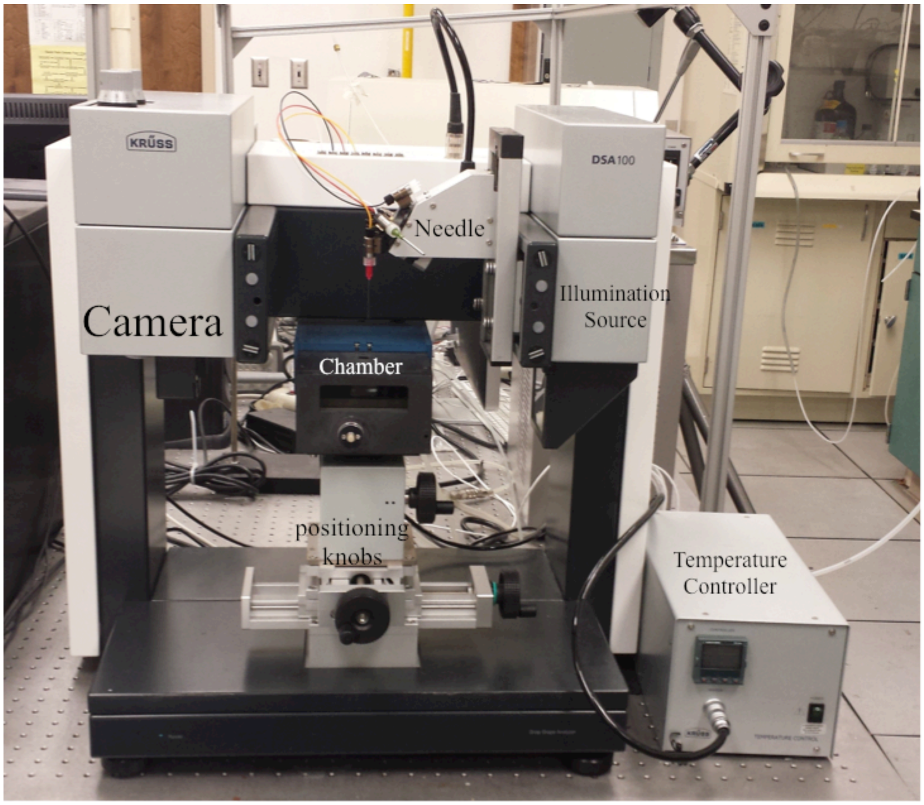

Figure 2.2: Drop Shape Analyzer (DSA100) by Krüss. This unit consists of a camera, illumination source, dosing unit, sample table, prism, peltier element, and temperature controller.

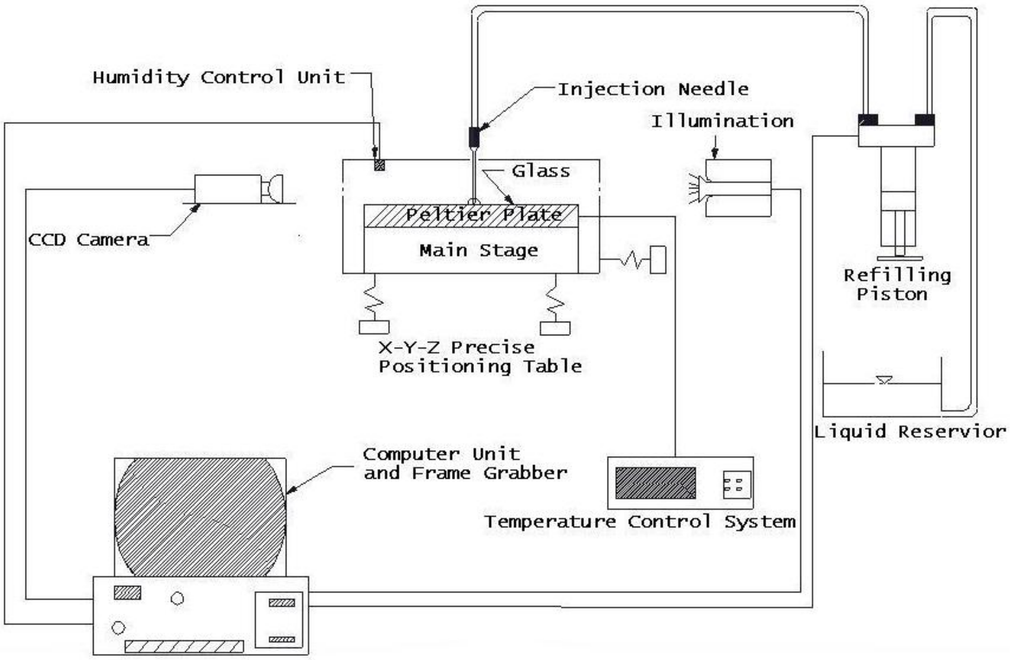

Figure 2.3: Schematics of continuous liquid spreading apparatus (DSA100). All of the affecting variables, such as the substrate's temperature, humidity, and liquid flow rate, except the stage positioning, can be controlled automatically via the DSA software.

The syringe driver unit conducts the dispensing of the liquids in two steps. In first step, a syringe plunger extracts liquid from the storage bottles and stores it in a secondary cylindrical containment in a downward motion. In the next step, liquid is pushed through the tubes by the same plunger and to the injection needles. The injection syringe is attached to a syringe revolver is can be brought down either manually or automatically entering a hole from a top of the chamber close to the glass substrate. The hypodermic needles used are flat tipped, with inner diameters of 0.51mm or 1.8mm. The distance between the injection needle and the glass substrate during liquid unloading was kept constant and relatively high in the upper region of the drop so the needle does not alter the shape of the drop substantially. The needle temperature was not changed significantly during the injection process. This was established by attaching an external k-type thermocouple (chromel–alumel) to the side of the needle tip during spreading of molten liquids. Continuous dispensing of a liquid is performed when the needle is brought close to the solid substrate with flow rates ranging from 0.2 µl/min to 600 µl/min.

2.3 Evaluating the Drop Geometry

The basis for the determination of the contact angle and base diameter is the image of the drop on the solid surface. In the DSA program, the actual drop shape and the contact line with solid are first determined by the analysis of the grey level values of the image pixels, i.e. the software calculates the root of secondary derivative of the brightness levels to acquire the point of greatest change of brightness. A mathematical model, which is used to calculate the contact angle, is adapted to fit the drop shape. The various methods of calculating the contact angle differ in the mathematical model used for analyzing the drop shape. Either the complete drop shape, part of the drop shape or only the area of phase contact is evaluated. All methods calculate the contact angle at the intersection of the drop contour line with the solid surface line. The base diameter and contact angle of the liquid drops at each frame are measured by DSA100, mostly, using a tangent-2 method, also known as the Polynomial method. In this method, a profile of sessile drop in the region of the baseline is fitted to polynomial function. The polynomial function is of the type of $y = a + bx + c\sqrt{x} + d/\ln x + e/x^2$, where a, b, c, d, and e are fitting parameters. From the fitted parameters the slope of the three-phase contact point at the baseline is first determined and used to determine the contact angles. As in this method, only baseline part of the drop is analyzed, this method is suitable for dynamic contact angles. Consequently, the base diameter is defined as a distance between to contact points. This method, however, is susceptible to heterogeneity and image quality at the trijunction. Especially, for our case where the condensation and frosting around the trijunction are possible, extra care needs to be taken. In general, repeat measurements of a contact angle for a given drop image, except in the presence of condensation and frost accumulation at the trijunction, were all within ±0.2.

For evaluation of the drop height and volume, tangent-1 method, also known as ellipse method, is used. In this method, the complete profile of a deposited drop is adapted to fit a general conic section equation. The derivative of this equation at the intersection point of the contour line with the baseline gives the slope at the solid-liquid-gas point and thus the contact angle. Before the drop evolution videos or images are taken, a criteria for scale is needed to identify the dimension of the spreading liquid. For this purpose, outer diameter of the injection needle is used to calculate the scale factor and hence compute the dimensions of spreading liquid. The contact angles shown in this thesis are the average of right and left contact angles measured by the software, unless otherwise is specified. Figure 2.4 shows a frame from the side view during forced spreading of water liquid on a glass substrate. The values of right (CA[R]) and left (CA[L]) contact angles at each frame are shown at top left. The black vertical solid line is the 0.51 mm diameter injection needle. White region in the water drop is the passing light from the illumination source.

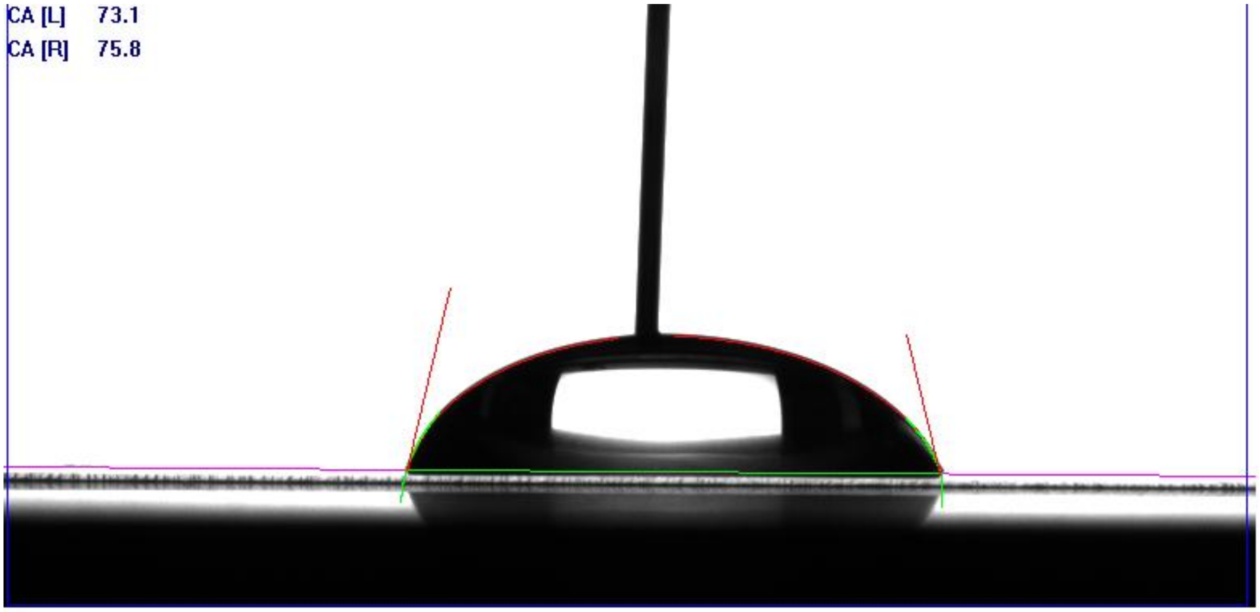

Figure 2.4: A frame from the video recording of the liquid spreading under constant flow rate on a glass substrate. At each frame, two apparent contact angles were measured using tangent method 2, and the average of these two was taken as an apparent contact angle. The base diameter is then measured between the two intercepts. The values of right (CA[R]) and left (CA[L]) contact angles at each frame are shown at top left. The black vertical solid line is the 0.51mm diameter injection needle.

CHAPTER 3

Isothermal Spreading

A significant body of literature studied the isothermal spreading of liquid on solid substrates, in which both the solid and liquid are held at constant and equal temperature above the melting point of the liquid. These works sought to devise an equation to explain the relationship between apparent contact angle and the speed of the contact line. The Hoffman–Tanner law [28,30] is generally accepted to be universal in explaining the relationship. For the spreading of a single drop, assuming that the drop follows Tanner law and applying volume conservation, the dynamics behavior is predictable, nonetheless, further formulation is required to explain the behavior under other conditions such as forced spreading.

In this Chapter, we try to formulate the forced spreading of liquid from the source onto the solid substrate, which is a prerequisite for understanding the non-isothermal spreading. We are using scaling analysis to derive an equation for the drop base diameter as a function of time.

3.1 Results and Discussion

Before studying the effect of solidification and temperature gradient on liquid spreading, a simple case of isothermal forced spreading of water was carried out. Figure 3.1 shows spreading diameter of water as a function of time in a log-log grah at flow rates of 5 µl/min, 25 µl/min, 50 µl/min, 100 µl/min, 200 µl/min, and 600 µl/min at 25 °C. At any given time, the base diameter of the drop is larger for higher flow rates. For all of the experiments, especially at flow rate of 600 µl/min, fingering and asymmetrical spreading of the liquid are observed at later stages. At long enough times, the drops do not maintain their circular shape and three-dimensional instabilities become distorting, as the drop's leading edge (very thin liquid film) approaches the lengthscale of the surface roughness. Figure 3.2 shows a video sequence of water forced spreading on a glass substrate under constant flow rate of 100 μl/min from side view. Movement of the contact line is fairly smooth with no signs of extreme stick-slip. In addition, water spreading under forced conditions in our experiments is axis-symmetric; however, minor fingering at larger timescales is observed.

Assuming that a sessile drop during spreading takes a spherical cap shape, a drop volume can be related to the droplet radius and contact angle as follows:

$$V(t) = D^3(t) f(\theta) \tag{3.1}$$

where for $\theta < \pi/2$, $f(\theta)$ is:

$$f(\theta) = \frac{\pi(1-\cos\theta)(2+\cos\theta)}{3\sin\theta(1+\cos\theta)} \tag{3.2}$$

where V is the drop volume, D is the drop diameter and θ is the contact angle. For $\theta < 65°$, $f(\theta)$ can be approximated by θ. This inequality prevails in our experiments. We posit that contact line follows the Tanner-Hoffman law [28,30]:

$$Ca = \frac{\mu U}{\sigma} \propto \theta^3 \tag{3.3}$$

On the other hand, for our case of constant flow rate from the injection needle:

$$V(t) = Qt \tag{3.4}$$

Where $V(t)$ is a volume of a spreading drop, Q is flow rate, and t is the duration of liquid spreading. Assuming that the contact point velocity (U) scales with the first derivative of radius over time (R/t), according to these equations, a general power scaling law for forced spreading of wetting liquid on a solid substrate can be derived as:

$$R \propto t^{0.4} \tag{3.5}$$

The experimental data in the Figure 3.1 were fitted according to

$$D(t) = At^{B} \tag{3.6}$$

where A and B are the power fitting components. The average value of B from all of the fitting lines (solid lines) equals to 0.388±0.007, which is in good agreement with theoretical derivation presented especially at later stages of liquid spreading. However, discrepancies at early stages of spread can be attributed to handling and positioning of injection needle, which have tangible influence on the spreading dynamics especially on advancing contact angle. The value of A increases with higher flow rates from 0.82 for 5 μl/min to 4.50 for 600 μl/min. Starov et al. [83] also considered the spreading of liquids over solid substrates with a liquid source at the center of the drop, both from theoretical and experimental standpoint, and obtained the same power value (0.4) for liquid spreading using lubrication approximation.

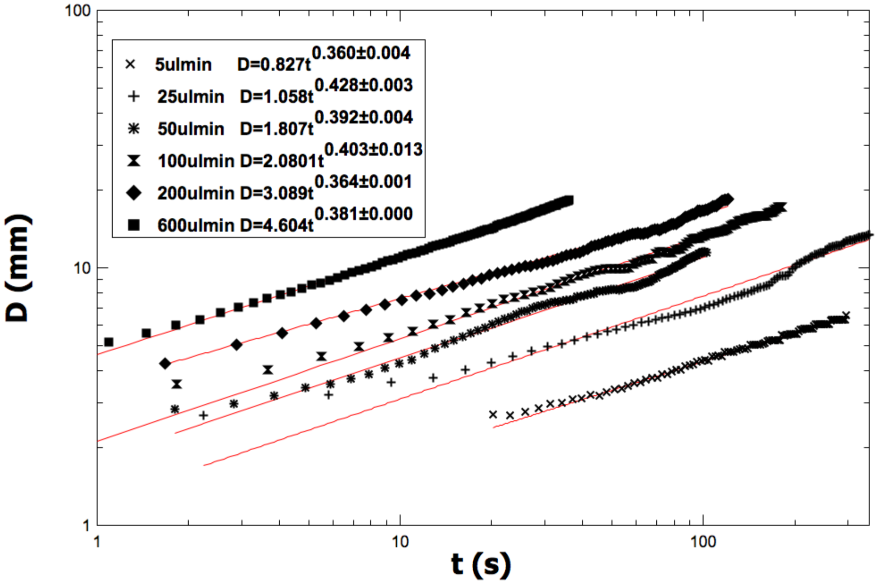

Figure 3.1: Base diameter versus time for isothermal (25 °C) spreading of DI water on a glass substrate. Water flow rates are adjusted to 5 μl/min, 25 μl/min, 50 μl/min, 100 μl/min, 200 μl/min, and 600 μl/min. Markers represent actual data, whereas the solid lines are power functions fitted to the data.

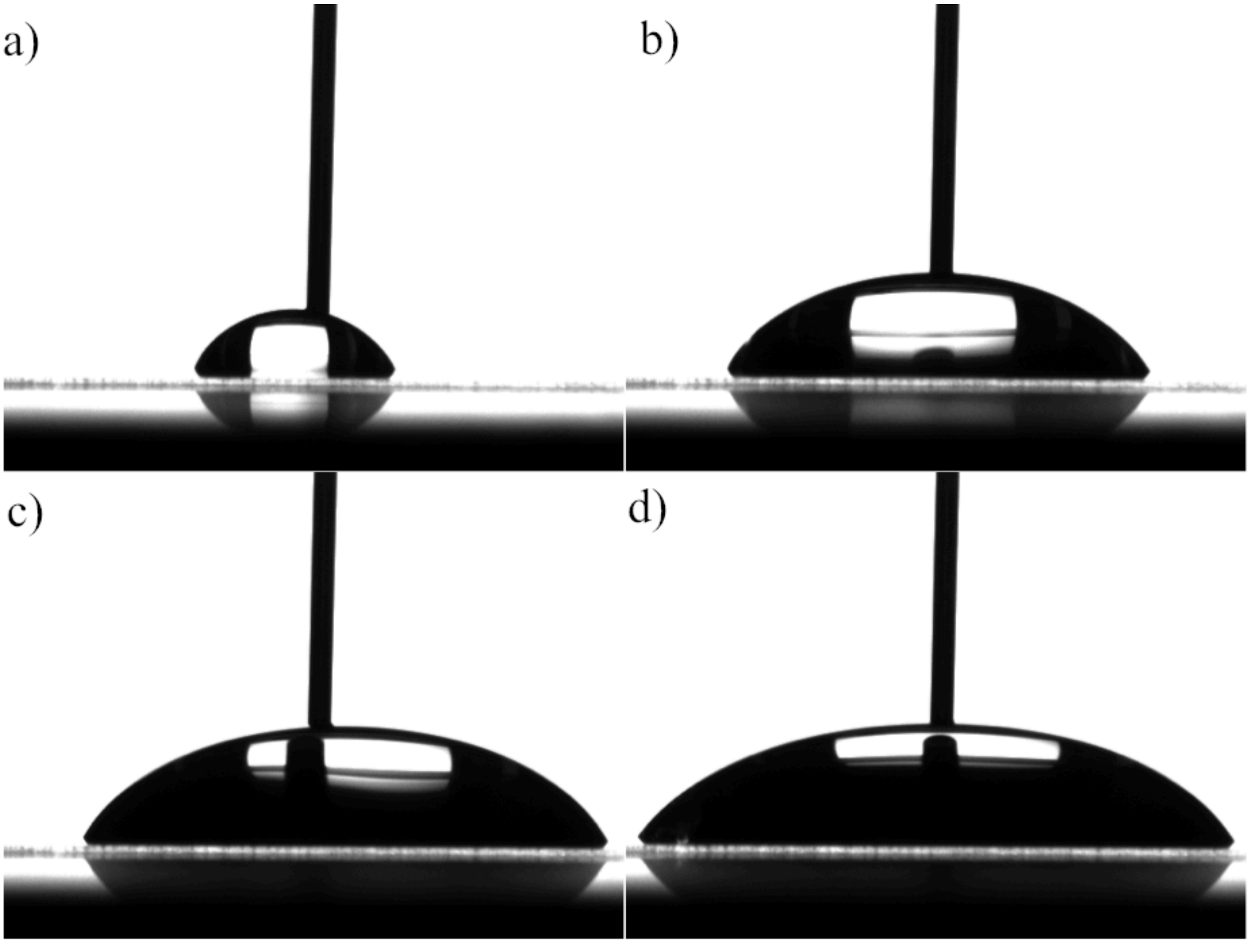

Figure 3.2: Isothermal spreading of water under constant flow rate of 100 μl/min on a glass substrate at a) 5 s, b) 40 s, c) 80 s, and d) 100 s.

3.2 Conclusions

Here, we seek to derive an equation showing the temporal evolution of liquid under both isothermal and forced conditions, which is a prerequisite for understanding the non-isothermal spreading. We assume the Tanner law prevails during the liquid spreading and relate varying volume of the liquid during the spreading to the flow rate of the injection needle. The theoretical correlation derived using scaling analysis confirms the experimental results. This formulation acts as a prerequisite for understanding the non-isothermal spreading and its dynamics. Subsequently, the relationship manifests itself during the upcoming hypothesis development of spreading solidifying drops.

CHAPTER 4

Non-isothermal Spreading and Arrest of Liquids on Cold Substrates

4.1 Introduction

The objective of the upcoming chapter is to provide empirical data to obtain a relationship between post-solidification geometry of the solidifying liquids with affecting physical parameters and to verify the proposed hypothesis, to be discussed later in this dissertation. The equation derived from the hypothesis development is then compared to the obtained data in section 4.2. The proposed hypothesis is thoroughly tested in section 4.3. To this end, mediocre quality of visualization techniques hindered accurate measurements of the drop contact angles. Computational algorithms to outline the liquids geometry have progressed substantially. Moreover, the location of solidification nucleation postulated in the previous related studies is inexact. All of the aforementioned reasons necessitate new sets of experimental data and analysis of spreading liquids on cold solid targets.

4.2 Solidifying spreading liquid on cold substrates

In order to examine the liquid motion and solidification over a variety of dynamic and thermal conditions, we have devised forced spreading experiments using the injection needle. Tests were run at various combinations of the substrate temperature, type of liquid and dispensing flow rate. The non-isothermal spreading in our experiments generally can be subdivided into three regimes. First, there is a regime in which instantaneous solidification occurs at the moment of liquid contact to the impermeable subcooled solid substrate. In this regime, solidification time is larger than the spreading duration. In the second regime, which usually occurs at higher flow rates and smaller *Ste*, substantial spreading of liquid precedes solidification (delayed freezing) (Fig. 4.1. a,b). In Figure 4.1, water spreading and solidification sequence on a cold glass substrate at a) 15s, b) 92s, c) 93s, d) 113s (*Ste* = 0.158) with flow rate of 25 μl/min are depicted. The drop arrest at the contact line due to freezing (Fig 4.1.c) and a thin frozen layer is formed at the base, while the bulk of the drop is still in a liquid state. Liquid continues to accumulate on top of the solidified crust (Fig 4.1.d). Ultimately, if the liquid feeding from the injection needle is stopped, the drop as a whole freezes on a much longer timescale. As liquid solidifies on the cold substrate, two geometrical parameters of the arrested base diameter (D^*) and the arrested contact angle (solidification angle) (θ^*) (Fig 4.1.c) are defined. As capillary and viscous forces are mostly dominant in our experiments, the drop maintains its spherical geometry. We note that, unlike lava and ice-sheets [84], no significant finger or lobe formation was observed during the liquid spreading and arrest. In the last and third regime, dominant at $Q \rightarrow \infty$ or/and $Ste \rightarrow 0$, no solidification transpires during the spreading and the droplet remained liquid during the entire spreading process. When the spreading is conducted for long periods of time or very thin liquid layers with small contact angles, deviation from axisymmetric spreading is observed.

Using DSA100, two main variables of the substrate temperature and the flow rate of liquid can be adjusted accurately. Figure 4.2 shows experiments where water was forced to spread with a flow rate of 50 μl/min on a cold solid glass substrate at five different temperatures of 0° C, -12.5 °C, -15 °C, -17.5 °C and -22.5 °C. At t^*, the time at which the drop is pinned down due to the solidification start, the base diameter becomes time-invariant. When the substrate temperature is close to the freezing point, the molten line advances over the target, and the post-solidification shape is characterized by a large footprint and low profile. In contrast, when the target temperature is significantly below the freezing point, the droplet arrests quickly, and the final post-solidification shape retains a small footprint, with the droplet standing high on the target. Figure 4.3 depicts the base diameter of the water liquids as a function of time at constant substrate temperature with varying flow rates of 2.5 µl/min, 5 µl/min, 6.25 µl/min, 7.5 µl/min, 10 µl/min, 25 µl/min, 32.5 µl/min, and 50 µl/min. The plot suggests that higher flow rates postpone the solidification for water leading to higher values of solidified footprint. Lower flow rates resulted in instantaneous solidification of liquid, whereas at higher flow rates, a transition from the instantaneous to delayed freezing regime transpires. The three regimes of spreading and solidification can be detected visually or from the plots of base diameter as a function of time (Figure 4.2, 4.3). Visual observation acts as a direct indication of the drop solidification start, as the drop gets instantly both immobile and opaque. Horizontal lines in the Figure 4.2 represent the solidification inception of the experiments and the value of *D* after the horizontal lines correspond to D^* (arrested base diameter).

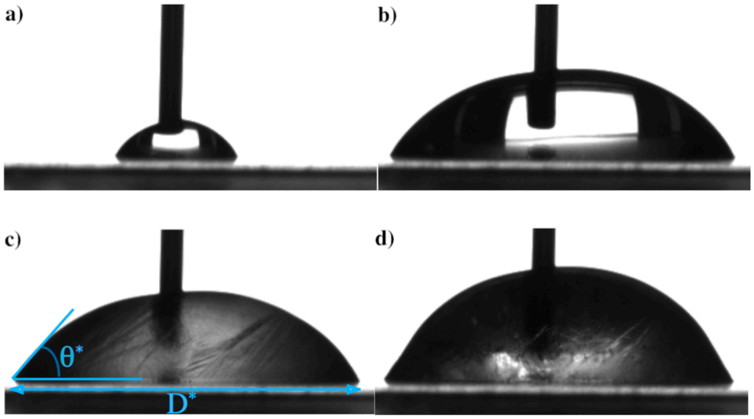

Figure 4.1: Water spreading and solidification sequence on a cold glass substrate at a) 15s, b) 92s, c) 93s, d) 113s (*Ste* = 0.158) with flow rate of 25 µl/min. The water liquid stopped moving when solidification is initiated (c) and upcoming water from the needle started accumulating on the drop (d). The vertical solid line shows the flat-tipped injection needle with an outer diameter of 0.5mm.

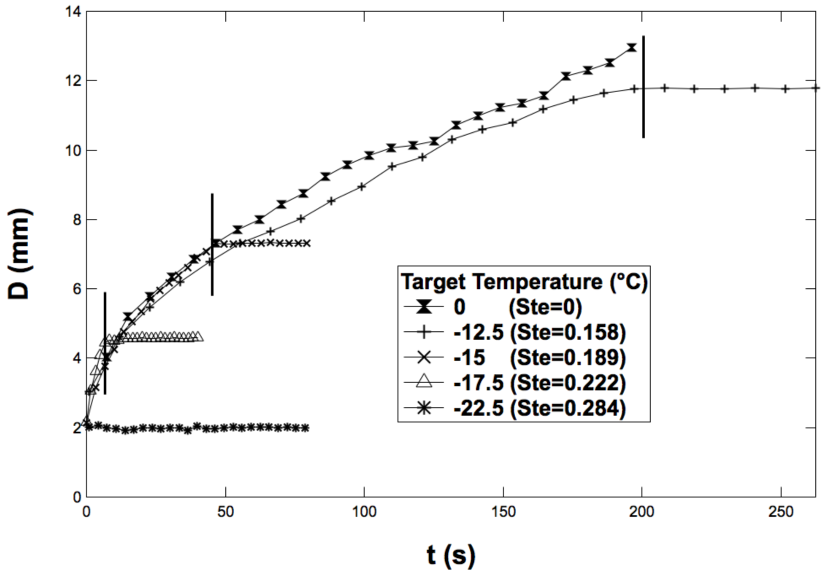

Figure 4.2: Base diameter of water versus time with a flow rate of 50 µl/min on a glass target with temperatures of 0 °C, -12.5 °C, -15 °C, -17.5 °C and -22.5 °C. Horizontal lines represent the solidification inception in the experiments and the value of D after the horizontal line corresponds to D^* (arrested base diameter).

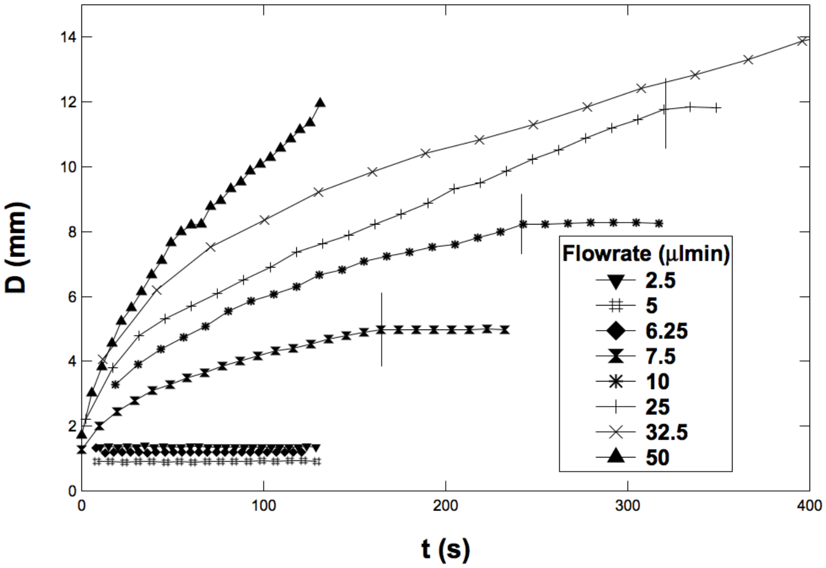

Figure 4.3: Base diameter of water versus time on glass with temperature of -10 °C (*Ste*=0.127) at multiple flow rates. Horizontal lines represent the solidification inception of the experiments and the value of D after the horizontal line corresponds to D^* (arrested base diameter).

Tests of spreading of liquids on cold substrates are run at various combinations of substrate temperatures and dispensing flow rates for different fluids. After some amount of liquid spreading and subsequent solidification, arrested base diameter, D^*, and solidification contact angle, θ^*, are defined at the moment that the drop gets pinned down due to solidification start (Fig. 4.1.c). All values of arrested base diameter and solidification angle of hexadecane, pentadecane and dodecane belong in instantaneous solidification regime. It is worth mentioning that the values of D^* and θ^* do not change in time after solidification inception (Fig. 1.d). The dimensionless final post-solidification shape is characterized by the extent of spreading, denoted by D^*/L_{cap} where the capillary length is $L_{cap} = \sqrt{\sigma/\rho g}$, and *g* is the gravitational acceleration. Figure 4.4 shows the dimensionless diameter of the solidified drops, D^*/L_{cap}, versus dimensionless form of the substrate's temperature for hexadecane, pentadecane, and dodecane. The plot displays more than 275 experiments conducted on the spreading solidifying drops. Duthaler [72] and Schiaffino [25] data are included for comparison and are shown in dashed lines. Increasing *Ste* (colder substrate) causes the drop to solidify with a smaller footprint and higher solidification contact angle. Variations of D^*/L_{cap} get larger at the temperatures close to the melting point of hexadecane and pentadecane, as trivial perturbations of the substrate's temperature substantially affect the outcome. At $Ste.\mathrm{Pr}^{-1/3} = 0.2$, a drastic change in behavior is observed and the values of D^* become more sensitive to *Ste*. At this point, θ^* start to exceed the right angle and even reaches values as high as 120°. *Pr* is the Prandtl number and is shown as $Pr = C_p\mu/k$ where C_p is heat capacity at constant pressure, *k* is thermal conductivity, μ is liquid viscosity. *Pr* is the ratio of viscous diffusion rate to thermal diffusion rate. A power function is fitted to the experimental data, because the drop post-solidification diameter data acts asymptotically with respect to *Ste*. Our power law exponent of -1/3 follows the same power law as that of previous experiments conducted by Sonin's group [25,72], even though their experimental conditions are only remotely analogous to ours. Their solid substrates are of the same materials as the molten liquid, whereas ours use cover glass as a solid target for all our spreading and solidification tests. In addition, their drop delivery frequency was converted in term of fluid flow rate. From our calculation, their flow rate/frequency are six orders of magnitude faster than us.

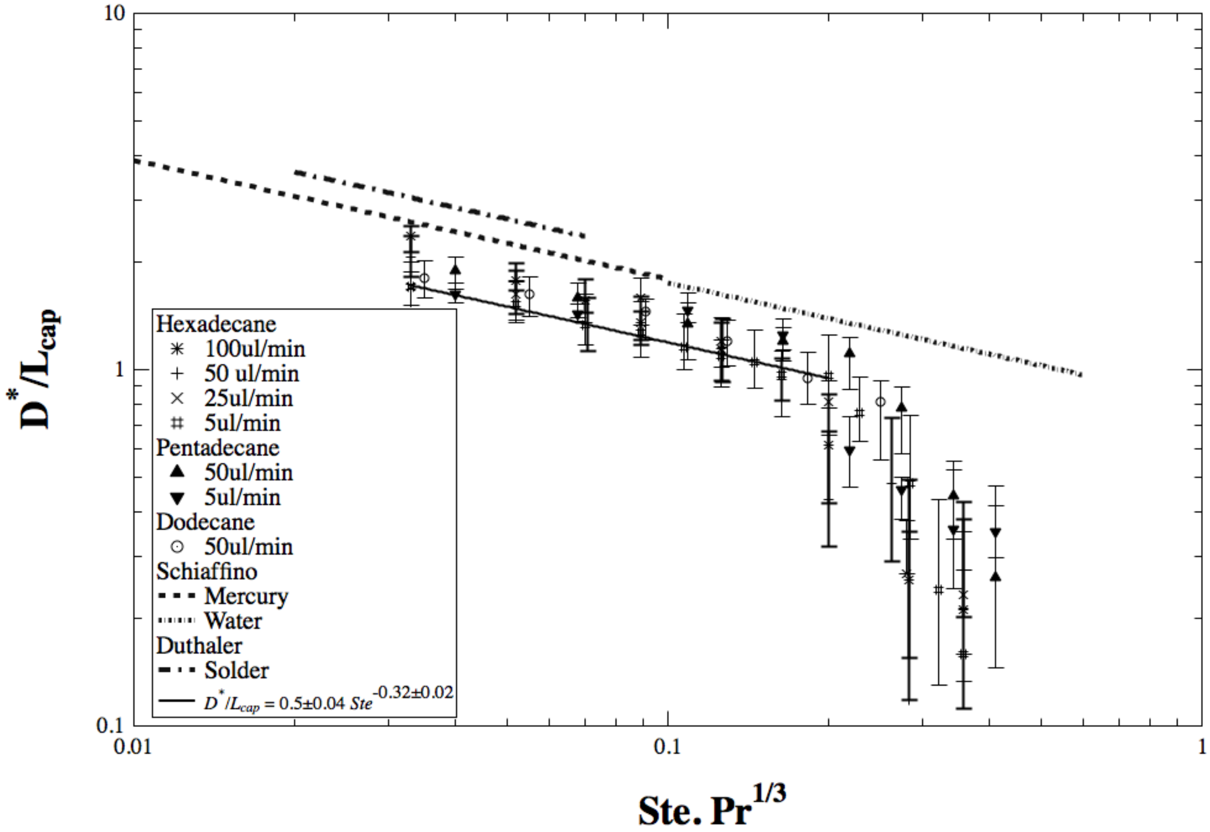

Figure 4.4: Effect of substrate temperature on arrested drop diameter. Duthaler [72] and Schiaffino [25] data are included for comparison and are shown in dashed lines. Solid line represents our fitted equation ($D^*/L_{cap} = 0.5 \pm 0.04 Ste^{-0.32\pm0.02}$) to our experimental data. Each data point is the average of 3 distinct experiments.

4.3 Hypothesis for Critical Solid Volume at the Trijunction

After performing the experiments of solidifying spreading drops, we now present a new hypothesis to describe the spreading solidifying drops and their behavior. Our hypothesis focuses on the near contact line physics at early stages of the drop solidification. In previous studies, location of solidification initiation and dynamic growth front was assumed to originate from the basal plane of the liquid drop covering the trijunction. However, we posit that a drop stops spreading when the volume of solid formed at the trijunction, at which effectively infinite heat flux occurs, reaches a critical value, V_c. The heat flux singularity stems from the discontinuous boundary condition of the heat flux vector at the trijunction [56,85,86]. Also, trijunctions are considered be the locations for the phase change [87] in crystal growth methods such as vertical zone melting and Czochralski process. This critical volume (V_c) emerges beneath an isotherm adjacent to the solid-liquid-gas contact point. Because the air is a poor heat conductor compared to liquid, these isotherms are perpendicular to the free-boundary surface of the liquid [21,58] and extend toward the fluid bulk; however, near the trijunction, isotherms extend thorough the substrate. It is also assumed that the substrate remains at the fixed temperatures during the cooling cycle [21,52]. Radiation and convection with air from the liquid free surface are neglected in our study. This assumption is also confirmed while cooling of 3.2 mm drop, as convection and radiation losses are found to be around 1.7% and 0.8% of initial thermal energy of drop, respectively [88].

Additionally, to support our assumption of solidification initiation from the trijunction, our forced experiments of liquids on cold substrates showed that after solidification start and simultaneous pinning of the liquid drop, the solidified contact angle remained unchanged, although liquid discharge is still continued from the injection needle. One of these experiments is shown in Figure 4.5, in which hexadecane is being forced spread on a glass substrate (*Ste* = 0.03) at flow rate of 200 µl/min. At the solidification start (Figure 4.5.b), The drop gets pinned down with a fixed solidified contact angle and base diameter. After solidification inception, additional liquid feed will be accumulated at the center of the drop with no apparent variation in the drop's solidified contact angle and base diameter (Figure 4.5.c,d).

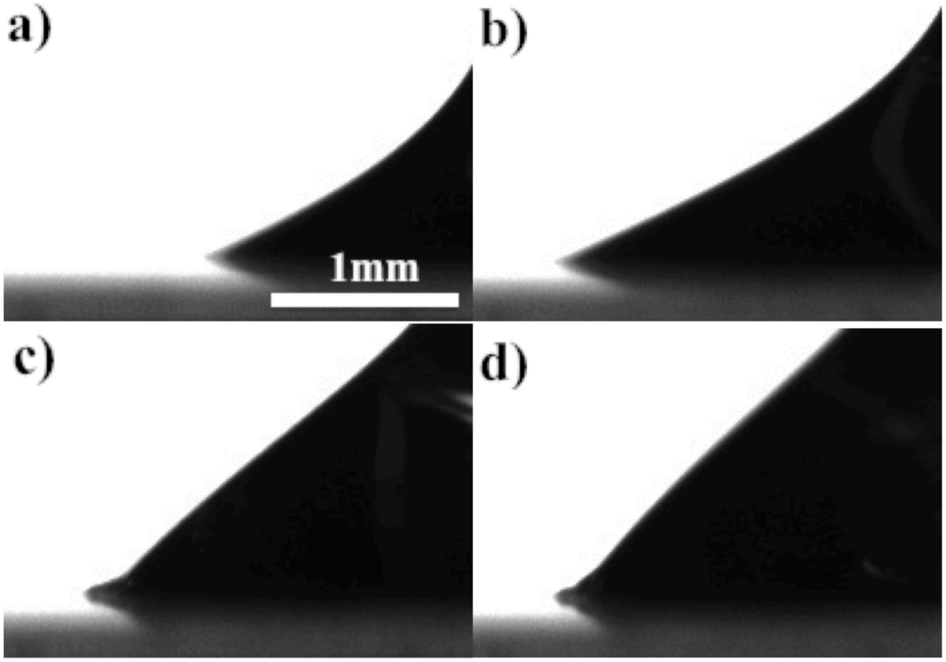

Figure 4.5: Hexadecane spreading and solidification sequence on a cold glass substrate at a) 80 ms, b) 1323 ms, c) 1833 ms, d) 3667 ms after the touchdown (*Ste* = 0.03) with flow rate of 200 µl/min.

The solidified volume of V_c equals the circular sector multiplied by drop's circumference (Figure 4.6):

$$V_c = 2\pi R\left(\frac{\delta^2\theta}{2}\right) \tag{4.1}$$

where V_c is a critical ice volume, R is a radius of a spreading drop, and δ is a radii of a circular sector representing critical ice area under an arbitrary isothermal line. Equation 4.1 displays the volume of critical solidified region, which equals to the multiplication of drop circumference ($2\pi R$) and the solidified circular sector at the trijunction ($\delta\theta^2/2$).

As the length of solidified layer, δ, near trijunction is much smaller than the drop diameter, one-dimensional analysis suffices for addressing this problem. In addition, the classical solidification model [89] was used in literature for the drop solidification problem[60,68,90,91]. We used the same model to find the grown length of the solidified form, $\delta(t)$, starting from the contact line (Figure 4.6),

$$\delta(t) = \sqrt{4\,t\,\alpha\,Ste} \tag{4.2}$$

where t is the time of solidification, and α is thermal diffusivity.

Volume of a spherical cap, taking into account the constant flow rate from the needle can be written as:

$$V(t) = Qt = \pi R^2 h \tag{4.3}$$

where Q is the fluid flow rate from the injection needle. For small contact angles and small drops, h (height of the apex) can be shown as:

$$\tan\frac{\theta}{2} = \frac{h}{R} \tag{4.4}$$

The equation applies on the premise that the drop shape is not large enough to be affected by gravity. Volume of the drop at any time during forced spreading can also be scaled to the area of the drop multiplied by contact angle (θ):

$$V(t) \cong \pi R(t)^3 \theta \tag{4.5}$$

The flow rate of liquid can also be scaled as:

$$Q = \frac{dV}{dt} \cong \frac{d}{dt}\left(\pi R^3 \theta\right) \tag{4.6}$$

Assuming that θ is constant and small as compared to $R,$ equation 4.6 can be written as:

$$Q \cong \frac{\pi R^3 \theta}{t} \tag{4.7}$$

We assume that t in equations 4.2 and 4.6 is measured from the onset of the solidification, so that we can eliminate the time component between these two equations. Then, that gives a relationship between R^* and the physical parameters.

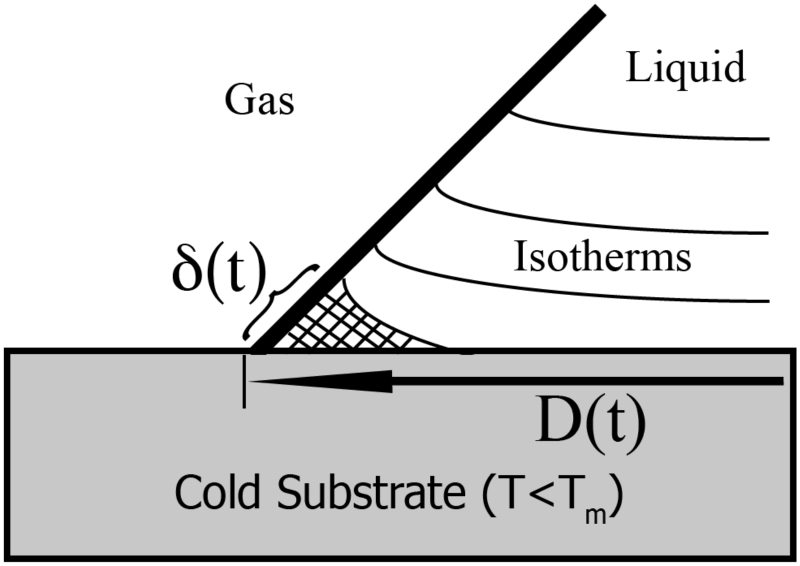

Figure 4.6: Side view schematics of the initial solidified volume of spreading drop on a cold solid substrate. Isotherms are shown as solid lines perpendicular to liquid surface. Hatched region shows an initial solidified region at the trijunction. Drawing not to scale.

Substituting θ in equation 4.7 with the Tanner law $\left(\theta \cong (\mu U/\sigma)^{1/3}\right)$ followed by scaling of the contact line velocity component with the rate of change of the drop radius with respect to spreading time and replacing δ in equation 4.1 with equation 4.2 and combining resultant equations, the time component of both fluid flow and heat transfer is eliminated. Hence, the arrested base diameter will be related to *Ste* as follows:

$$\left(\frac{R^*}{a}\right) = C.Ste^{-1/3} \tag{4.8}$$

$$C = \frac{0.4 V_c^{1/3} Q^{1/6}}{\left(\alpha^2 \mu / \sigma\right)^{1/6}} = \frac{0.4 V_c^{1/3} Q^{1/6}}{\left(\mu^3 / \rho^2 \sigma\right)^{1/6}} \mathrm{Pr}^{1/3} \tag{4.9}$$

where the Prandtl number is $Pr = C_p \mu / k$. We also note that $D^* / L_{cap} = D^* a / a L_{cap}$.

From the test of solidifying spreading drops, solidification contact angles are measured using DSA100 software. Solidification angle versus *Ste* plot is shown in Figure 4.7. The plot shows the values for the case of hexadecane, pentadecane, and dodecane. Solidification contact angles for the liquids investigated ranges from 21° to 157.2°. In all of our data, a certain level of data scatter was always present. This scatter of the data is larger for smaller *Ste*, possibly due to high relative sensitivity of solidification at temperatures close to the melting point. Arrested contact angle is independent from liquid flow rates especially at very high and low Stefan numbers. Our results seem to diverge from Schiaffino's at high Stefan numbers. Their contact angle measurements were less sensitive to substrate temperature. As molten liquid in Schiaffino's experiments is deposited on a solid substrate of a same material, local melting of the substrate at the vicinity of trijunction may have occurred during deposition. This local melting accounts for the undervalued arrested contact angles measurements from the actual arrested contact angle. Variations of θ^* get larger at the temperatures close to the melting point of the liquids, as trivial perturbations of the substrate's temperature substantially affect the outcome. The plot also depicts limiting behavior: for $Ste \rightarrow \infty$ (large substrate supercooling), $\theta^* \rightarrow \pi$ (the drop solidifies without apparent spreading), and for $Ste \rightarrow 0$ (small substrate supercooling), $\theta^* \rightarrow 0$ (the droplet spreads completely over the substrate).

Further, we seek to extend our proposed hypothesis to the contact angle values versus *Ste*. To do so, we assume that the liquid drops take a spherical cap form. For assuming that the liquid drops take a spherical cap shape, Bond number (*Bo*) should be less than unity. The Bond dimensionless number is a measure of the importance of surface tension forces compared to the body forces. The bond number is shown as $Bo = \rho g\left(D^*\right)^2/\sigma$, where ρ is liquid density, D^* is the solidification diameter, σ is surface tension of the liquid, and is the standard acceleration due to gravity. Maximum values of bond number for hexadecane, pentadecane and dodecane are 0.568, 0.754 and 0.652, respectively. This indicates that we can neglect the role of hydrostatic pressure variations in distorting the shape of the drop and the drops assume a spherical cap shape. Therefore, considering that the final solidified shape is spherical cap, mass conservation relates arrested contact angle to the dimensionless arrested base diameter by [25]:

$$\left(\frac{R^*}{a}\right) = \frac{4\sin\theta^*(1+\cos\theta^*)}{(1-\cos\theta^*)(2+\cos\theta^*)} \tag{4.10}$$

Where R^*/a is a non-dimensionalized length, and θ^* is a solidification contact angle of the drops. Substituting equation (4.10) into equation (4.8), yields an equation for solidification contact angle as a function of *Ste* obtained from a second–order expansion of solidification contact angle:

$$\theta^* = \frac{9}{16}\frac{C^3}{Ste}\left(\sqrt{1+19\left(\frac{Ste}{C^3}\right)^2} - 1\right) \tag{4.11}$$

By putting the values of *C* obtained from fitted power law equation (Equation 4.8) to the experimental data points of D^*/a versus Ste, modified function (Equation 4.11) perfectly fits our data starting from 0° and extending to 180°. The modified function is depicted in Figure 4.7 in a black solid curve.

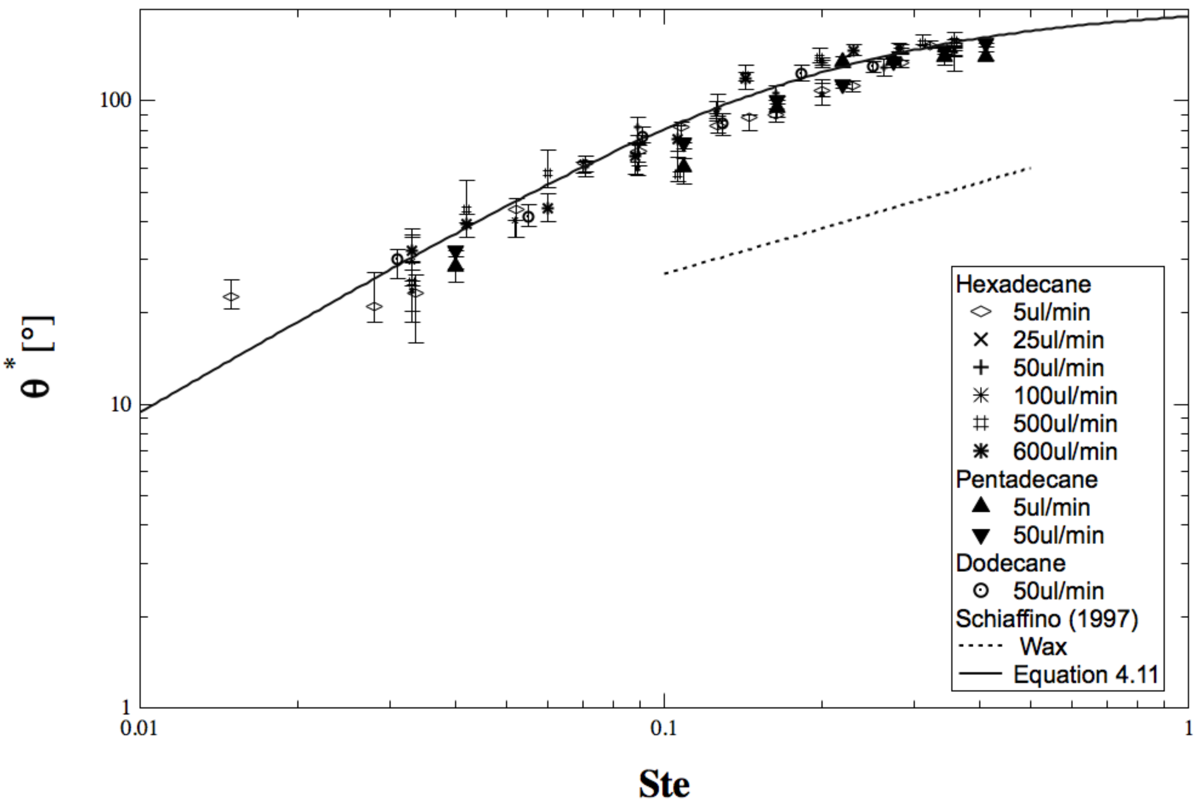

Figure 4.7: Arrested contact angle versus *Ste* for different liquids and flow rates. The black solid line is the equation 4.11 with average value of *C* corresponding to experiments conducted. Dashed line corresponds to the wax experimental data of Schiaffino and Sonin [65].

We now have introduced a working hypothesis to explain the drop evolution and arrest due to solidification on cold solid substrates at low initial velocity of the drop. This novel hypothesis is introduced, as previous proposed fusion interface did not satisfactorily address the observed data of the solidifying spreading drop. The experimental data seem acceptable as an adjunct to theoretical justification stemmed from the suggested hypothesis, however, the hypothesis should be rigorously tested in other systems of spreading followed by solidification. In order to assess the validity of the proposed explanation, two distinct sets of experiment are designed to test the suggested hypothesis:

1-Impact experiments

2- Inclined plane experiments

These designs are potentially capable of either authenticating or fully negate the whole premise of the hypothesis. In short, the premise states that a finite volume of ice forms and grows at the trijunction point under an arbitrary isotherm, which eventually stops the spreading of the drop. Both sets of experiment are governed by distinguishing fluid dynamics, but rather similar heat transfer regimen.

4.3.1 Impact Experiments:

To validate our proposed hypothesis, we planned free fall experiments and compared the results to the derived equations stemming from our working hypothesis. The free fall impact experiments of single hexadecane drops were conducted from Weber numbers of 2.4 to 81.6 on the glass and copper substrates. Different Weber numbers are obtained by tuning the height of the needle from the solid target. Higher elevation of the injection needle corresponds to higher Weber number. During the liquid discharge from the injection needle, the drop becomes larger in size and eventually falls under its own weight (Figure 4.8). The diameter of hexadecane drops, just after the drop detachment, for all of the experiments is given by the DSA100 software and were nearly identical (1.9mm). Moreover, The average of the drop diameters is also measured prior to the detachment following these steps: i) the vertical and horizontal radii ($r_{vertival}$ and $r_{horizontal}$) of the elongated drop is measured just prior to detachment from the injection needle, ii) both radiis are related to the diameter of the spherical drop using [72]:

$$a = \left(r_{vertical} . r_{horizontal} \right)^{1/3} \tag{4.12}$$

where a is the drop radius, $r_{vertical}$ and $r_{horizontal}$ are major and minor axes of the eclipse. Finally, all of the diameter results over the numbers of experiments are averaged. Calculations show that the diameter of the drops calculated from equation 4.12 is approximately the same, less than 5%

margin, as the measurements of the DSA100 software. The error is determined by a one-sample *t*-test.

From experimental data shown in Figure 4.9, at high enough *We*, D^* gets totally independent with *Ste* number manifesting in horizontal lines of D^* versus *Ste* plot. Figure 4.9 shows the dimensionless arrested diameter, D^*/a, versus *Ste* for hexadecane on glass and copper substrate. At lower *Ste* numbers, the drops spread more radially assuming a donut-like form and *We* seem to have little effect on the post-solidification diameter. At constant *Ste*, arrested base diameter of hexadecane is lower on copper substrate, as compared to glass substrate; because thermal diffusivity of the copper plate is four orders of magnitude higher than the glass substrate. Most importantly, the dimensionless arrested diameter becomes independent of *Ste* at high Weber numbers.

Now we will extend our theorization to the impact experiments; the general form of the equation (4.1) still holds and the critical volume scales with equation (4.5). Clearly, volume of the free falling drops is constant and is not a function of time, in contrary with the forced spreading experiments. Moreover, the radius of the drop in impact experiments advances at the rate of [92]:

$$R \propto t^{\frac{1}{2}} \tag{4.13}$$

This relationship is irrespective of the physical properties of the liquid and the surface[92]. Replacing the time component in equation 4.1 with equation 4.13 and volume component with equation 4.5, results in a new formula for the arrested drop radius, which is not a function of *Ste*. This independence of spreading dynamics followed by arrest from *Ste* is in accord with experimental results shown in Figure 4.9. This further authenticates our proposed hypothesis of critical volume of solid formation at the trijunction. In addition, Bhola ad Chandra [66] also showed the similar trend for the impact of wax droplets on cold aluminum plates. In their study, the variations of spread factor, ratio of final diameter to initial drop diameter, between two distinct temperatures become less at higher impact velocity (Figure 4.10).

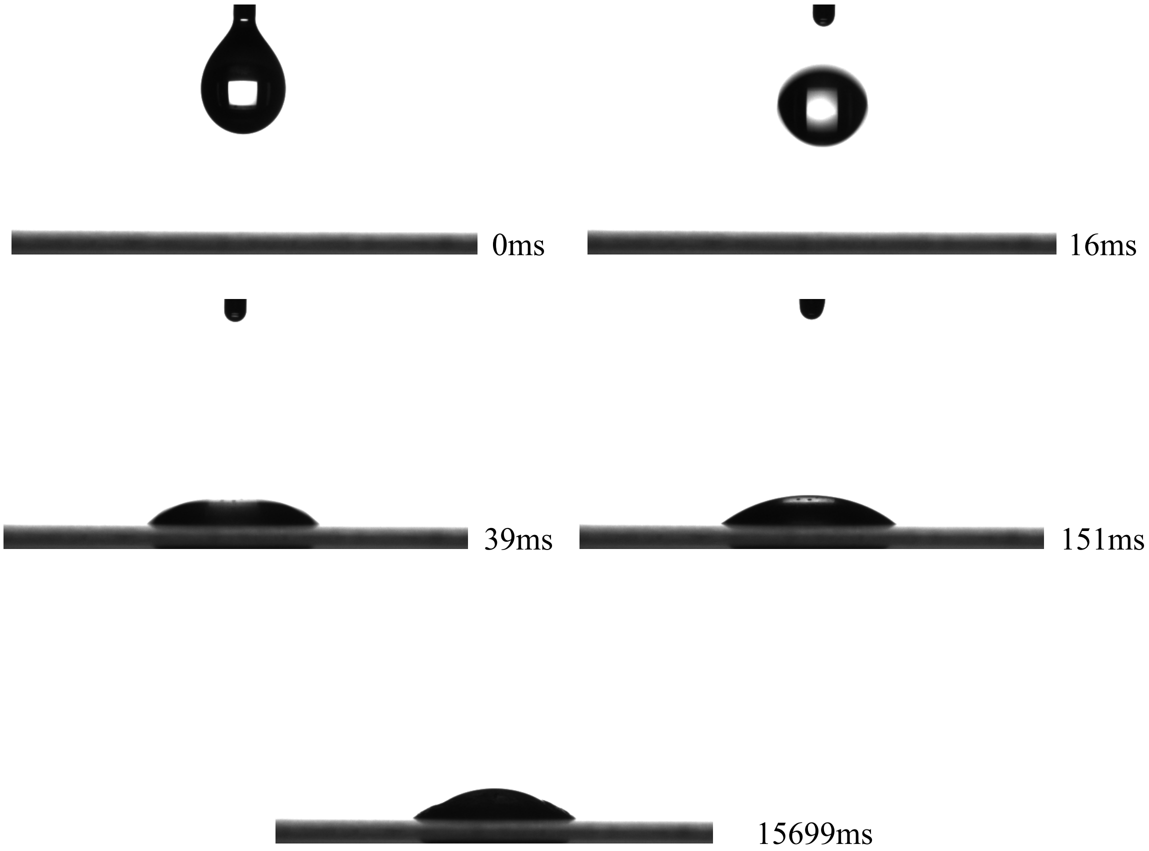

Figure 4.8: Select video frames showing the deposition of a molten hexadecane drop on a glass substrate (*Ste*=0.122). Vertical line is an injection needle with outer diameter of 0.51 mm. Distance of the needle to the solid target is 5mm.

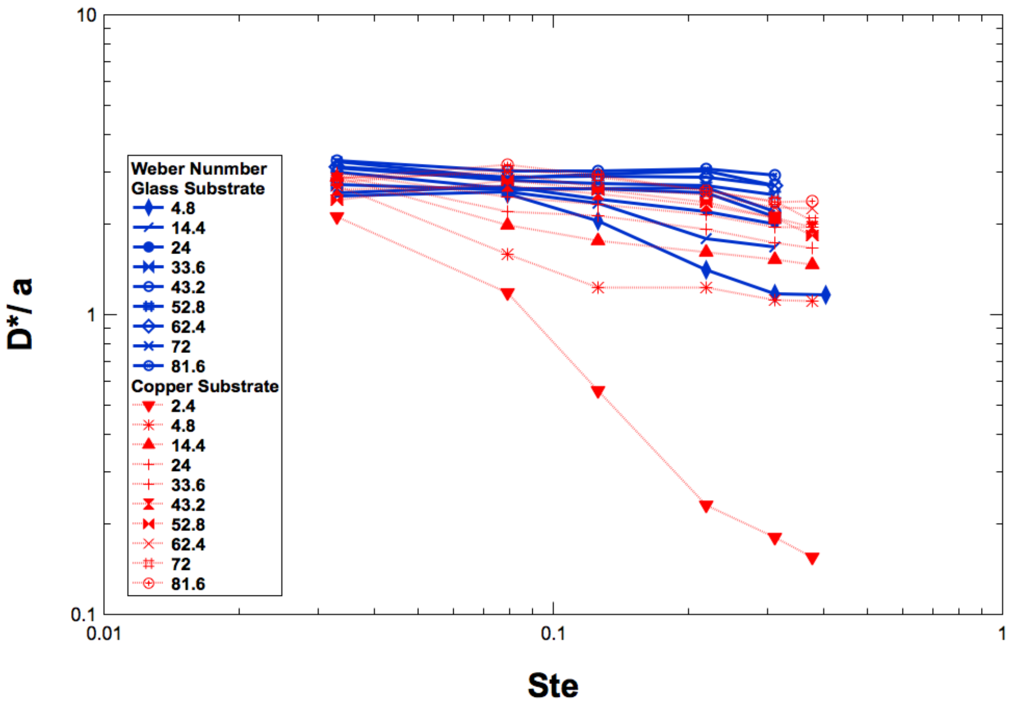

Figure 4.9: Dimensionless arrested base diameter as a function of *Ste* for free fall of hexadecane on copper and glass substrates. Diameter of the drop is denoted by *a*.

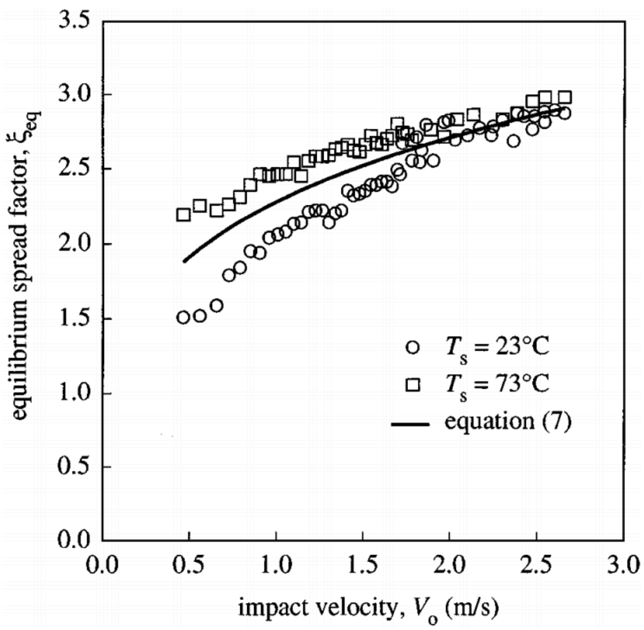

Figure 4.10: Equilibrium spread factor, ratio of final drop diameter to initial drop diameter, versus impact velocity, for impact of wax droplets on an aluminum surface at temperature T_s. Melting point of the wax used is 70 °C [66].

4.3.2 Inclined Plane Experiments:

In these sets of experiment, we fabricated a right-angled triangular prism with predetermined angles of 30 and 60 degrees, and deposited the molten drops on the solid target. A right-angled triangle with thickens of 9 mm is fabricated from aluminum (Figure 4.11). Length of the legs and hypotenuse are 16.2 mm, 22.1 mm and 32.4 mm, respectively. Cover glasses, with properties mentioned in Chapter 2.1, are attached to the specific face of the triangular prism, depending on the inclination angle, using a thermally conductive adhesive. We will impose different temperatures to the substrate and deposit varying drop volumes to obtain multiple values for drop’s post-solidification geometrical data. The downhill contact line is defined as the advancing one, and the uphill contact line as receding one. Through this process, new data will either authenticate or weaken, even invalidate, our model for the spreading solidifying drops.

Figure 4.11: Right-angled triangular prism fabricated from aluminum with smallest angle of 30 degrees. The hypotenuse of this piece is 32.4 mm.

Before performing systematic inclined experiments, it would be constructive to predict the behavior of the molten drops using our proposed hypothesis with combination of the dynamics equation involving the drop’s movement on an inclined surface. In order to extend our hypothesis of the critical volume at the trijunction (refer to Chapter 4.3) to an inclined plate, we assume the drop is spreading down the inclined wedge with the uniform thickness of *S* and length of *L(t)*. The drops stop spreading after the solidification initiation at the advancing trijunction with a solidified contact angle of θ^* and solidified drop length of L^* (Figure 4.12). The critical solidified volume would be the circular sector ($\delta^2\theta^*/2$) multiplied by the thickness of the drop (*S*) on the inclined plate and is written as:

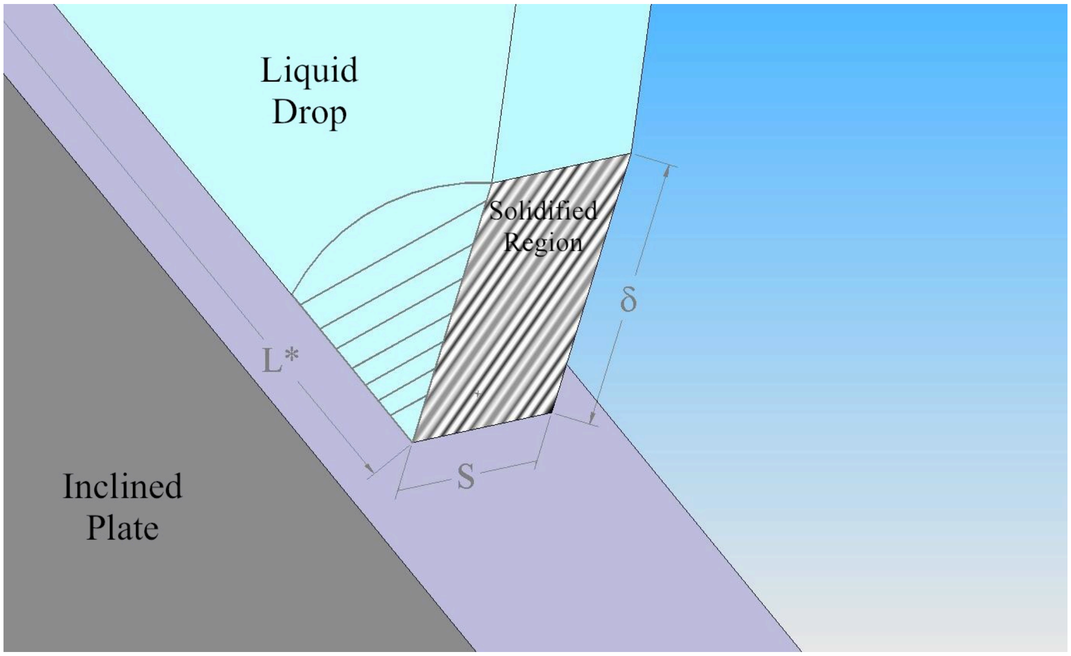

Figure 4.12: Solidified region at the trijunction of the liquid drop flowing down on an inclined plate

$$V_C = S\frac{\delta^2\theta^*}{2} = S(\alpha . t . Ste)\theta^* \tag{4.14}$$

In order to obtain a relationship between *Ste* and L^*, solidified contact angle and time components should be replaced with an appropriate length scale in equation 4.14. To do so, spreading dynamics of liquid on an inclined surface needs to be obtained. Duthaler [72] derived a equation for velocity of two-dimensional fluid sheet (*U*) with cross-sectional area of a^2 flowing down an inclined plane with definitive inclination angle of ϕ:

$$U = \frac{dL}{dt} = \left(\frac{1}{12} \frac{\rho g a^4 \sin\phi}{\mu} \right)^{\frac{1}{3}} t^{-\frac{2}{3}} \tag{4.15}$$

The equation yields a proportionality relationship between *t* and *L*:

$$L \propto t^{\frac{1}{3}} \tag{4.16}$$

Using the Tanner law $\left(\theta \propto (\mu U/\sigma)^{1/3}\right)$ and equation 4.16, liquid contact angle with respect to time can be shown as:

$$\theta \propto L^{-\frac{2}{3}} \tag{4.17}$$

Substituting θ and t with L by using equations 4.16 and 4.17 in equation 4.14 provides a correlation between dimensionless solidified length of the drop and *Ste*:

$$\frac{L^*}{L_{cap}} \propto Ste^{-\frac{3}{7}} \tag{4.18}$$

In our experimental setup, hexadecane drops are released from a definitive distance above the aluminum triangular prism. Figure 4.13 shows two completed experiments of hexadecane drops on the inclined triangular prism. Inset *a* of Figure 4.13 shows a hexadecane drop on an aluminum plate with inclination angle of 60 degrees with the substrate temperature of -20 °C, and inset *b* shows a hexadecane drop on the same plate with inclination angle 30 degrees with the substrate temperature of 12 °C. Increasing inclination angle and lowering *Ste* number result in larger solidified base length.

Figure 4.14 illustrates advancing and receding solidification contact angles of the hexadecane drops versus *Ste* on an aluminum inclined surfaces with inclination angles of 30° and 60°. Two injection needles with diameters of 0.5 mm and 1.8 mm are used to deposit the hexadecane drops. For a constant needle diameter and inclination angle, advancing contact angles are larger than receding contact angles for all of the experiments, except for the injection needle with the diameter of 1.8 mm and inclination angle of 60°. All of the contact angles tend to converge at high Stefan numbers. Variation between advancing and receding solidification angles of hexadecane drops on plates with inclination angle of 60° are larger as compared to inclination angle of 30°.

Figure 4.15 shows the dimensionless length of hexadecane drops versus *Ste* on aluminum inclined planes with angles of 30° and 60° degrees. Two different needle diameters have been used to discharge the hexadecane drop on a cold aluminum tilted plate. For comparison, Duthaler [72] data is also shown in Figure 4.15. The larger needle diameter and inclination angle lead to larger flow of hexadecane drops on the inclined plate. The results are prone to large scatter at higher inclination angle and lower Stefan numbers, as small perturbation significantly affects the post-solidification geometry. At lower Stefan numbers and higher inclination angles, two different stages of flow of the drop are evident: fast flow followed by deceleration and ultimate arrest. No wavy motion or "stick-slip motion" were observed during the experiments. At extremely low *Ste*, the contact angle results are not presentable as receding end of the hexadecane drops takes a shape of a very thin and vanishingly small elongating tail. The black lines in Figure 4.15 correspond to our derived equation of motion and arrest on an inclined plane (equation 4.18). This implies that the experimental data of the cold inclined plates are in accord with theoretical equation stemmed from out proposed hypothesis.

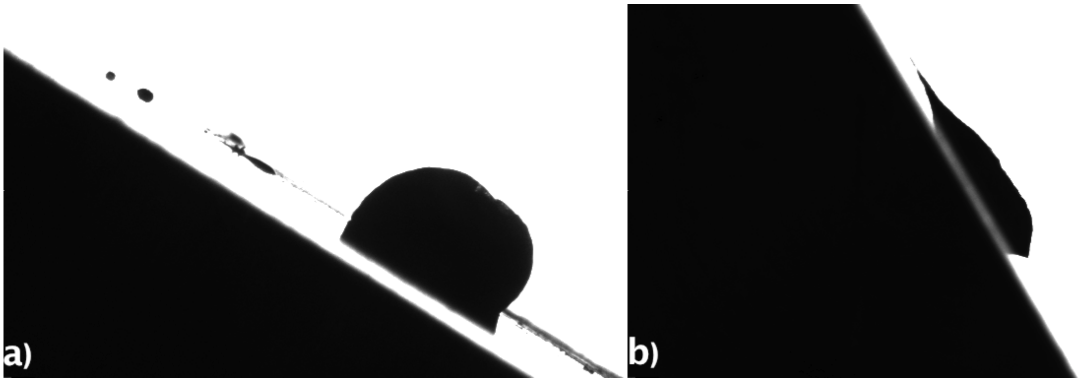

Figure 4.13: Solidified hexadecane drops on inclined planes with substrate temperature of, a) -20 °C with inclination angle 30°, b) 12 °C with inclination of 60°.

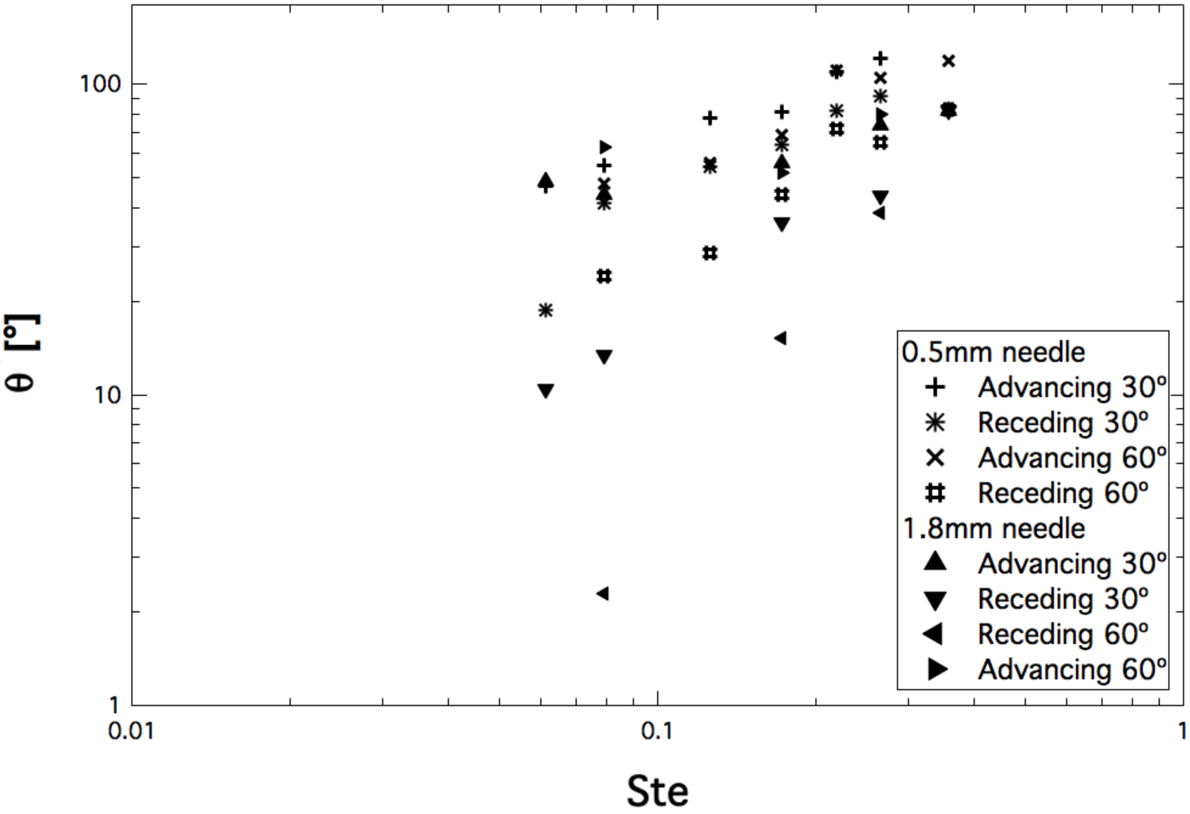

Figure 4.14: Advancing and receding solidification contact angles of hexadecane drops versus *Ste* on an aluminum inclined plane with angles of 30° and 60°.

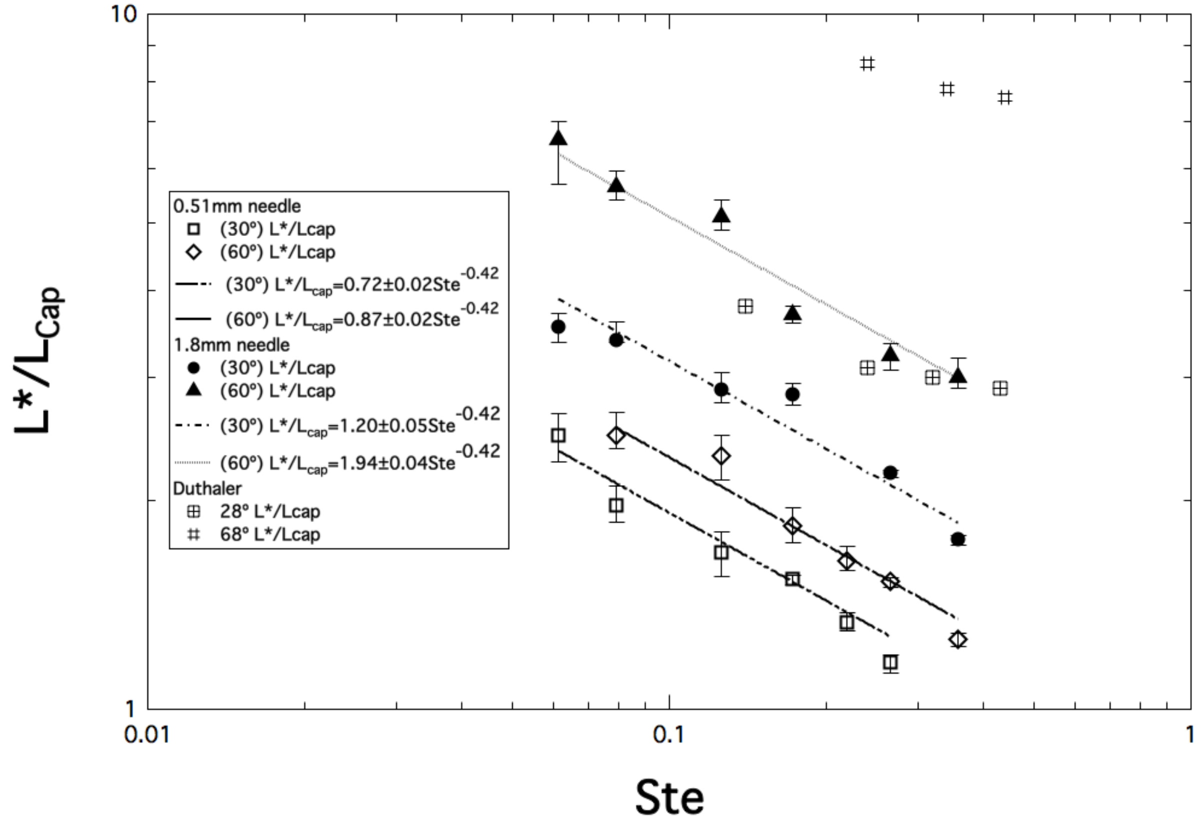

Figure 4.15: Dimensionless arrested base diameter of hexadecane drops versus *Ste* on a aluminum triangular prism with angles of 30° and 60° degrees. Duthaler [72] data also presented in the plot for inclined angles of 30° and 60° degrees for comparison. Solid and dashed lines correspond to equation 4.17, which relates length of solidified drop to *Ste*.

4.4 Special Case of Supercooled Water

When a drop of liquid is placed on a substrate which temperature is below the melting point of the liquid, one would expect the drop to solidify instantaneously. However, some liquids, such as water, must be cooled to solidify below its melting temperature (supercooling) due to homogeneous nucleation's high activation energy. For our case, Water is easily supercooled when it is cooled without any vibration, contamination or a foreign surface. Even supercooling of -47 °C has been reported for submicroscopic droplets by evaporative cooling [93]. In addition, when water is cooled from room temperature, water becomes increasingly dense, as with other liquids. At approximately 4 °C, pure water reaches its maximum density. As it is cooled further, unlike most liquids, it expands to become less dense. These unique properties do impart distinction to the underlying mechanism of water spreading followed by freezing and drastically alter the physics of motion and subsequent arrest.

4.4.1 Supercooled Water Results:

As same with the case of hexadecane, pentadecane and dodecane, two values to define a solidification drop shape are evaluated for water drops: Arrested footprint and solidification contact angle. The dimensionless length can be characterized by D^*/L_{cap}, the ratio between the arrested base diameter over capillary length. The plot of arrested drop diameter with respect to *Ste* is shown in Figure 4.16. Intuitively, the water drops solidify sooner at lower substrate temperature, leading to smaller values of drop base diameter. Given the stochastic nature of supercooled water drops, variance in the arrested base diameter results is expected and no common trend is followed. In order for the results to be statistically significant, 6 data points at each flow rate and *Ste* are included in the plot. Variations in D^*/L_{cap} get larger at lower *Ste* due to the effect of the flow rate before the transition temperature, a temperature at which two regimes of instantaneous solidification and delayed solidification meet. The delayed solidification range for water is wider as compared to hexadecane and pentadecane. The main justification can be that water, unlike most liquids, undergoes supercooling leading to higher rates of spreading at lower Stefan numbers. In a region of delayed solidification, D^*/L_{cap} increased with higher flow rates; however, D^*/L_{cap} seem to be independent from *Ste* in the instantaneous solidification region.

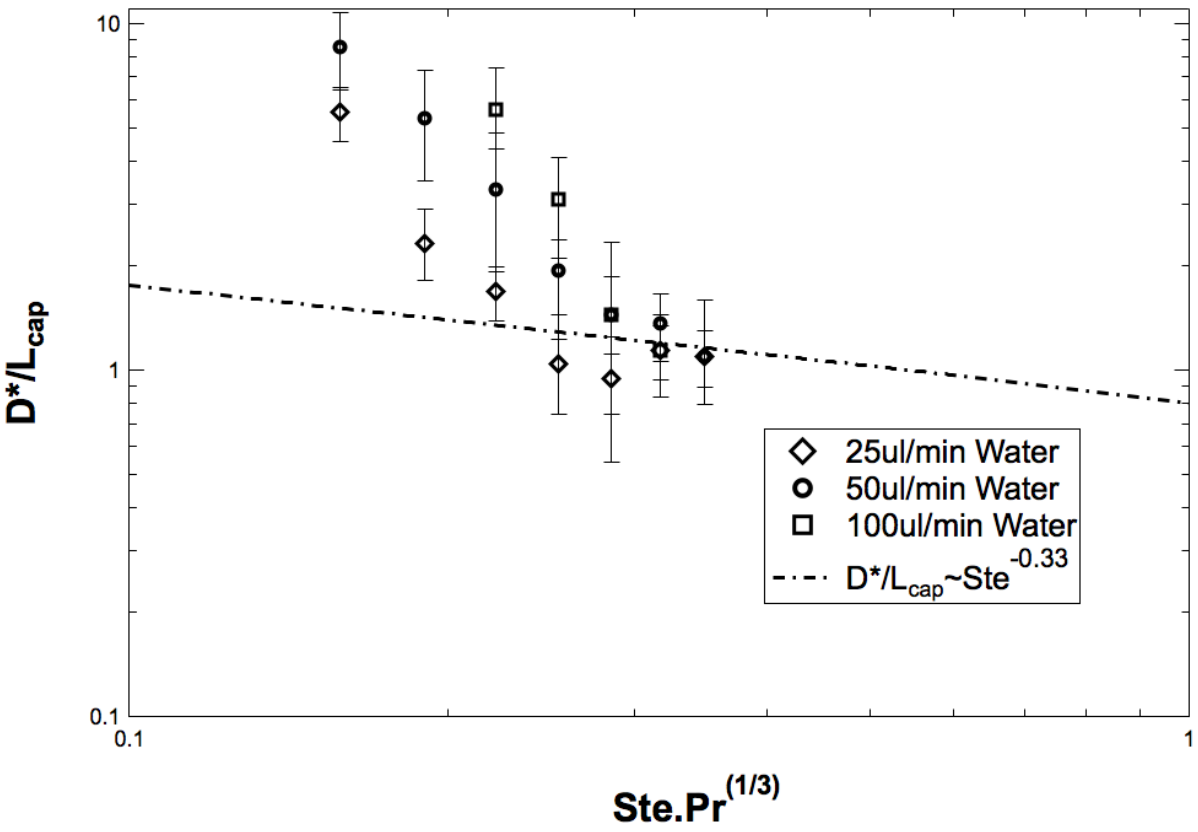

Figure 4.16: Arrested base diameter versus *Ste* for water drops.

4.5 Conclusions

We performed an experimental and theoretical study on the dynamics of molten drops on cold solid substrates, on which the drop spreads and comes to rest when it solidifies. Two sets of post-arrest geometrical parameters i) the arrested footprint (D^*) and ii) the solidification contact angle (θ^*) are experimentally obtained. These two values are measured using a high-speed camera mounted in a drop-shape analyzer (DSA 100) machine. The results show a power-law relationship between the D^* and *Ste* for small arrested contact angles (<65°). Motivated by these experiments, a novel hypothesis is presented aiming to clarify the observed relationships for spreading dynamics followed by solidification. This hypothesis is based on the initiation of the solidified layer from the contact line below an isotherm and ascending through the liquid bulk, which is in contrary to the previous assumption of basal plane formation of a solidified layer. For the first time, for solidifying spreading drops, a theoretical scaling analysis agrees with experimental results, for the liquids that do not supercool and *Ste* is less than 0.2.

To further test our working hypothesis, we designed two sets of experiment, which would either strengthen or negate our presumed hypothesis. First, we performed impact experiments of hexadecane with low to medium Weber numbers on different substrates. In our impact experiments, the dimensionless diameter of the drops becomes independent from *Ste* at high Weber numbers. In the second set of the experiments, we deposited liquid drops on inclined aluminum targets and explored effects of the substrate temperature and inclination angle. By extending our hypothesis to both types of experiments, formulations from our hypothesis and scaling analysis confirm the experimental results signifying that our hypothesis is still valid. It is worth emphasizing that our novel hypothesis, that lead to the theoretical formulation, which relate empirical data of solidifying spreading drop on cold solid substrates to theory using scaling and dimensional analysis, focuses on the early stages of drop solidification from the trijunction, as contrary to previous assumption of basal plane solidification.

Experiments performed on water under forced conditions, deviated significantly from our derived equation, as they undergo notable undercooling during cooling stage. The nucleation and heterogeneous freezing of undercooled liquid, especially water, is considered to be stochastic discerned from large scatter in the arrested base diameter versus *Ste* number, nonetheless the data points converge at higher *Ste* numbers with less scatter. Also, at delayed solidification regime, higher flow rates lead to larger arrested base diameter of water drops.

CHAPTER 5

Solidification Delay on Hydrophobic Surfaces

5.1 Introduction

Ice formation and adhesion can have tragic consequences on human activity in air and on the ground. Any effort to alleviate ice stickiness or/and postpone the freezing inception can lead to improved operation safety and enhanced energy efficiency. Ice accumulation on aerodynamics wing structures can significantly increase drag and weight leading to degradability of airplane control [94]. Wind turbines may stop rotating due to heavy vibrations under uneven ice accumulation. In addition, excessive ice accumulation increases static load on the wind turbine rotor [95]. Prevention methods are categorized into either active or passive operations. Active anti–icing/de–icing system (ADIS) are often based on melting or stripping off of already formed ice structures; however, these techniques can compromise the functionality of the associated materials[96]. Passive methods such as black paint and hydrophobic coatings have been suggested in literature [95,97,98], but their performance has been often unsatisfactory [99].

There is been a huge debate in the last two decades on whether hydrophobic surfaces induces a significant delay on solidification or adhesion [100-106]. If so, the underlying mechanism is still a mystery, however, many factors such as insulating properties of these surfaces [101], less probability of heterogeneous nucleation and reduction of water-solid interfacial [107,108] area have been attributed to these unique features. At relatively higher Weber numbers, hydrophobic surfaces can eliminate frost formation by pushing back impinging droplets [109]. Tourkine et al. [101] claimed that for a given volume, freezing time of static water drops on hydrophobic surfaces is always delayed by a factor of between 3 and 5. They attributed this delay to the presence of a thin film of air that acts as a barrier to thermal transfer. In second series of their experiments, where both volume and surface area were kept constant, still freezing was delayed approximately by a factor of 2. A predictive model that integrates submodels describing droplet impact dynamics, heat transfer, and heterogeneous ice nucleation also confirms the experimental results [110] and demonstrate that superhydrophobic surfaces can fully prevent the freezing of impacting water droplets down to surface temperatures of even -25 °C. In practice, the efficiency of the hydrophobic surfaces under conditions of extreme humidity, airflow [104], icing/deicing cycles [111], and frost formation [105] is critically questioned. Yet despite of these research studies, solidification delay caused from hydrophobicity have remained elusive; partly because icing of water on the hydrophobic surfaces is a complex phenomenon in which it can be affected by temperature, humidity, surface chemistry, surface roughness, contact area, and etc [112].

Despite the discrepancies and uncertainties, classical nucleation theory has been utilized to predict nucleation kinetics. Classical nucleation theory provides a quantitative description of nucleation for supercooled water. In this theory, formation of the stable (critical) nucleus initiates the solidification and is followed by the growth phase. This nucleation is formed either homogenously or heterogeneously. Homogenous nucleation is associated with a solidification of the bulk fluid with no presence of external crystallization center, whereas heterogeneous nucleation involves some kind of external interface, in our case the hydrophobic surface, which reduces the nucleation barrier. In general, energy barrier of heterogeneous nucleation can be related to homogenous one with a geometrical relationship of [113]:

$$W_{het} = W_{\hom}\omega(\theta) \tag{5.1}$$

where W_{het} and $W_{\hom}$ are is the work required to form nucleus in heterogeneous and homogenous nucleation, respectively. $\omega(\theta)$ is the coefficient that is dependent on the contact angle of the liquid and ranges from zero to one. The equation was further extended by Tochev and Gutzow

[114] to derive time lags between homogenous and heterogeneous nucleation. The equation showed that at angles more than 90, nucleation rate in the initial stages of heterogeneous nucleation rate is lower than homogenous. To the best of our knowledge, verification of time lags between these two modes of nucleation using Tochev model [114] has not been substantiated in literature.

In addition to uncertainty related to freezing delay property of hydrophobic surfaces on static drops, forced spreading of liquid water on subcooled hydrophobic surfaces and their freezing timescale study have not been conducted in literature. Here, we explore the claimed freezing delay during the forced spreading of water liquid on subzero hydrophobic surfaces.

5.2 Materials and Procedure

Here we set up experiments to illuminate recent doubtfulness associated with these surfaces efficacy on postponing solidification. In our experiments, water is being spread by an injection needle on cold hydrophobic surfaces. Three different kinds of hydrophobic surfaces were used. Theses surfaces are WX2100^{TM}, Fluorothane^{TM}, and silicon pillars. The full description of the hydrophobic surfaces is tabulated in table 6. ϕ_s is the area fraction of the solid surface in contact with water and can be calculated as the ratio of the total pillar-top surface area to the total projected surface area. Both WX2100^{TM} (aerosol coating) and Fluorothane^{TM} (solution coating) are applied to the surface of cover glasses. It is worth mentioning that the thickness of the hydrophobic films on the cover glasses for both cases of WX2100 ^{TM} and Fluorothane^{TM} has no significant effect on wettability. The hydrophobic materials are chosen as they represent different wettability and structural morphology. These hydrophobic targets then were cooled to subzero temperatures (-10 °C and -20 °C) using a Peltier element. Peltier element is a thermoelectric device, which transfers heat from one of its sides to the other when electricity is applied. Increasing the voltage across the thermo-electric heaters can increase the temperature of the Peltier. The cold side is then brought in contact with the substrate and cools it to a chosen temperature before the water liquid is fed on top of it. Temporal evolution of the drops was recorded using DSA 100 and both contact angle and base diameter are measured by the DSA software.

Table 6: Specifics of the hydrophobic surfaces used in Chapter 5. ϕ_s is the area fraction of the solid surface in contact with water.

Hydrophobic Surfaces	Specifics and Application Method	Equilibrium Contact Angle (°)
WX2100^{TM}	Spray on cover glass	144±1.8
Fluorothane^{TM}	Dip coating of cover glass	142±1.5
Silicon Pillars	$\phi_s = 0.26$	149±1.3

5.3 Experimental Data:

Forced experiments are assigned to be performed on hydrophobic substrates with two different temperatures of -10 °C and -20 °C. Spreading experiments on cold hydrophobic (WX2100, Fluorothane and silicon pillars) and hydrophilic substrates (cover glass) with temperature of -10 °C are performed at flow rates of 5 μl/min, 50 μl/min and 100 μl/min. Figure 5.1 shows the video sequence of water feeding at the rate of 100 μl/min on -10 °C WX2100 coated cover glass. Dynamic contact angles on the hydrophobic surfaces approximately equal the equilibrium contact angles. Elapsed times for insets a-d are 0.448 s, 10.088 s, 40.129 s, and 100.233 s, respectively. Figure 5.2 shows the dynamic drop diameter versus time for the aforementioned parameters. Open markers represent the data for the silicon pillars, whereas filled markers show the data for WX2100 spray. Clearly, as contact angle of water on hydrophobic surfaces is substantially higher than on hydrophilic surfaces, the spreading rate is significantly lower. Movement of water on these hydrophobic substrates is not smooth resembling stick/slip motion. This jerky movement is also discernible from noisy base diameter and contact angle data versus time. The data for these hydrophobic surfaces were smoothed in associated plots for better distinction of the data sets. At 5 µl/min, water instantly freezes at the moment it touches the cover glass, whereas water continues to spread without any sign of retardation and phase change on a cover glass coated with WX2100 hydrophobic spray. At higher flow rates with the same target temperature, freezing does not occur on neither hydrophobic nor hydrophilic surfaces.

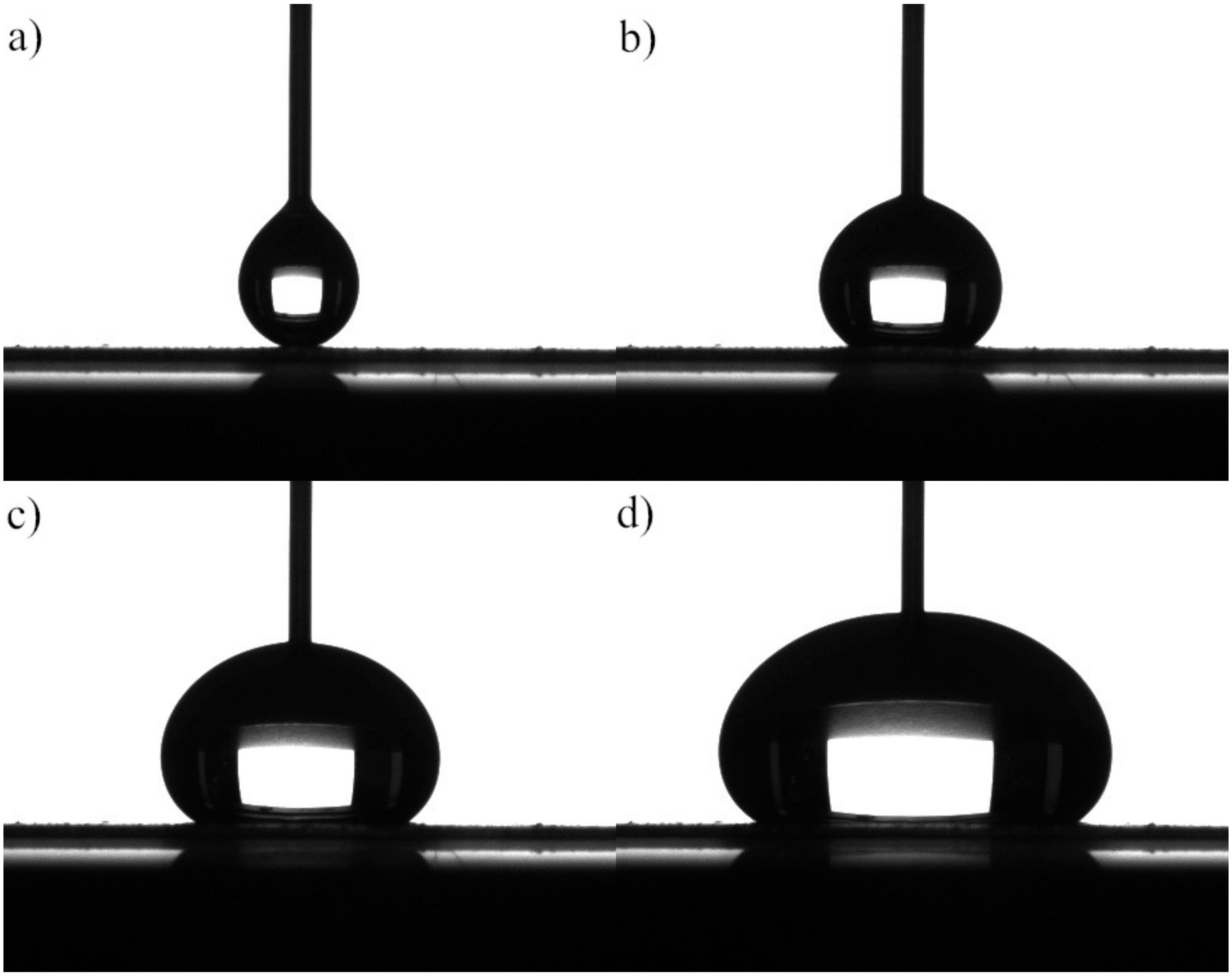

Figure 5.1: Video sequence of water feeding at the rate of 100 μL/min on -10°C WX2100 coated cover glass. Elapsed times for insets a-d are 0.448 s, 10.088 s, 40.129 s, and 100.233 s, respectively.

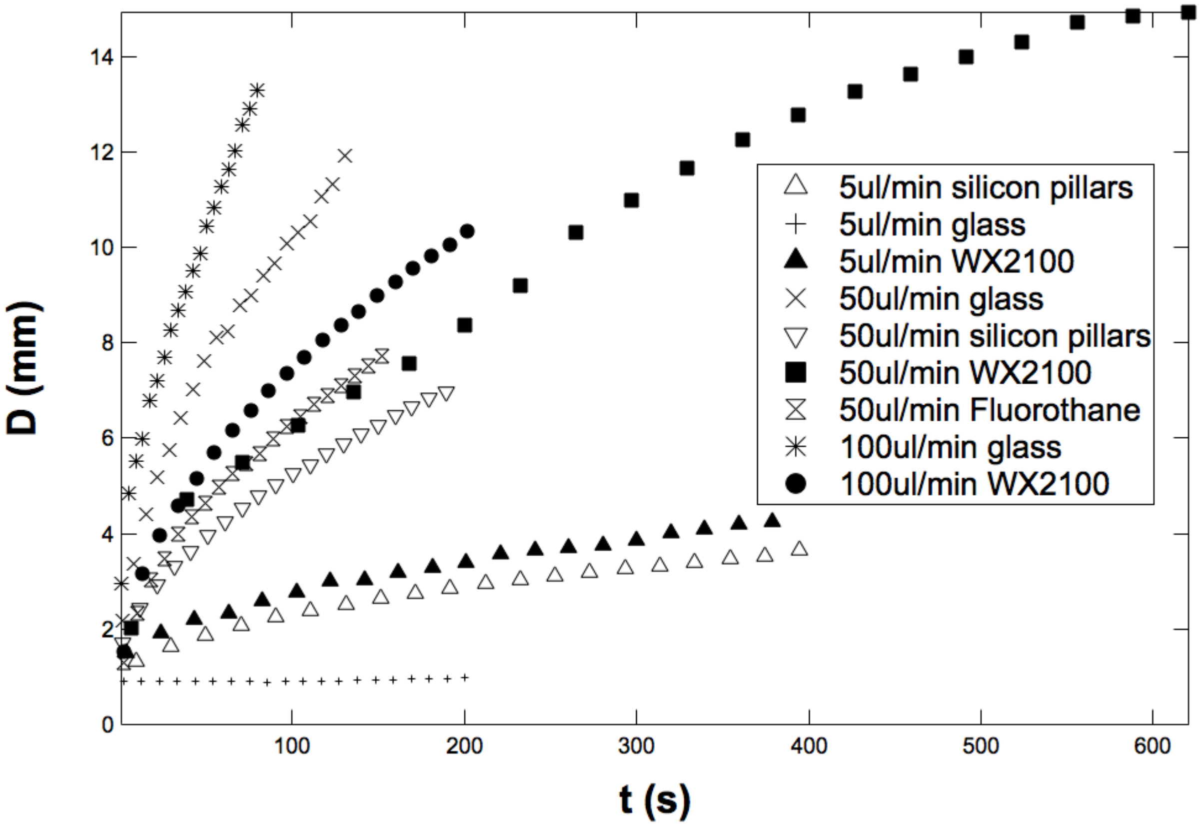

Figure 5.2: Water drop diameter versus spreading time with substrate temperature of -10 °C (Ste = 0.127). Spreading was conducted at flow rates of 5 µl/min, 50 µl/min and 100 µL/min. Three different hydrophobic surfaces (silicon pillars, WX2100 coated surface, and Fluorothane solution) have been used as solid targets.

We now set the temperature of the hydrophobic substrates to -20°C and conducted the same sequence of experiments. Figure 5.2 shows the drop diameter versus time on the hydrophobic surfaces at flow rates of 5 µl/min, 50 µl/min and 100 µl/min. Freezing is discerned to be initiated at the point that the drop footprint versus time plot reaches a plateau. The solidification retardation is more evident at this temperature (*Ste* = 0.254) of the substrate as compared to -10°C. At high enough flow rates, freezing is delayed leading to higher values of arrested base diameter (D^*) and elapsed time to freezing initiation (t^*); however, at 5 µl/min, at which instantaneous solidification ensues, hydrophobic D^* is smaller than hydrophilic D^* because at the moment of touchdown, drop on the hydrophobic surface obtains higher values of contact angles and subsequently lower values of base diameter. Ratio of the arrested base diameter for the hydrophobic surface (WX2100) to the hydrophilic ones for flow rates of 5 μl/min, 50 μl/min and 100 μl/min are 0.75, 2.67, and 1.69, respectively. This implies that at lower flow rates and higher *Ste*, D^* is controlled by wetting characteristics of the hydrophobic surface rather than its solidification delay impact.

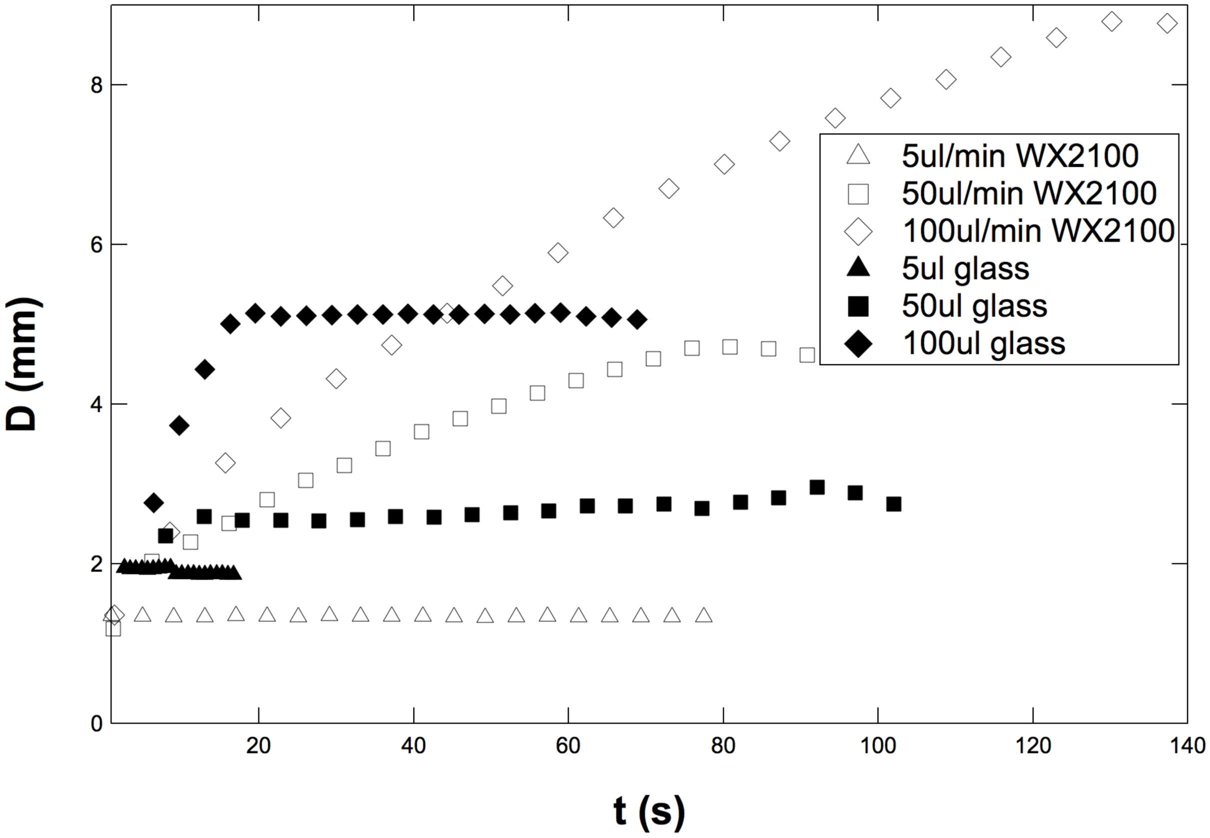

Figure 5.3: Water drop diameter versus spreading time with substrate temperature of -20 °C (Ste=0.254) at flow rates of 5 μl/min, 50 μl/min and 100 μl/min.

5.4 Modeling Data

A numerical heat transfer model using finite element analysis is being used to simulate the effect of contact angle on isotherm progression through the static drop, taking into account the influences of the drop base diameter and thermal diffusivity of liquid. This simulation is implemented by the COMSOL software package. We assume that the solidification of the drop is dominated by local equilibrium and the fusion interface has the melting point of water. Figure 5.4 illustrates the geometry of one the problems analyzed at its initial configuration: a water drop with 0.5 mm base diameter with equilibrium contact angle of 45° situated on a glass substrate. The solid domain is sketched as 2×2mm square object. The solid can be assumed as a semi-infinite body due to a larger size compared with the drop. For simplicity, the drop liquid-gas interface is assumed to be a straight wedge, as the liquid near the contact line becomes very narrow. Height of the drop is fixed to 0.5mm for all of the simulations. For reasons of symmetry, half of the droplet is modeled and the heat flow is modeled using 2D axis–symmetric model. The left vertical dashed line represents the axis of symmetry.

It is also important to verify that the implementation of different mesh generator does not perturb the resulted solutions. To ensure adequate grid resolution, solution-based grid adaption is pursued and the grid independence is inspected in terms of solutions of solidified layer progression (δ). Initially, triangular boundary mesh is generated at the boundaries and the main domains. Subsequently, meshing of the domains was refined until the results variations are intangible. In the liquid domain with area of 0125mm^2, for instance, number of triangular elements used is 19392. Figure 5.5 depicts the qualitative node density in the liquid domain and solid-liquid interface in one of studies. The axes of the figures 5.4 and 5.5 correspond to length scales in millimeters.

The solid domain (r1) and the liquid domain (b1) are set to -20 °C and 25 °C, respectively. The interface between the solid domain and the liquid domain is assumed to be an internal boundary. The bottom boundary of the solid domain is appointed to -20 °C. Thermal insulation is set to all of the remaining boundaries such as air-liquid interface; that is, gas-liquid boundary is adiabatic. Physical properties such as density, thermal conductivity and heat capacity at constant pressure are manually entered in the properties section of the software. The properties entered correspond to water and the cover glass for the liquid and solid, respectively. The values of thermal conductivity, heat capacity at constant pressure, and density for cover glass, from the VWR international, are assigned to 0.2 *W/m.K*, 840 *J/Kg.K*, and 1.8 *gr/cm*, respectively. All of the thermophysical parameters, by definition, are temperature dependent; however, our solidified layer progression results based on the temperature-independent values assigned to the properties are approximately the same (less than 1.5%) as temperature-dependent ones, as temperature range of our study is small. For all of the simulations, the transient studies are conducted and time step of 1ms is used at early stages to pinpoint even minute behavior changes, nonetheless, time step is increased to 10ms at later stages in order to satisfy computer memory constraints.

Figure 5.6 shows the progression of the isothermal line (T=273K) along the liquid-gas interface (δ) versus time for contact angles ranging form 35° to 145° and base diameters of 0.5mm, 1mm and 3mm. The results clearly show that the higher contact angles postpone the isotherm growth. The change of base diameter seemed to be insignificant in altering the results of the progression length, however, some divergence is evident at later stages with respect to the base diameter. To directly illustrate the effect of contact angle, specific times of Figure 5.6 at early stages are chosen and illustrated in Figure 5.7. The progression of the isothermal line (T=273K) with respect to different contact angles at progression times of 0.02 s, 0.03 s, 0.04 s, 0.05 s, 0.06 s, 0.07 s, 0.08 s, and 0.09 s is shown in Figure 5.7. The Figure is shown in a semi-log format to better demonstrate the modeling data that are related to an exponential relationship. The plot shows that at constant time, the progression of the isothermal line is retarded with increasing contact angles.

To disentangle other affecting parameters from contact angle, i.e., to ascertain the sole effect of equilibrium contact angle, we now non-dimensionalize the progression length with thermal diffusivity and time. The aforementioned similarity parameter is defined as thermal diffusivity divided by the square root of thermal diffusivity multiplied by corresponding progression time. We impose two different thermal conductivities of 0.58 and 1.61 (W/m.K). The former corresponds to thermal conductivity of water used in our previous models. Figure 5.8 shows the dimensionless progression length versus the wedge contact angle. The dimensionless length scale is shown as eta (η) and is characterized as:

$$\eta = \frac{\delta}{\sqrt{\alpha t}} \tag{5.2}$$

where t is progression time, and α is thermal diffusivity. The eta curves are more converged specially at low contact angles, implying the paramount effect of contact angle on delayed progression of solidified layer. As mentioned before, the interface between solid and liquid domains is not set to a constant temperature for previous models; however after assigning the interface to predetermined temperature of -20 °C and redo the simulations, the eta curves results are more exhaustive; that is, they emphasize the sole dependence of progression length to contact angle. Figure 5.9 shows the eta curves versus contact angles for thermal conductivity of water as the interface of solid and liquid domains is set to constant temperature of -20 °C. All of the eta curves collapse on each other indicating the sole dependence of progression length of the solidified layer on contact angles of the liquid wedge.

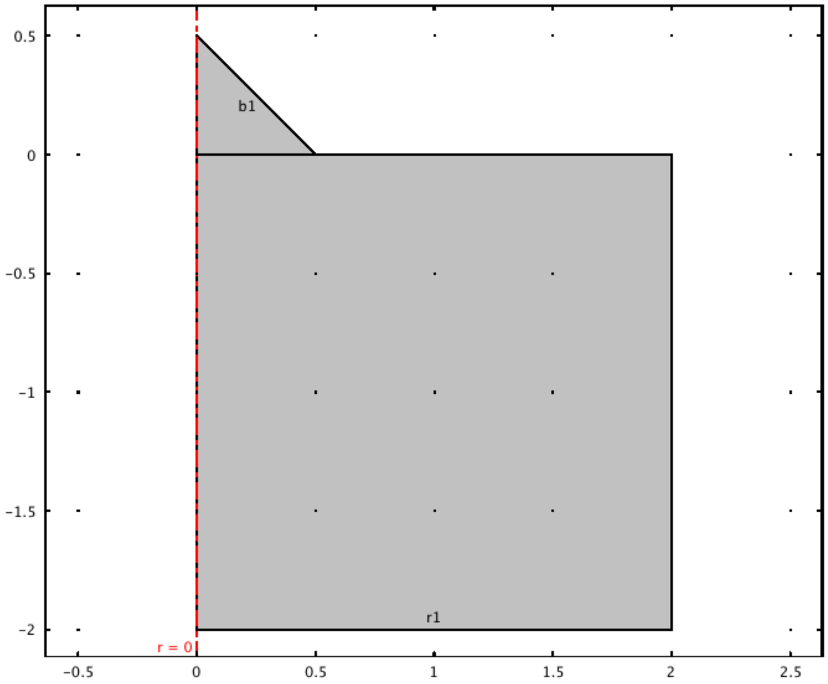

Figure 5.4: Geometry of a water drop with wedge-like liquid-gas interface, denoted by b1, on a solid glass target, denoted by r1. Horizontal and vertical axes are length scales in millimeters.

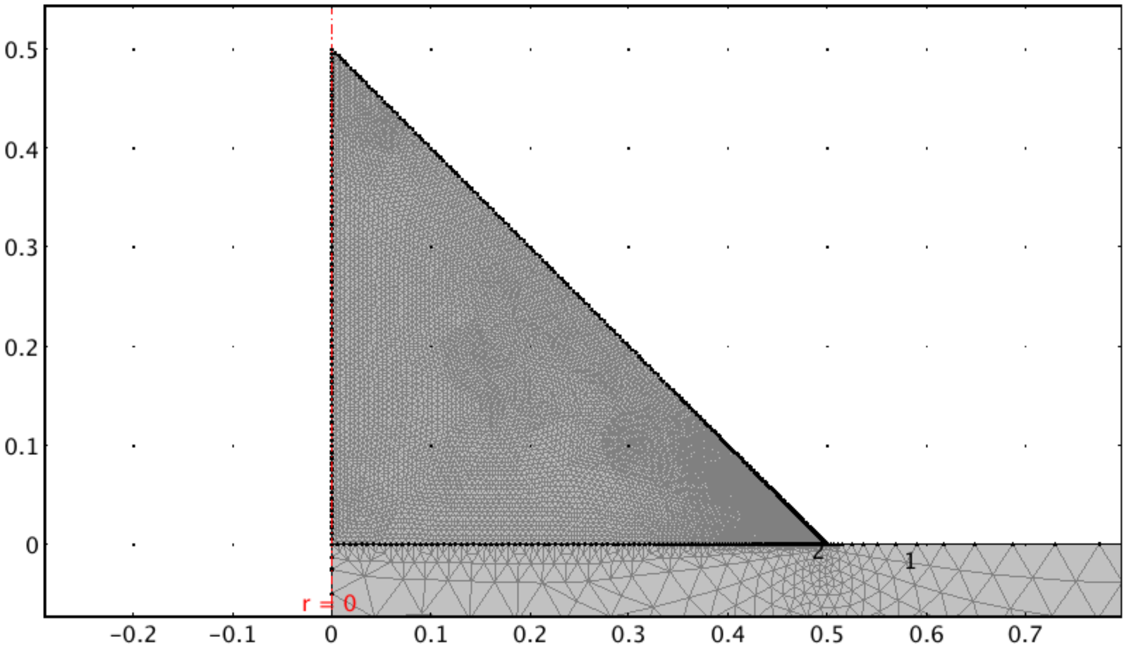

Figure 5.5: A typical mesh density in liquid domain. Horizontal and vertical axes are length scales in millimeters.

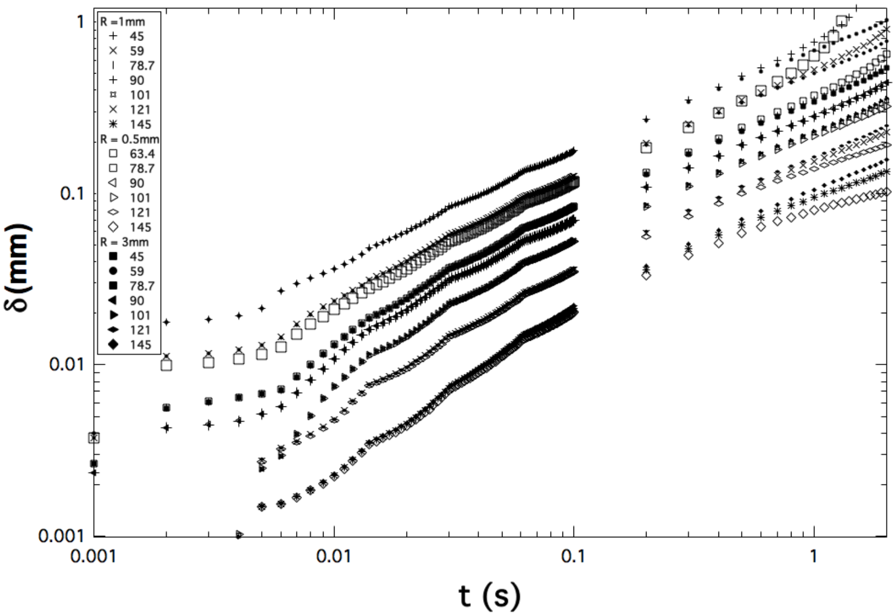

Figure 5.6: Progression length of the solidified layer along the liquid-gas interface versus time for different base diameter of the water drop (0.5 mm, 1 mm and 3 mm) and contact angles (45°-145°).

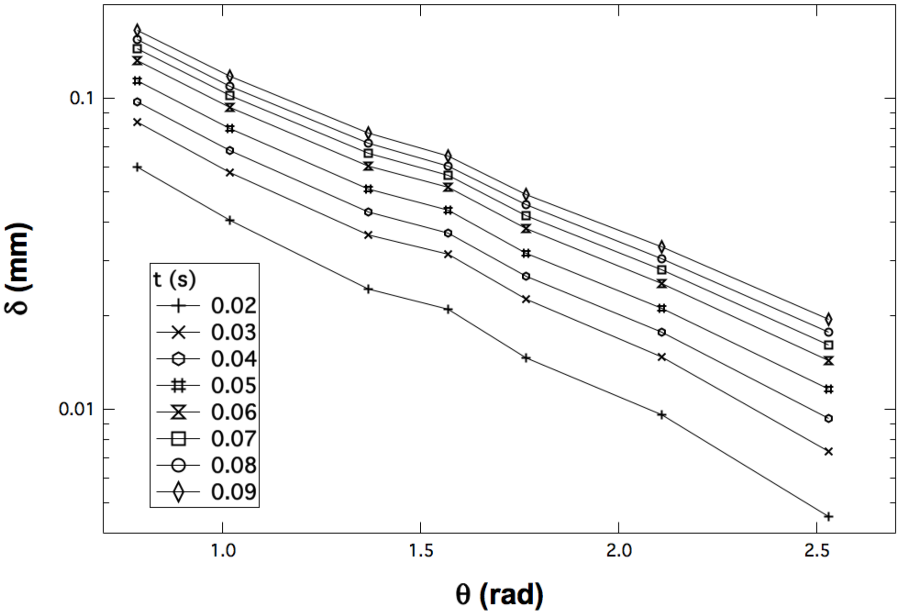

Figure 5.7: Solidified layer progression along the liquid-gas interface with respect to equilibrium contact angle for different progression times.

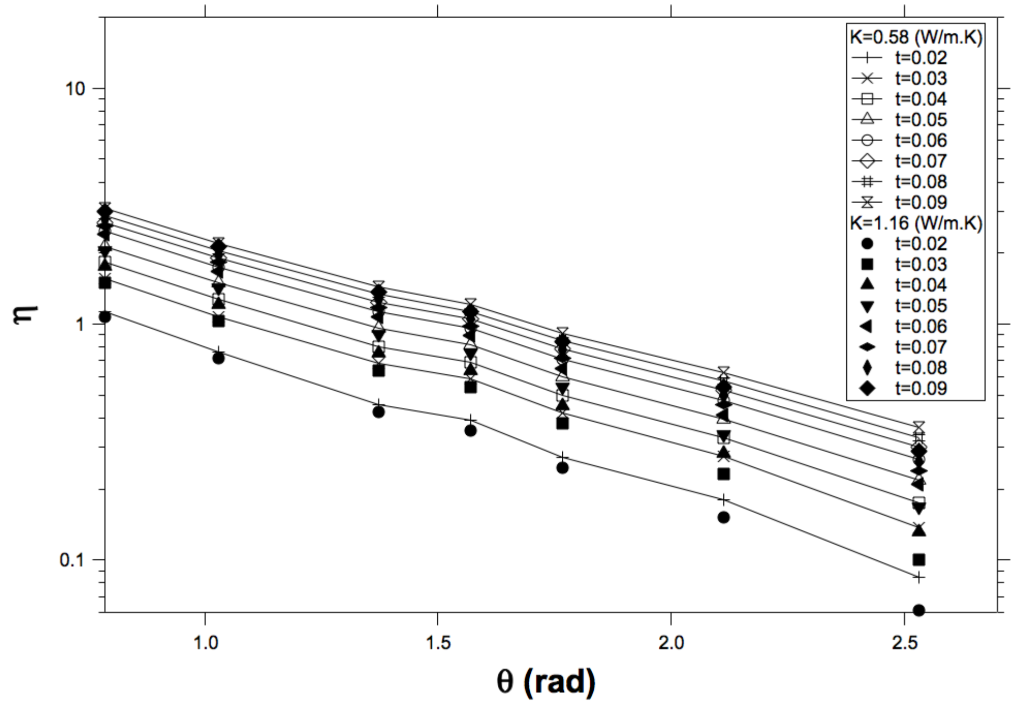

Figure 5.8: Dimensionless solidified layer progression, $\eta = \delta / \sqrt{\alpha t}$, versus equilibrium contact angle for two thermal conductivities at multiple progression times.

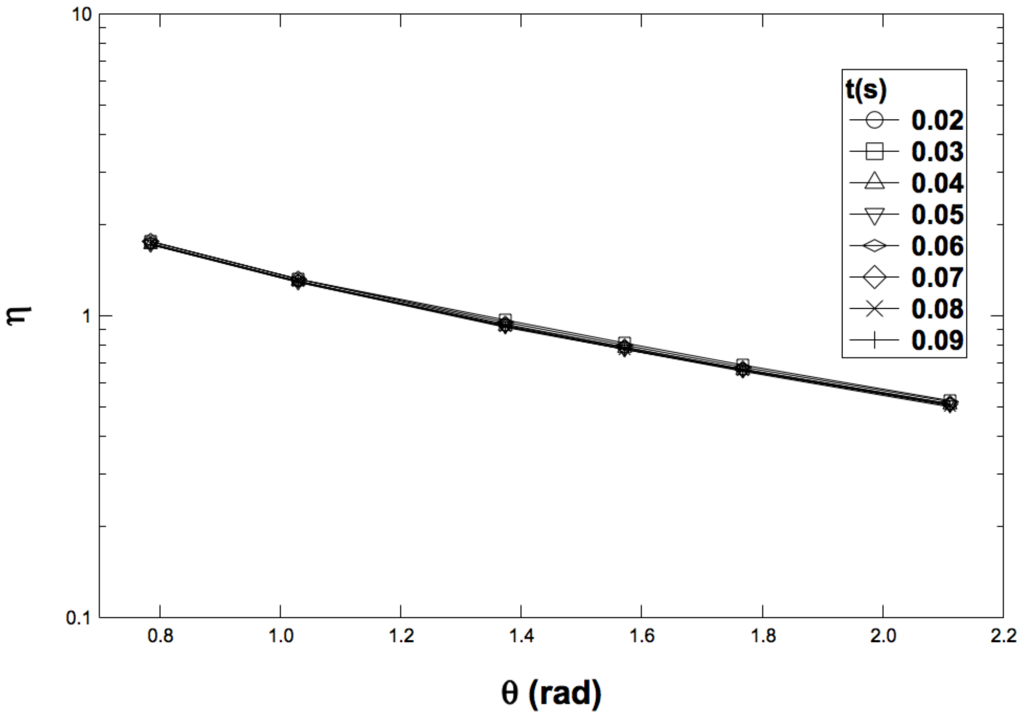

Figure 5.9: Dimensionless isotherm progression, $\eta = \delta / \sqrt{\alpha t}$, versus contact angle at multiple progression times with the fixed temperature (T=-20 °C) of the solid-liquid domains interface.

5.5 Conclusions

Freezing delay on hydrophobic surfaces is still a subject of debate between scholars. We conducted experimental and numerical studies of solidification delay on hydrophobic surfaces under forced and static conditions, respectively. In the experimental section, we performed the forced spreading experiments of water on cover glass substrates with temperatures of -10 °C and -20 °C at constant humidity. Spreading rate on the hydrophobic surfaces is slower due to high contact angle of these surfaces as compared to the hydrophilic ones. At -10 °C and small enough flow rates, the freezing inception is postponed on the hydrophobic surfaces with larger footprint. At very high flow rates, no solidification transpires on both surfaces, as cooling temperature is not adequate to initiate heterogeneous nucleation and freezing in the drop. At lower temperatures of the substrate and lower flow rates, water drops instantly freeze on both surfaces with larger footprint on hydrophilic surface, however higher flow rates transitions from instantaneous to delayed spreading regime yielding longer freezing time scales as compared to the hydrophilic cover glass. The sudden change of behavior could have implicit impact on ice adhesion of both hydrophobic and hydrophilic surfaces.

In addition, numerical analysis is conducted to assess the effect of contact angle on possible delay on freezing. Wedge-like form is postulated for the drop's liquid-gas interface on the cold solid substrates. Numerical studies unequivocally confirm that higher static contact angles postpones solidification inception of the static water drops, however, the difference in growth rate is immaterial. Hence, at constant time, solidified layer ascended less along the drop's liquid-gas interface for hydrophobic surfaces. Dependence of progression length on the base diameter of the drop is intangible. Non-dimensionalizing the progression length with square root of thermal conductivity multiplied by time, $\delta/\sqrt{\alpha t}$, resulted in converging of the curves as a function of equilibrium contact angle. This reflects the sole dependence of the solidified layer advancement with the equilibrium contact angle at the trijunction.

CHAPTER 6

Intermittent Freezing Stage of Supercooled Water Drops on Cold Substrates: Initiation and Mechanism

6.1 Introduction

The process of cooling a liquid below its melting point without phase change, supercooling, followed by solidification is of paramount interest for many engineering applications and in nature. Casting, for instance, in which liquid material is poured into the mold and allowed to solidify is one. In splat quenching, meta-stable and improved structural properties are obtained by extremely rapid cooling of molten materials [115,116]. In addition, temperature transitions of freezing drops and the crystallization of watery and fatty phases in food systems can determine food quality [117]. Most of the drop solidification research, particularly for water, phase change is assumed to occur at equilibrium freezing temperature; however, this is not always the case. When supercooling of a liquid drop exceeds few centigrades, the process of freezing splits in four distinct stages: i) liquid droplet cooling, ii) stage-one freezing (also known as recalescence among metallurgists), iii) stage-two (main) freezing, and iv) solid droplet cooling [118-120]. Figure 6.1 schematically shows the temperature versus time during these four stages. Melting point of the supercooled liquid is denoted by T_m under a vertical dashed line. During the recalescence stage, 7 to 18 wt% of the water, depending on the degree of supercooling, is found to get solidified by using a Nuclear Magnetic Resonance (NMR) technique [120]. This stage is ceased when the supercooling is exhausted and the droplet has reached its equilibrium melting temperature. Percolation of the hydrogen-bonded water network was introduced as an explanation of this ultrafast temperature rise during recalescence [108]; However, no supporting evidence was provided. Moreover, the recalescence stage is still not well understood in terms of initiation mechanism.

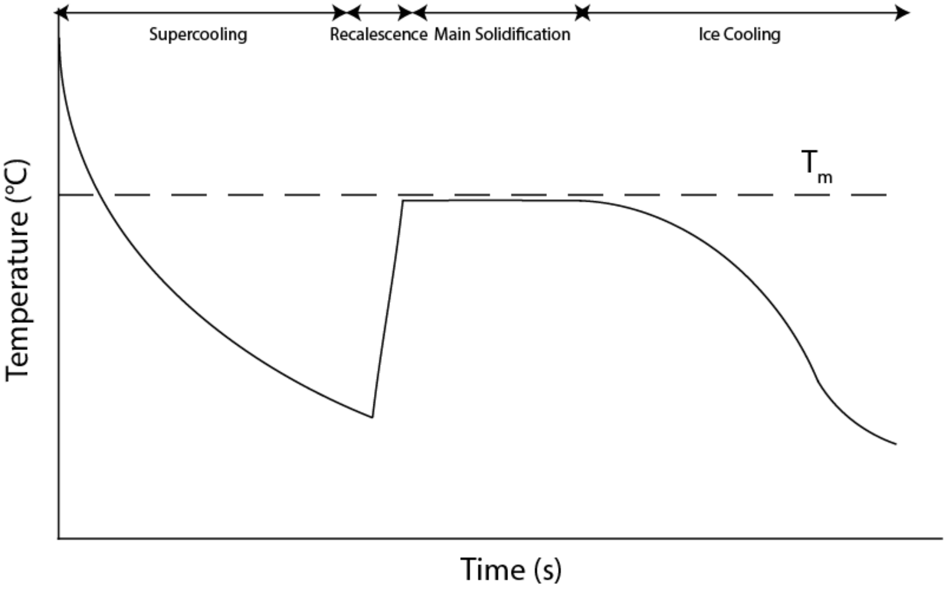

Figure 6.1: Cooling stages of supercooled liquid.

There have been many studies on the nucleation of subcooled melt in literature. These studies usually concern droplets suspended in air [121] or attached to a solid [118,122]. The research on ice nucleation is mostly motivated by the formation of snow crystals, commonly revolves around the dynamics of crystal growth from gaseous phase [123]. For the case of recalescence of water droplets on a substrate, some experiments showed that nucleation occurs preferentially at the trijunction point, supporting energetic arguments that an ice nucleai at the contact line leads to a reduction in the nucleation barrier energy [124,125]. Most recently, a study on freezing supercooled water on a homogenous silicon substrate concludes that there is no preference for nucleation at the trijunction point [122]. By avoiding substrate cooling and using low cooling rates, their design eliminates temperature variations in the drop. Air itself was used to cool the drop and substrate inside of an isothermal container. Ice nucleation and freezing of acoustically levitated drops was analyzed [121] and it is asserted that ice nucleation from surface is dominant. While high-speed IR imaging during freezing delivers a temperature data of the droplet surface, high-speed recording provides visual data about freezing both at the surface and in the drop interior. In contrast, immersion nucleation, also know as volume–dominated nucleation has also been reported for levitated micro drops [126]. In sum, there is no clear consensus on the nucleation mode of supercooled drops.

Further understanding of the recalescence stage for undercosoled liquid, in terms of dynamics and structure, can possibly unveil a strong influence of this stage on the solidification of static or spreading drops. Furthermore, in many fluids-mechanical research and experimental studies on the freezing of supercooled drops, whether static [58] or dynamic [25], the recalescence stage has not been considered. More importantly, elapsed time to recalescence stage (duration of supercooling stage) has not been quantified.

6.2 Experimental Setup

In our experiments, glass slides with dimensions of 50×24×0.15 mm^3 (VWR microcover glass) are rinsed successively in acetone, methanol and DI water. Plasma cleaning is not performed so that the full wetting of liquid is prevented. The slides are situated on top of a Peltier element with dimensions of 90×90×12 mm^3 which is capable of reaching temperatures as low as -30 °C. Liquid drops are positioned on top of the Peltier plate using a motorized injection needle. Afterwards, water drops ranging from 3.9 mm to 6.8 mm, are cooled by the Peltier element. A camera (Phantom IV series) is used to view events from the side and top of the water drops. The camera is capable of recording events with maximum speed of 1000 frames per seconds. From captured images, we can locate the temporal and spatial origin and track the propagation of the freezing front. The horizontality of a stage is carefully checked before the experiments using a spirit level. Temperature readings of the temperature controller are accurate to ±0.3 °C established by FLIR A600-series thermographic camera and k-type thermocouple. The main stage, on which the Peltier element and glass substrate are situated, can be moved in x, y and z directions. To monitor surface temperatures of freezing static drops, k-type thermocouple is immersed at the apex of the water drops. Data collection rates are set to 10ms to capture temperature evolution during recalescence. FLIR® A600-series infrared camera was used as a complementary thermal mapping technique to monitor the supercooling stage of the drops from the top view. The IR camera was situated 10cm above that substrate surface and emissivity of the camera was set to 0.95. The videos are recorded with resolution of 640×480 and frame rate of 25Hz.

6.3 Experimental Results

Solidification of the supercooled water drops is recorded using a CCD camera. The full sequence from the cooling of the water drop to the solidification completion is shown in Figure 6.2. When the water drop is being cooled by the cold glass substrate substantially below its melting point (Figure 6.2.a), recalescence occurs prior to the main solidification stage and a shell-like structure forms throughout the drop (Figure 6.2.b). After recalescence, a slower solidification step, driven by the heat conduction toward the solid-liquid interface ensues and the fusion interface starts to ascend through the water drop (Figure 6.2.c) until the solidification is completed. When the last fraction of liquid at apex turns into ice, a singular tip develops spontaneously due to expansion of water upon freezing and distinct trijunction conditions [58,127] (Figure 6.2.d). The water drop solidification followed by cusp formation are also clearly shown, excluding recalescence, experimentally[128-130] and numerically[128,130].

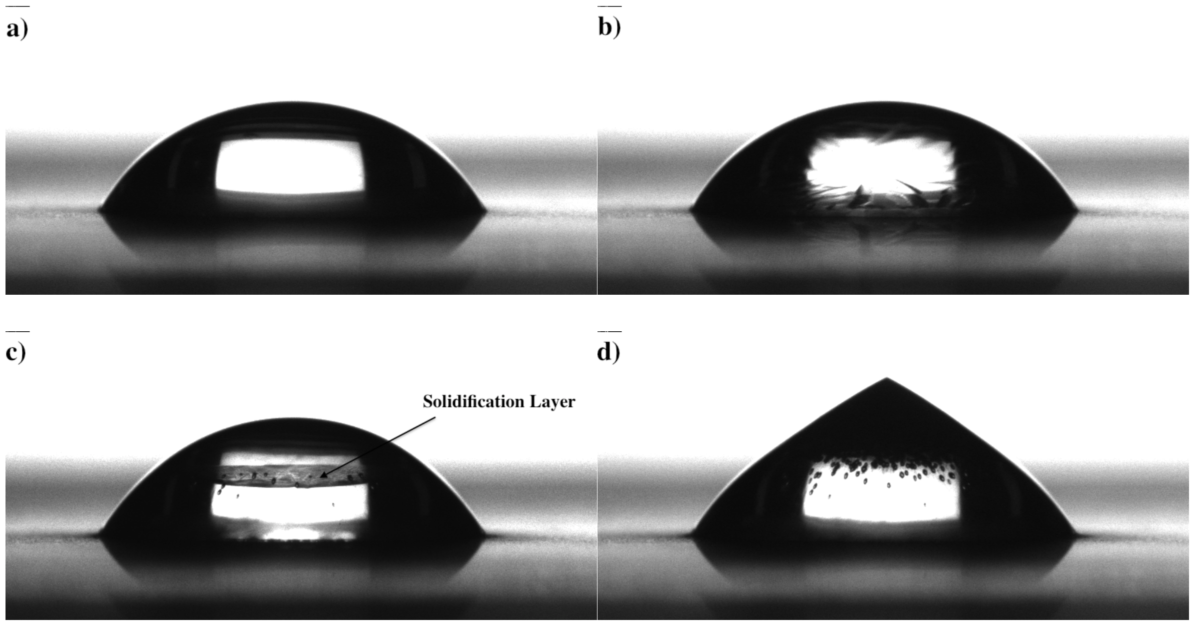

Figure 6.2: Freezing sequence of a water drop with 4.8 mm diameter on a -15 °C glass solid substrate. a) prior to drop solidification, b) recalescence, c) ascending of the solidification layer, and d) solidification completion with cusp formation.

New set of experiments was organized to look closely into origin of this kinetics driven phase change (recalescence) and the speed of nucleation front. For this, different sizes of water drops were positioned on either hydrophobic or hydrophilic substrates and cooled by a Peltier element to temperatures ranging from 0 °C to -25 °C. It should be mentioned that water drops and substrate are cooled simultaneously from 25 °C to designated temperatures; As opposed to the other common case of cooling, when 25 °C water drops are deposited on a cold Peltier element. No solidification occurred when water drops were cooled to -10 °C because of water ability to undergo supercooling. The barrier energy for heterogeneous nucleation is not reached by small amount of cooling energy at these temperatures. In most of the cases, recalescence starts when the substrate temperature reaches -20 °C. Recalescence renders the water drop fully opaque without any further noticeable light transmittance; therefore, the recalescence front can be accurately located during its propagation. It is worth mentioning that rejection of gas by the ice has been attributed to the change of the refractive index during recalescence[131]; however, no bubbles were observed during our experiments.

Figure 6.3 depicts the results of the front speeds versus undercooling temperatures. The recalescence videos are processed using MATLAB and the recalescence edge is tracked between two consecutive frames. The temperatures shown in the Figure 6.3 correspond to the temperature of the Peltier element at the moment of recalescence initiation. Closed filled data points represent recalescence front speed on hydrophobic surfaces, whereas open markers show hydrophilic ones. The morphologies of the recalescence fronts are written in the legend of Figure 6.3. The nucleation front speed increases monotonically with lowering substrate's temperature due to increased thermodynamic driving force. The velocity of the recalescence front can be roughly related to undercooling by a power function of:

$$V \sim \left(\Delta T\right)^2 \tag{6.1}$$

where V is the velocity of the solidification front in *mm/s*, and ΔT is degree of undercooling in °C. This power law relation has been introduced between dendritic growth rate and degree of undercooling for nickel [132] and aluminum [133] undercooled melts.

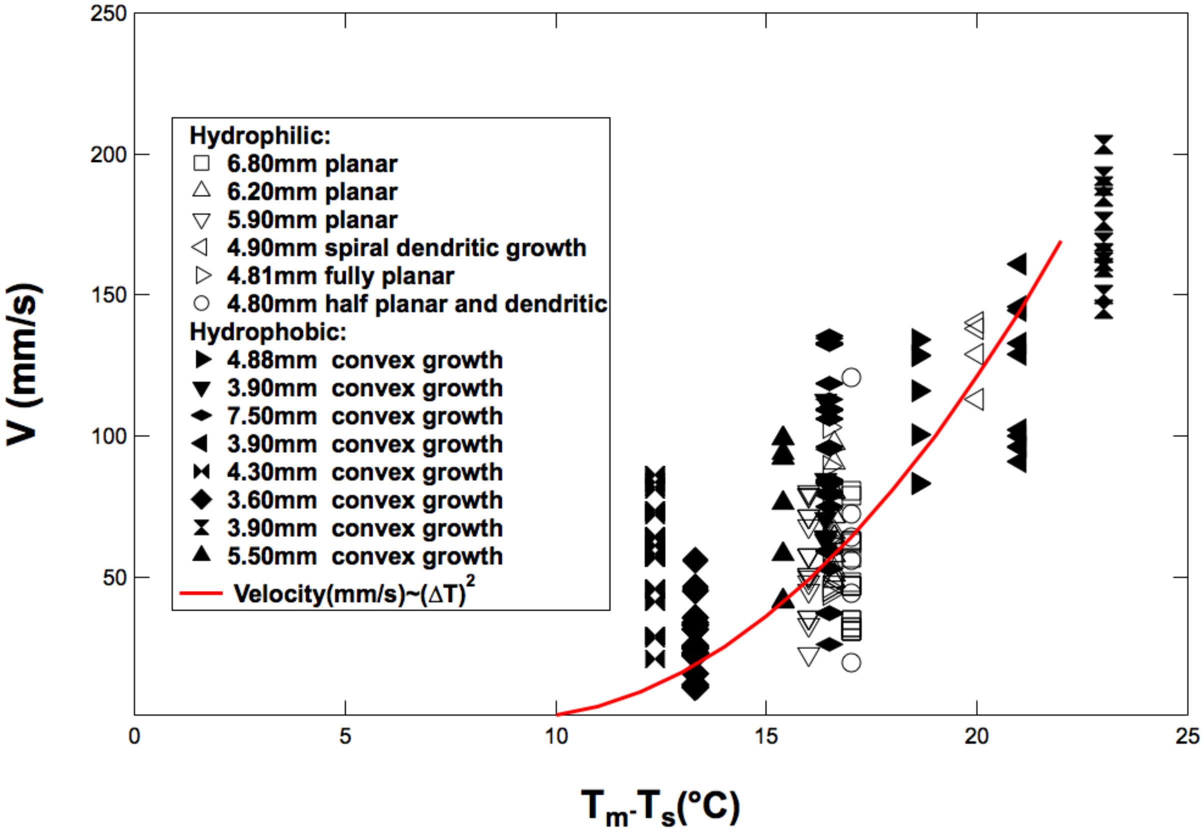

Figure 6.3: Recalescence speed of water drops versus supercooling temperature. Solid line represents a parabolic equation fitted to the data. Closed filled data points represent hydrophobic speed values, whereas open markers show hydrophilic ones.

Dramatic variations have been seen in crystal morphology of ice from vapor phase [123] and liquid water [134] as a function of temperature and supersaturation. Full understanding of the crystal growth has not been reached due to interaction of large-scale physics, microscale dynamics, and stochastic nature of non–equilibrium solidification. Here, we monitored the structure of the recalescence front using a CCD camera. Morphological structure of solidification front differs for different substrate's hydrophobicity and temperature. Recalescence front on all cases of hydrophobic surface exhibits convex growth microstructure (Figure 6.4), however on the hydrophilic surfaces morphologies of recalescence front varies as: i) planar front (Figure

6.5), however, parallel branching at the front edge is visible, ii) half planar growth followed by half dendritic front and iii) dendritic growth (Figure 6.6). Dendritic morphology is formed owing to negative temperature gradient in a water droplet leading to amplification of local instabilities.

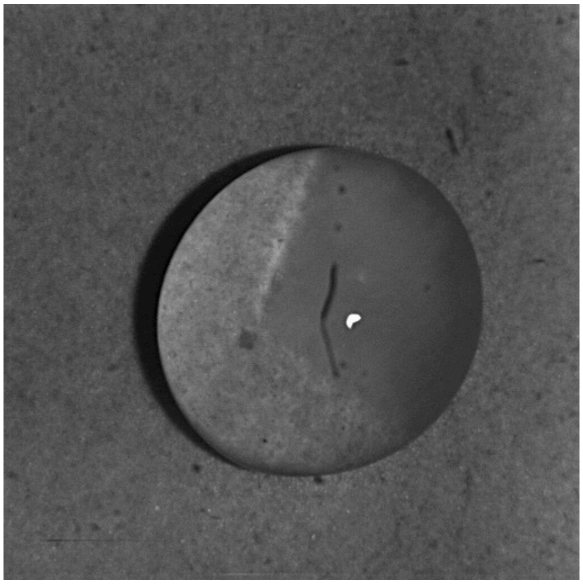

Figure 6.4: Solidification front of a water drop with diameter of 4.8 mm on a hydrophobic surface.

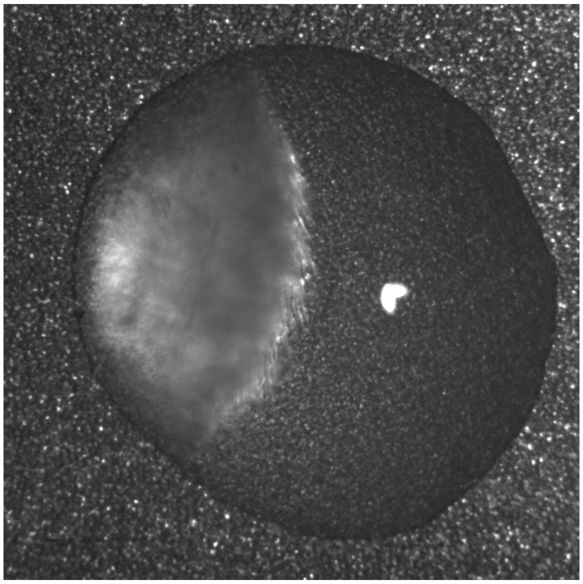

Figure 6.5: Solidification front of a water drop with diameter of 6.8 mm on a cover glass.

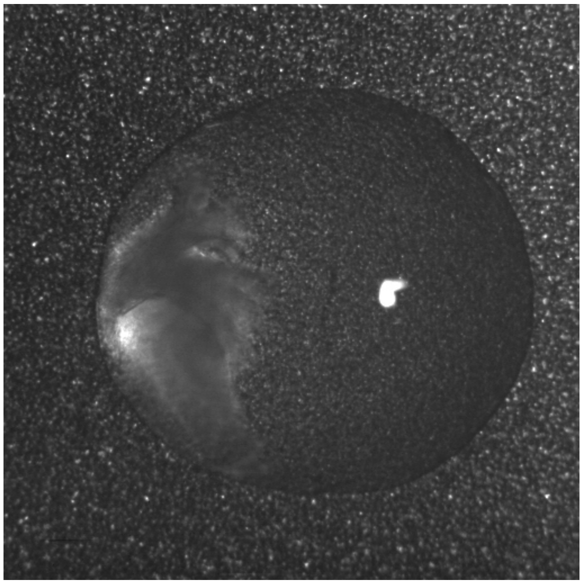

Figure 6.6: Solidification front of a water drop with diameter of 4.9 mm on a cover glass.

Recalescence of water drops on cooling solid targets always initiated at the trijunction point and extended radially toward the bulk of water drops. Figure 6.7 shows the progression of the recalescence front from top and side views for two water drops on a clean, but not plasma treated, hydrophilic glass substrate. Drop diameter for side and top views are 3.2 mm and 4.7 mm, respectively. From the initiation of recalescence front to the stage completion lasted 0.5 s for both cases. During recalescence, the water drops are pinned down and base diameters remain unchanged; however, there is 8.62% increase in drop volume after recalescence. This volume expansion is measured by superimposing before and after recalescence frames, shown in Figure 6.8, using ImageJ software. This expansion of drop's outline corroborates the partial solidification of liquid drop by the recalescence stage, as freezing of water is accompanied by volume expansion in an open hexagonal form.

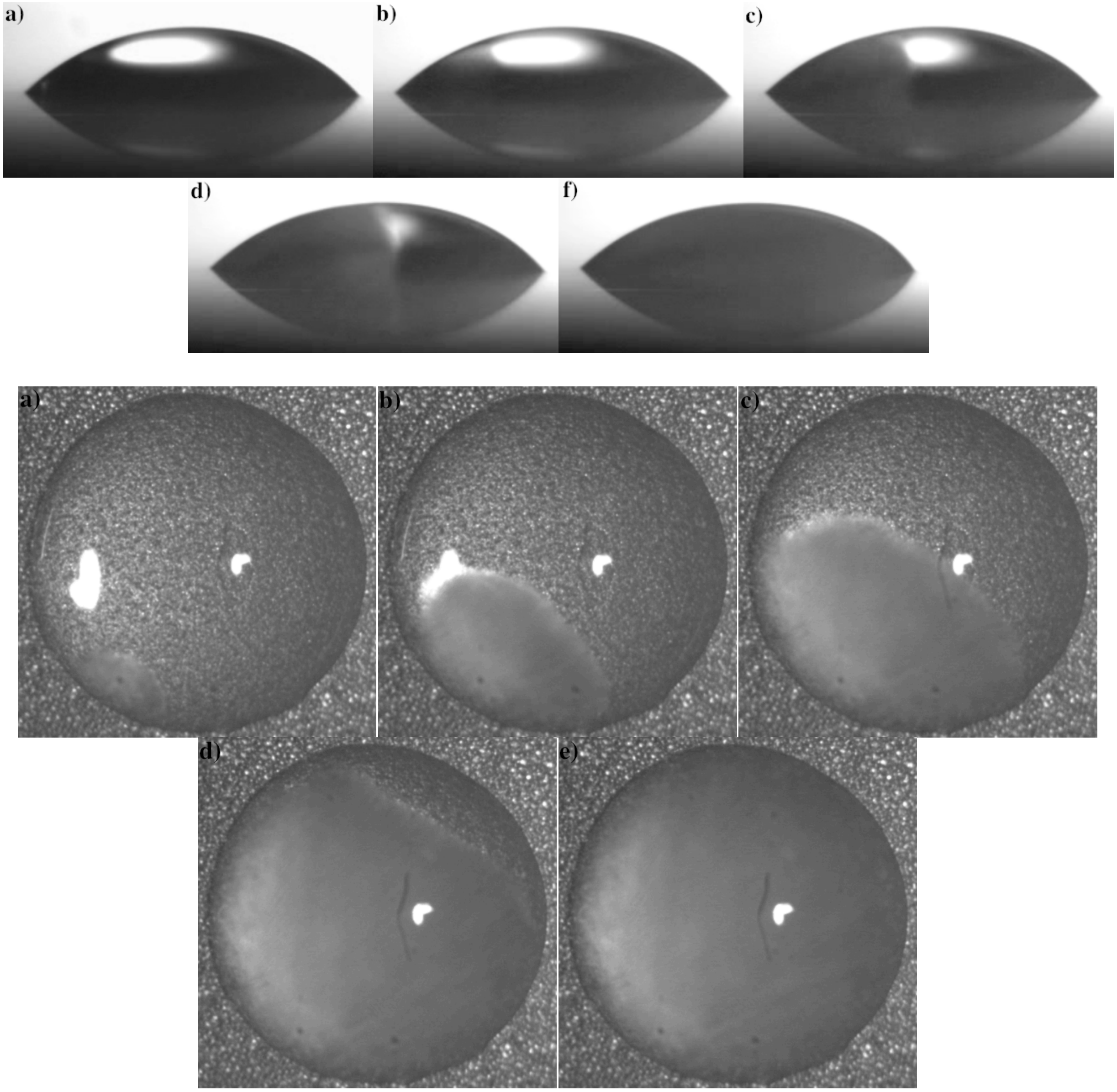

Figure 6.7: Recalescence front progression from side and top view (a-e). Recalescence front initiated from a trijunction line and propagated radially through the drop volume. Drop diameter for side and top views are 3.2 mm and 4.7 mm, respectively.

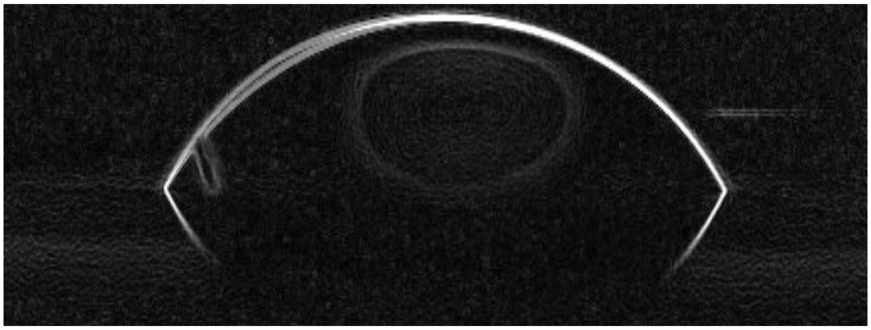

Figure 6.8: Two superimposed frames of before and after recalescence of a water drop on a glass substrate with temperature of -20 °C. Recalescence initiated from the right side of the water drop and propagated through the volume.

In our experiments, the cooled drops on both hydrophilic and hydrophobic surfaces undergo the well-known cooling stages: i) supercooling, ii) recalescence, iii) main solidification stage at constant temperature, and iv) ice cooling (Figures 6.9 and 6.10). The thermal measurements are acquired using a k-type thermocouple submerged just below the drop's apex. The temperature data, with acquisition rate of 5 Hz, of the drop's apex versus time for a drop with 2.23mm diameter on a cover glass is shown in Figure 6.11. The inset shows the region at which sudden latent heat is released followed by main solidification stage and ice cooling stage. Both figures 6.9 and 6.10 show the interpolated data values by cubic spline method and the data points shown are reduced for more visual distinction. Generally, a cubic spline curve is defined as a piecewise cubic curve with continuous second derivative. Cubic spline method is preferred over polynomial interpolation, as polynomial interpolation tends to construct distortions at the edges, which in our case, the edges correspond to the overshoots at the recalescence stage. Supercooling temperatures are reached in the range of -13 °C to -17 °C. The recalescence stage duration is less than 20 ms, in which the drop becomes completely opaque (Figure 3.f). During recalescence, temperatures of the drops rapidly return to the solid-liquid equilibrium temperature. The main solidification stage, which starts with rise of an ice sheet from the basal plane and finishes after cusp formation on top of the ice, is strongly dependent on drop size. Larger drops yielded longer solidification times ranging from 27 s to 217 s for a drop diameter of 2.27 mm to 15.52 mm on hydrophobic surfaces, respectively. Duration of all the stages on both hydrophobic and hydrophilic surfaces is listed in tables 3 and 4. Standard deviations for each stage are also included; however, variations for the supercooling stages are large rendering them insignificant statistically. At the main solidification stage, droplet temperature would be independent of time. Right after cusp formation, the ice droplet cooling starts and lasts longer for larger drops. In addition, main solidification stage lasts longer on hydrophobic surfaces as compared to hydrophilic ones. For instance, the main solidification period for water drop with 2.24 mm diameter on the hydrophobic surface is approximately one order of magnitude longer than the one on the hydrophilic surface. This implies that solidified layer growth rate in hydrophobic surfaces is slower than hydrophilic ones. However, no conclusive relationship can be made regarding the duration of the supercooling stage with drop size, wetting characteristics of the surface. This randomness of time-to-recalescence is yet to be understood.

Table 3: Duration of cooling stages for water drops on hydrophilic surfaces.

Drop Diameter (mm)	Supercooling Stage	Recalescence Stage	Main Solidification Stage	Ice Cooling Stage
2.53	601.23	10ms	5.0±0.3	2.3±0.3
3.41	425.53	10ms	4.8±0.4	2.8±0.6
6.8	599.13	10ms	22.1±2.1	15.1±2.0
13.26	363.56	10ms	39.1±2.8	21.0±2.1
22.47	432.45	10ms	52.3±3.8	26.5±1.9

Table 4: Duration of cooling stages for water drops on hydrophobic surfaces.

Drop Diameter (mm)	Supercooling Stage	Recalescence Stage	Main Solidification Stage	Ice Cooling Stage
2.24	509.33	10ms	25.4±1.8	37.3±2.3
3.17	442.75	10ms	69.3±2.2	49.9±2.4
6.60	413.37	10ms	151.3±6.8	61.6±3.8
9.85	550.69	10ms	151.3±4.2	68.1±3.8
11.97	480.32	10ms	162.7±6.8	74.2±4.1
15.52	392.68	10ms	233.1±5.8	97.0±4.8
16.96	411.18	10ms	235.5±4.8	138.0±4.0

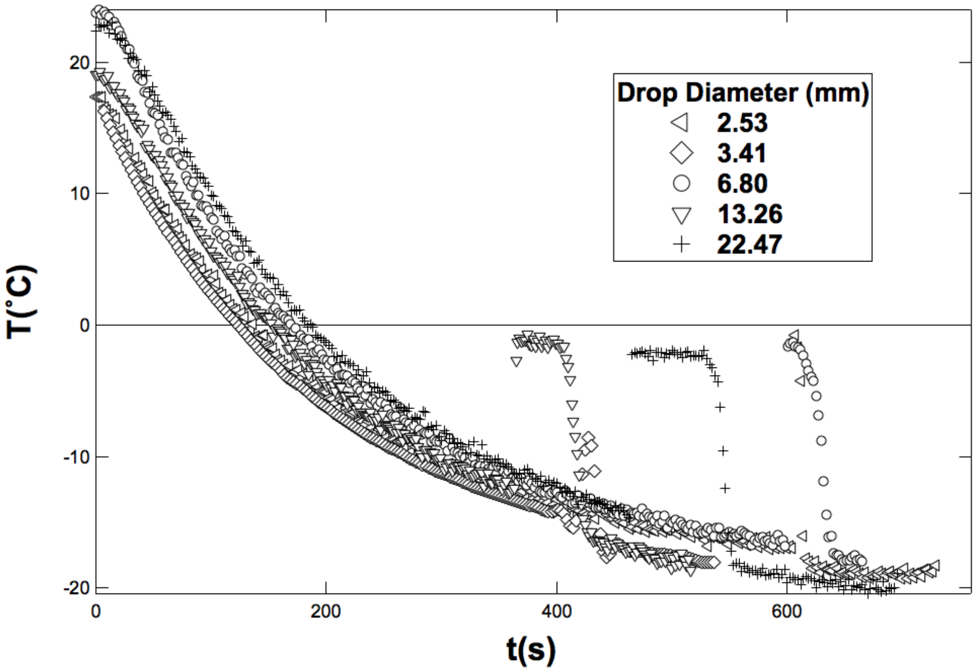

Figure 6.9: Evolution of the surface temperature of cooling water drops versus time on a hydrophilic surface (cover glass) measured by a k-type thermocouple for multiple drop sizes.

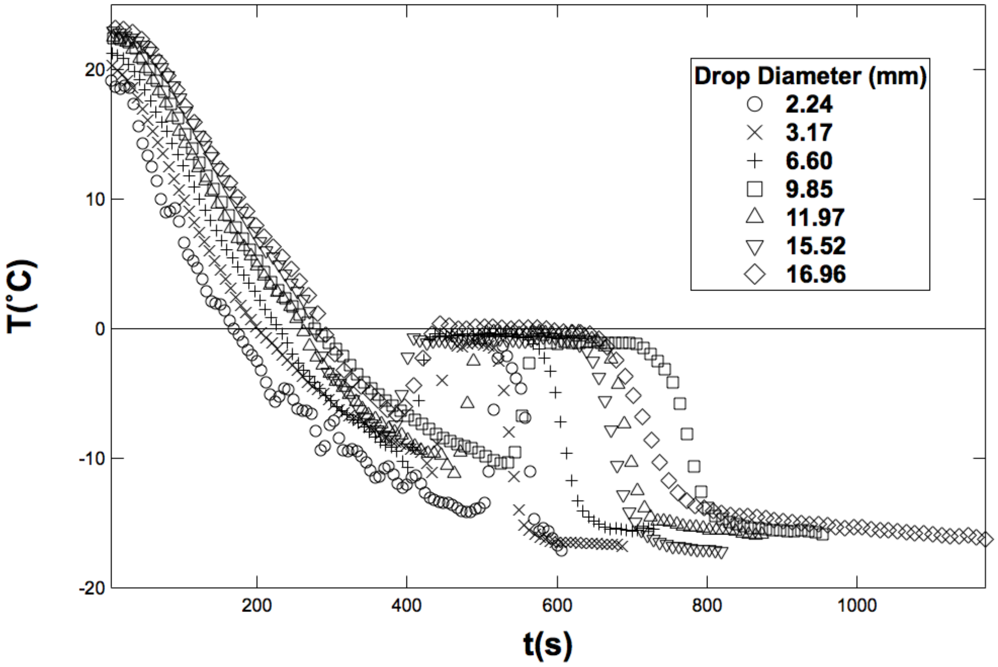

Figure 6.10: Surface temperature of cooling water drops versus time on a hydrophobic surface (WX2100TM spray on cover glass) measured by a k-type thermocouple for multiple drop sizes.

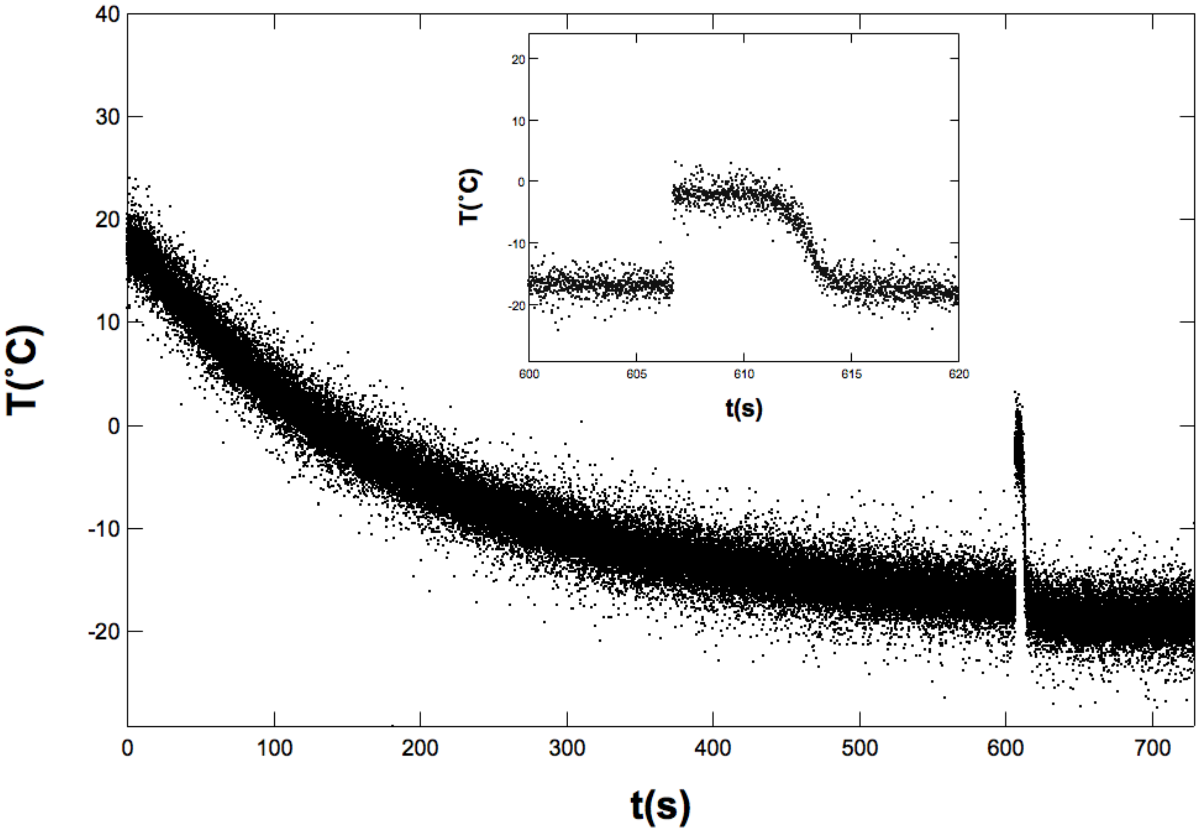

Figure 6.11: Surface temperature (acquisition rate = 5Hz) acquired by a k-type for a cooling water drop with diameter of 2.53 mm versus time on a cover glass surface. The inset shows the magnified recalescence region at which sudden latent heat is released at *t* = 606.27 s.

6.4 Triggering Mechanism of Drop Solidification

As mentioned in the previous section, the cooling stage of water drops (time from cooling to drop freezing initiation) are not dependent on substrate temperature, drop size and the substrate hydrophobicity. In order to attain more knowledge on the governing parameters on the solidification initiation, we decided to monitor the nucleation event from the top using FLIR® A600-series infrared camera as a complementary thermal mapping technique. As like for previous experiments, water drops were deposited on solid substrates and cooled to temperatures below the melting point of water, however at relative humidity of 48 RH%. The IR camera was situated 10cm above that substrate surface and emissivity of the camera was set to 0.95. Videos of recalescence stage were recorded and a video sequence is shown in Figure 6.12. Darker regions in Figure 6.12 correspond to colder temperatures. During cooling stage, condensation of microdrops ensues all over the glass substrate. In larger areas, recalescence of micro-condensed drops surrounding the main “mother” drop manifests itself in a wave-like “front” movement (Figure 6.12.a). The direction at which this front approaches the main drop is non-deterministic, as every experiment resulted in random direction of the front progression. This front seems fairly straight with some instability-induced bumps. The moment, at which the recalescence front reaches the drop circumference, recalescence is triggered in the main drop, as illustrated in Figure 6.12.b, and propagates through the drop bulk (Figure 6.12.c). In return, the main drop’s recalescence (Figure 6.12.d), sets off recalescence of surrounding drops close to the drop (Figure 6.12.e) which continues to move away radially from the main drop (Figure 6.12.f,g). This clearly explains the data inconsistency of time to recalescence initiation, as condensed drops’ wave-like recalescence motion dictates the main drop’s freezing initiation. This observation will open new discourse regarding the solidification of the drops in contact with foreign solid substances, as condensates, especially at higher humidity, on solid target could potentially set off the solidification initiation.

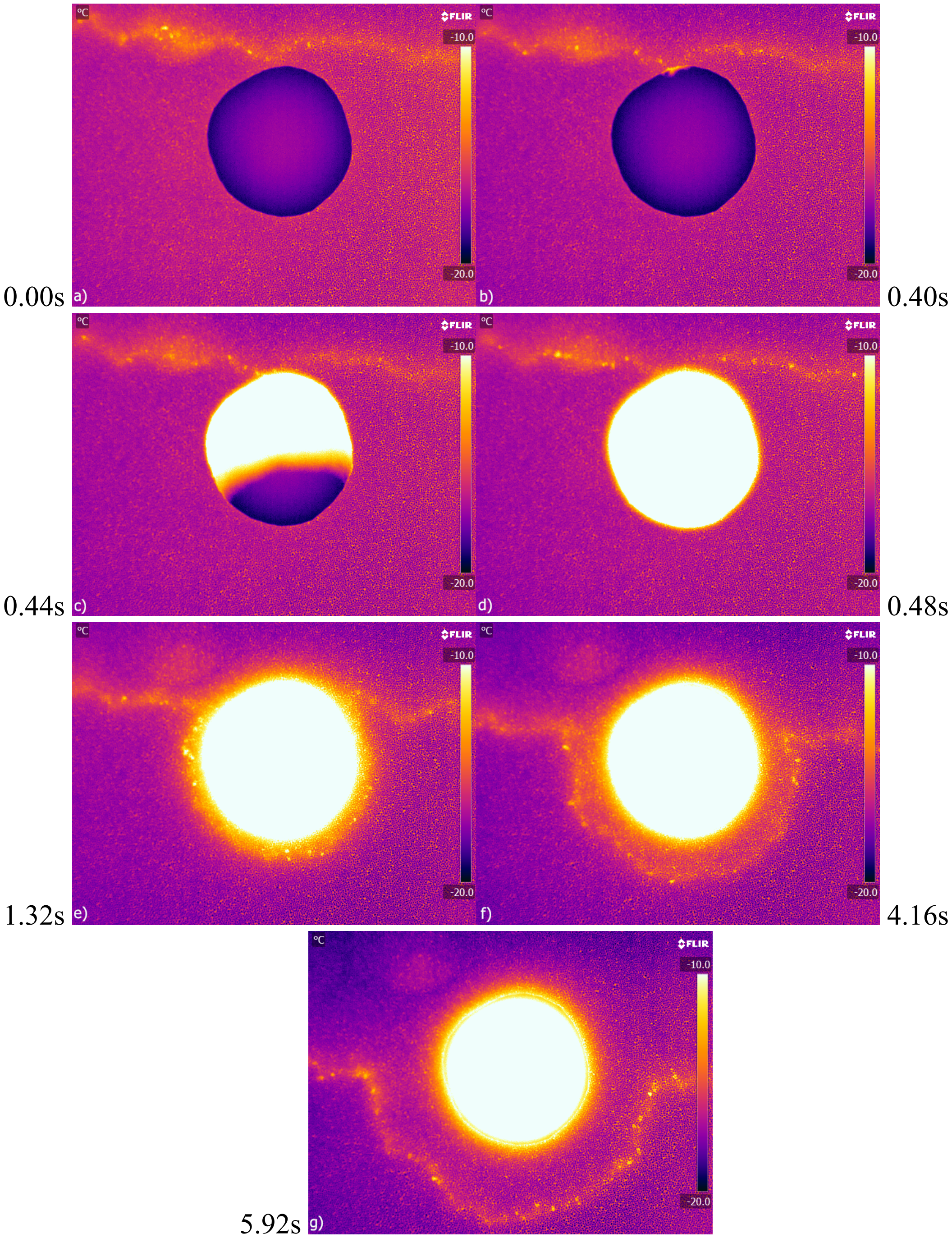

0.00s 0.40s 0.44s 0.48s 1.32s 4.16s 5.92s

Figure 6.12: Recalescence sequence of the main drop with diameter of 5.5 mm on -20 °C glass substrate and surrounding micro-condensates.

6.5 Conclusions

Freezing stages of static supercooled liquids by cold solid hydrophilic and hydrophobic substrates were investigated. Using a high-speed camera, we observe a well-known intermittent kinetics-driven stage (recalescence) prior to the main freezing stage whose freezing speed is in the range of 50-150 mm/s. The presence of this stage is confirmed from the temperature measurements acquired by k-type thermocouple and IR camera, at which cooled drops reached zero °C in less than 20 ms and maintained that value until the main solidification interface fully covers the drop from the bottom plane to the top. In all of our 76 experiments, the nucleation front initiates from a point on the trijunction and propagates into the drop volume with different structural morphologies determined by cooling temperatures and surface hydrophobicity of the solid target. The morphology of the recalescence front varies from planar to dendritic growth depending heavily on the substrate temperatures, whereas on hydrophobic surfaces, the recalescence interface maintains a convex, yet stable, front.

After completion of the main solidification stage, cooling of ice commences. The duration of both the main solidification and ice cooling stages are highly dependent on the drop size. However, no conclusive relationship could be made regarding the duration of the supercooling stage with the drop size and the surface hydrophobicity from the thermocouple measurements. The duration of the supercooling stage is found to be dictated by the collective recalescence of condensed micro-drops surrounding the main drop that manifests itself in a wave-like “front” movement. This front seems fairly straight with some instability-induced bumps. The moment at which the recalescence wave reaches the main drop circumference, recalescence is triggered in the main drop. This observation explains the data inconsistency of the time to recalescence initiation, as condensed drops wave-like recalescence motion dictates the main drop’s freezing initiation. This observation will open new discourse regarding the solidification of the drops in contact with foreign solid substances, as condensates, especially at higher humidity, on the solid targets could potentially set off the solidification initiation.

CHAPTER 7

Cold-induced Spreading of Water Drops on Hydrophobic Surfaces

7.1 Introduction

Hydrophobic surfaces are universally used for their unique, and supposedly perpetual, self-cleaning properties, as water droplets roll along theses surfaces rather than spread. In addition, there have been many studies in the last decade on the capability of hydrophobic surfaces to induce a significant delay on freezing or ice adhesion reduction at extreme cold conditions [100-106]. Many factors such as insulating properties of these surfaces [101], less probability of heterogeneous nucleation and reduction of water-solid interfacial [107,108] area have been attributed to these unique features. In practice, the efficiency of the hydrophobic surfaces under conditions of extreme humidity, airflow [104], particle diameter of the hydrophobic surface [97], icing/deicing cycles [111], and frost formation [105] is critically questioned.

External stimuli could impart distinctive properties to either the liquid or the hydrophobic substrate and change the wettability characteristics. For the case of liquid, trisiloxane polyoxyethylene surfactants, also known as superspreader, are added to water-based solutions prompting early spreading on the hydrophobic surfaces. Two mechanisms of decreasing the interfacial tension of solution/solid and marangoni flow have been suggested; nonetheless the definitive underlying mechanism is still a mystery [135]. This property is directly being employed for water–based coatings in plastics, surface modifiers in fabrics and cleaners [136,137]. In addition to liquid, substrate's wettability of hydrophobic surfaces can be tuned by external parameters such as light [138], temperature [139], magnetic field [140] and electrical voltage [141].

Imposing temperature gradients has been recently introduced to alter hydrophobic substrate's wettability. The early studies on thermal manipulation of surface wettability was conducted by Sun et al [142]. Crevosier et al. [143] used a polymer which undergoes phase transition between organized and the disorganazied state under exposure to temperature gradients. Chao Li et al. [139] introduced a specific hydrophobic surface that induces reversible liquid contact-angle change with change of temperate. This change of contact angle resulted from the change of the interfacial interaction caused by the crystal-to-amorphous phase transition.

More specifically, geometrical characteristics of the water drop, i.e. contact angle and base diameter, on cooling hydrophobic surfaces, which determine icephobicity and freezing delay, have been explored briefly in literature. Huang et al. unveiled the strong relationship between the contact angle and base diameter of the water drops with droplet freezing time [144]. The larger the contact angle is, the longer the freezing time. Despite the obvious relevence of contact angle and base diameter of the drop to the ice adhesion [98,145-147] and freezing time of the supercooled drops, systematic investigation on wetting dynamics of water drops on hydrophobic surfaces during the cooling stage, prior to freeezing initiation, have not been conducted. A few studies about thermal stability of hydrophbic surfaces have been published. One claimed [148] that decreasing temperature gradually increased the wettablity of almost all hydrophobic surfaces, whereas, in contrary, Wang et al. [149] reported that hydrophobicity remained stable at temperatures as low as -5 °C.

When liquid drops are deposited on hydrophobic surfaces and cooled to the temperatures below RT, net force balance at the trijunction predicts, in ideal scenario, that introducing coldness to the solid substrate will increase the surface tension of the liquid/gas interface and cause the drop to recede leading to smaller base diameter and higher contact angle (Figure 7.1). However, we observed a new phenomenon, in which introducing negative thermal gradients between the hydrophobic substrates and the deposited water drops triggers depinning and subsequent spreading of the drop. The hydrophobic surfaces, on which water drops are deposited, were cooled by a Peltier element to cold temperatures to accurately observe the phenomenon by DSA100. Peltier element is a thermoelectric device, which transfers heat from one of its sides to the other when electricity is applied. Amplifying the voltage across the thermo-electric heaters increases the temperature of the Peltier element. The cold side is then brought in contact with the substrate and cools it to a chosen temperature before the water liquid is fed on top of it.

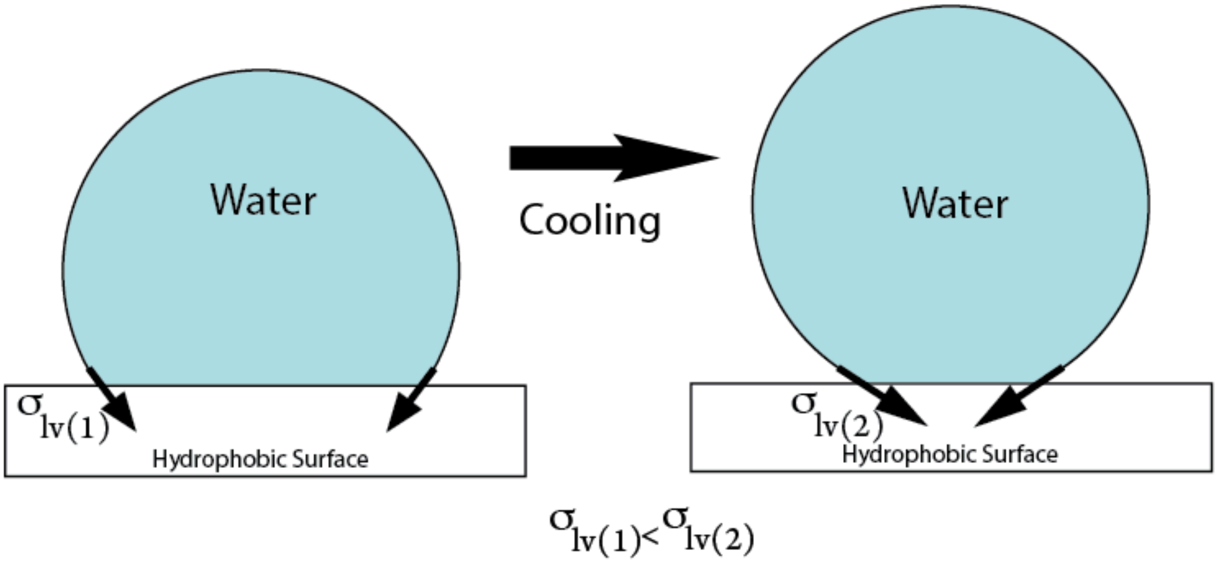

Figure 7.1: Predicted dynamics of a water drop on cooling hydrophobic substrates. The direction of the force is the same as the interfacial tension gradient, pointing toward the lower temperature substrate.

The present study aims to further elucidate the drop's spreading inception caused by cold hydrophobic substrates and unveil the underlying mechanism. The cold-induced spreading of water drops on hydrophobic surfaces is investigated and effects of the substrate temperature, humidity, types of hydrophobic surfaces, drop volume and surface roughnesses on the spreading are explored. The solid-liquid-gas line (trijunction) during the spreading is monitored closely using a high–speed camera. To our knowledge, no previous study has been published, which reports temporal evolution of the water drops on cooling hydrophobic surfaces from RT (Room Temperature) to -20 °C, with the addition of some of the aforementioned parameters such as the relative humidity and the drop volume.

7.2 Experimental Setup and Materials

Experimental setup is elaborated in Chapter 2.2. Four different hydrophobic surfaces of WX2100^{TM}, Fluorothane^{TM}, Silicon pillars and Teflon, with equilibrium angles of 144°±1.8, 142°±1.5, 149°±1.3 and 108°±2.1 were used, respectively. The area fraction of the solid surface (ϕ_s) for silicon pillars is 0.26. ϕ_s is the area fraction of the solid surface in contact with water and can be calculated as the ratio of the total pillar-top surface area to the total projected surface area. Both WX2100^{TM} (aerosol coating) and Fluorothane^{TM} (solution coating) are applied to the surface of cover glasses. It is worth mentioning that thickness of applied WX2100^{TM} spray and applied Fluorothane^{TM} solution on the cover glasses do not change the wetting characteristics substantially. The hydrophobic surfaces and their relevant properties are listed in table 5.

Table 5: Summary of parameters for hydrophobic surfaces used in Chapter 5. ϕ_s is the area fraction of the solid surface in contact with water. Contact angle measurements are performed on the water drops to up to six different locations on the substrate.

Hydrophobic Surfaces	Specifics and Application Method	Equilibrium Contact Angle (°)
WX2100^{TM}	Spray on cover glass	144±1.8
Fluorothane^{TM}	Dip coating of cover glass	142±1.9
Silicon Pillars	$\phi_s = 0.26$	149±1.3
Teflon	N/A	108±2.1

As we are dealing with temporal evolution of water drops on a cooling Peltier target, the temperature readings of the Peltier element during the cooling stage is crucial. Figure 7.2 shows the temperature of the Peltier element versus time for different cooling ranges of 24 °C to 10 °C, -10 °C, and -20 °C. For temperatures down to -10 °C, cooling rate can be considered to be constant. Cooling rate of the Peltier element from 24 to -10 °C yields to roughly 0.19 centigrades per seconds; however reaching lower temperatures of -20 °C, cooling rate deviates from linearity and decreases in time. No tangible fluctuations of temperature are observed after reaching the assigned temperatures. Temperature measurements of the Peltier surface using k-type thermocouple showed +0.2 °C higher values than the Peltier readings itself.

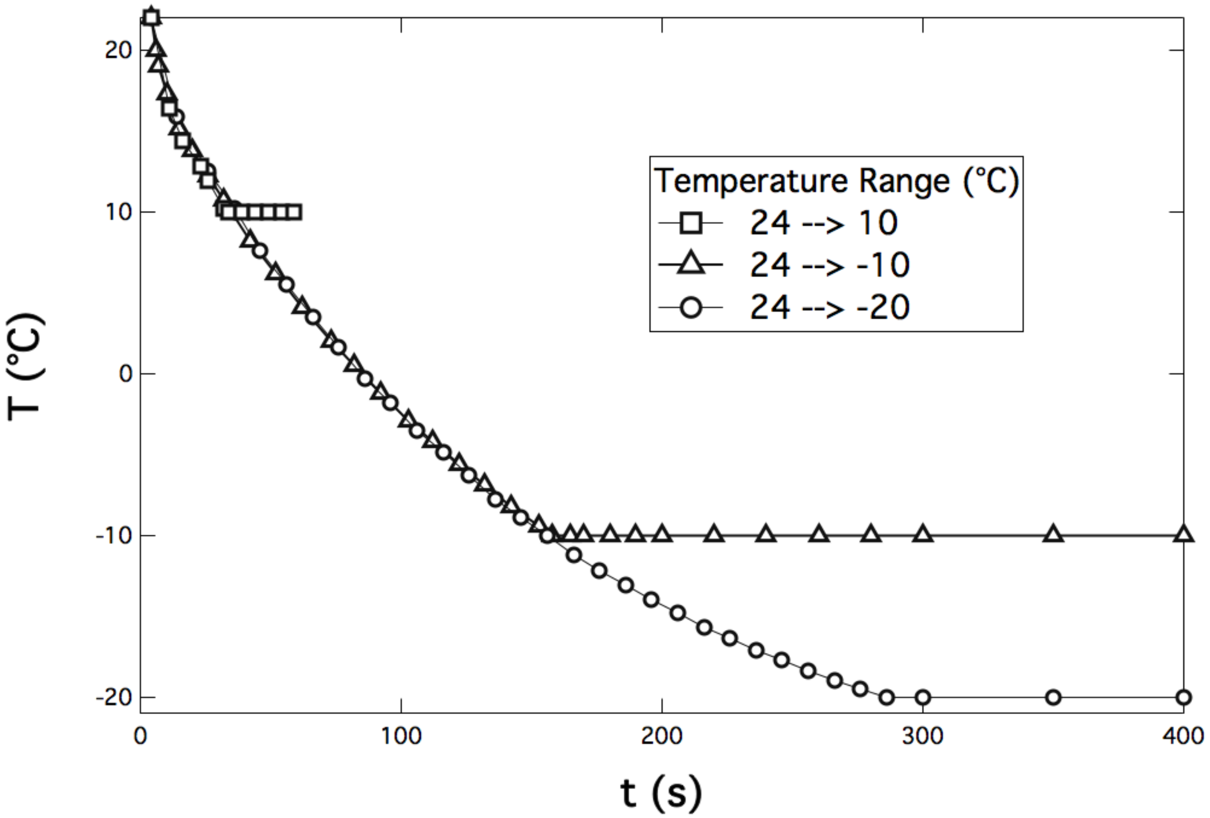

Figure 7.2: Temperature of the Peltier element situated in the DSA100 machine versus time during cooling processes.

7.3 Experimental Approach and Results

The preliminary results showed dependence of the drop dynamics on cooling hydrophobic substrates. In order to evaluate the physical parameters involved, we seek to vary a parameter at a time while isolating other possible affecting variables. To further probe the process, the cold-induced spreading of water drops on hydrophobic surfaces is systematically investigated and effects of the substrate's temperature, the relative humidity, cooling mode, surface hydrophobicity, the drop volume, and the substrate's roughness on the spreading are explored.

7.3.1 Effect of Cooling Mode on Cold-induced Spreading

We present two distinct modes of cooling procedures: i) water drops of 9 μL at room temperature are deposited on four different hydrophobic surfaces (Teflon, WX2100, Fluorothane and silicon pillars). Afterwards, solid substrates and a water drop simultaneously are cooled to -10 °C by a Peltier element situated underneath the WX2100 coated surface; ii) water drops of 9 μL volume are deposited on an already cold (-10 °C) hydrophobic surfaces. Figures 7.3 and 7.4 show the apparent contact angle and base diameter of the water drops versus cooling time, respectively. Open markers represent water drops which are deposited on 25 °C hydrophobic substrates and then both were cooled to -10 °C by the Peltier element (mode i). Closed markers represent water drops that were deposited on an already cold (-10 °C) hydrophobic substrate (mode ii). Clearly, water drops on a more hydrophobic surface attains smaller footprint and larger contact angle at initial conditions. Both modes of cooling resulted in same post-spreading diameter and contact angle, however at different timescales. For simultaneous cooling of drop and the substrate, final form of the drops is reached at longer times as compared to the other mode of cooling. The drop depinning followed by spreading occurred at both right and left contact angles, rather than rolling in one direction. The only exception is for water drops on Teflon that remains immobile and rests at 108° for equilibrium contact angle.

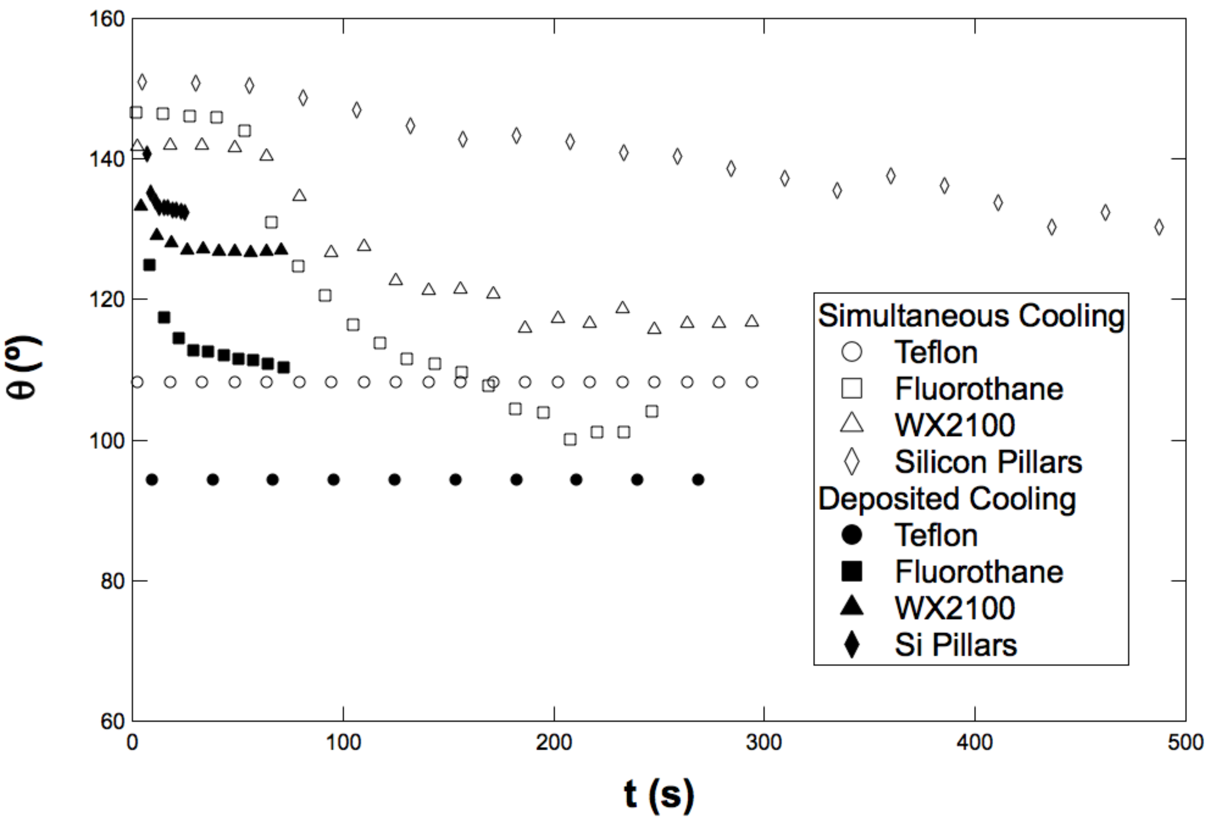

Figure 7.3: Apparent contact angle of water drops versus time for different hydrophobic surfaces (Fluorothane, Teflon, WX2100 and silicon pillars) and cooling modes. Open markers represent the water drops that were deposited on 25 °C hydrophobic substrates and then both were cooled to -10 °C by the Peltier element. Closed markers represent the 25 °C water drops that were deposited on a cold (-10 °C) hydrophobic substrate.

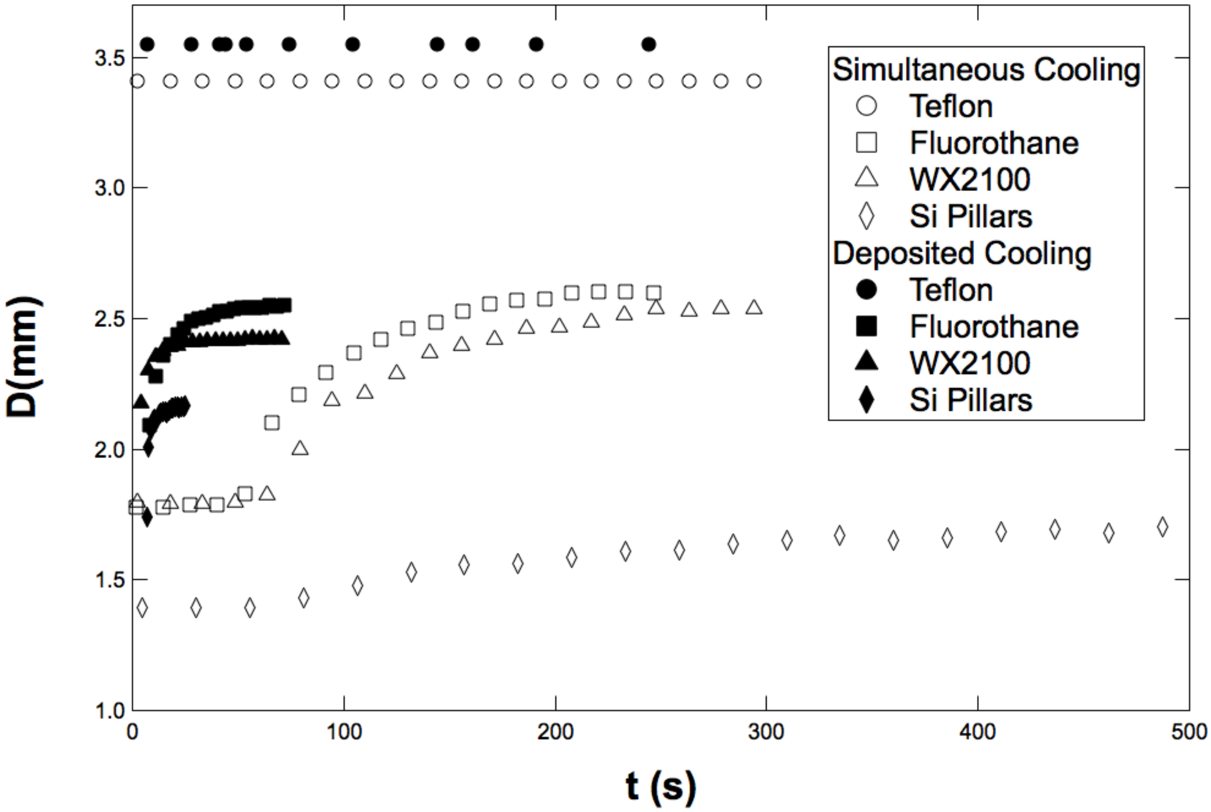

Figure 7.4: Apparent base diameter of water drops versus time for different hydrophobic surfaces and cooling modes. Open markers represent water drops which were deposited on 25 °C hydrophobic substrates and then both were cooled to -10 °C by the peltier element. Closed markers represent water drops that were deposited on a cold (-10 °C) hydrophobic substrate.

7.3.2 Temperature Dependence of Cold-induced Spreading

WX2100 coated surface and a water drop simultaneously were cooled by a Peltier element to assigned temperatures of 15 °C, 10 °C, 0 °C, -10 °C and -20 °C at constant relative humidity. During the cooling cycles, water drops started spreading smoothly over the solid substrate and stopped after a definitive amount of time. Figure 7.5 shows an example of these experiments in which a water drop with volume of 9 µL is cooled on WX2100 coated cover glass from RT to -10 °C. Depinning of the drops followed by spreading occurred at both right and left contact angles, rather than rolling in an arbitrary direction. The diameter of the injection needle, shown in Figure 7.5.a, is 0.51 mm. The initial drop diameter (7.5.a) and post-spreading drop diameter (7.5.g) are 1.78 mm and 2.44 mm, respectively. Figures 7.6 and 7.7 show contact angle and base diameter evolution for a single water drop on WX2100 hydrophobic surface cooled to different temperatures from RT. The post-spreading diameter and apparent contact angle of the drop are proportional to substrate's temperature, however drop geometry did not change when the drops were cooled to 15 °C. The measurements, especially contact angle, are noisier at lower temperatures due to substantial condensation and frosting at the trijunction. Time to spreading initiation is fairly independent from the assigned temperature; however, colder substrates caused higher spreading rates. All of the cold-enhanced spreading experiments are irreversible, i.e. the water drops do not recede when the temperature of the substrate is raised to RT.

In addition to water, ethylene glycol drops are deposited on WX2100 surfaces (θ_0 = 135°) and cooled to subzero temperatures to observe any change in the drop geometry. Thin liquid film and subsequent spreading of the drops have not transpired which leads to the fact that the condensation and the drop dynamics thereafter at the trijunction is not mainly controlled directly from the vapor phase surrounding the drop, but via the water liquid itself.

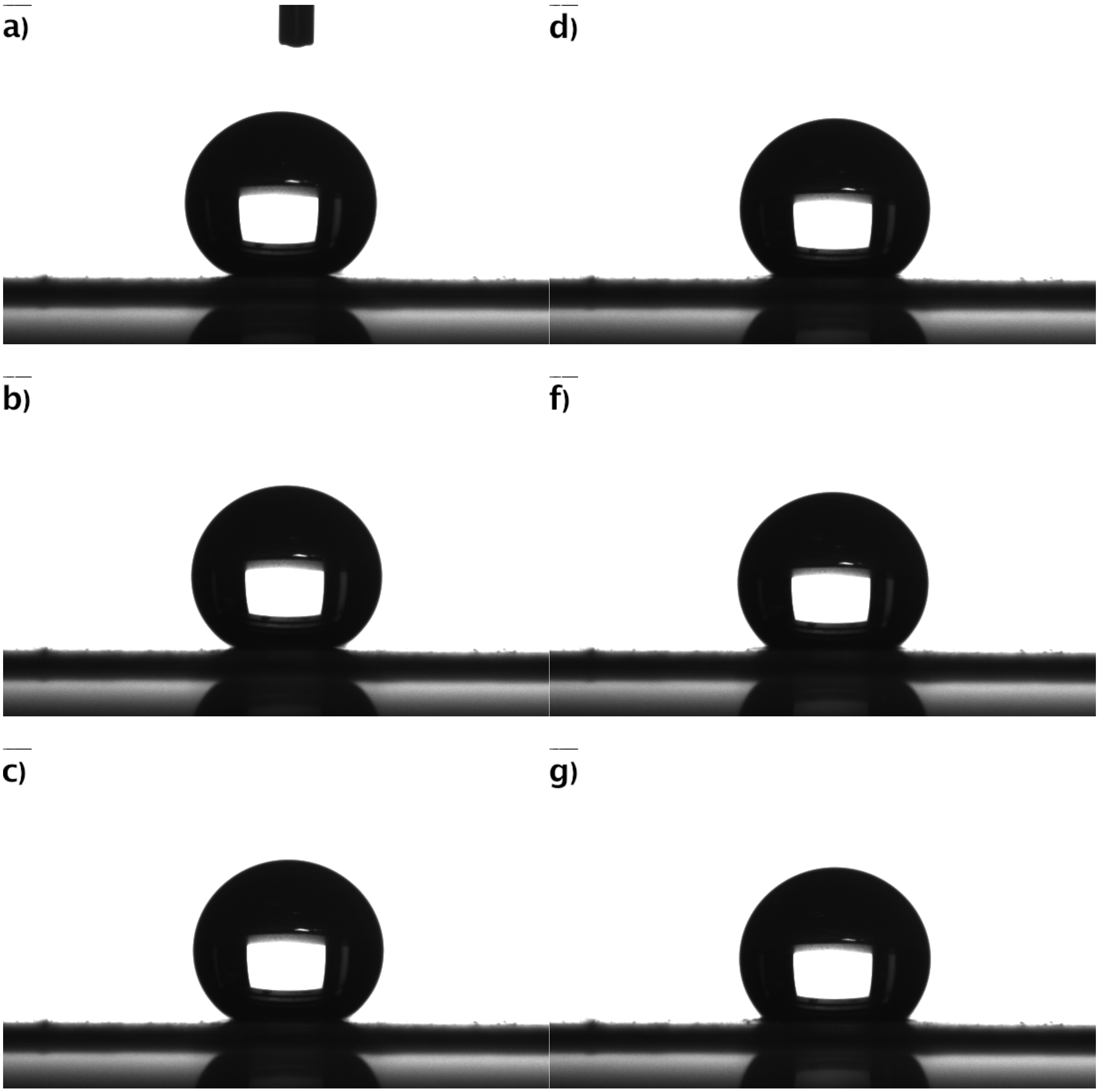

Figure 7.5: Cold-induced spreading of a water drop sequence (a-g) on WX2100 while the substrate is cooled from 25 °C to -10 °C. The depinning of the drop followed by spreading occurred simultaneously at both right and left contact angles, rather than rolling in one direction.

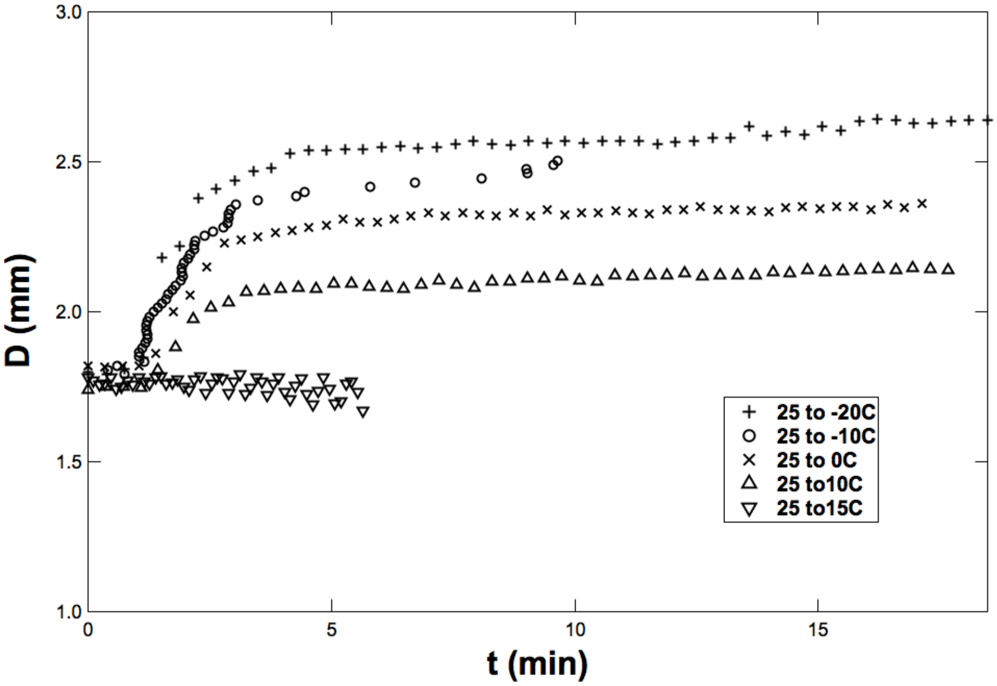

Figure 7.6: Drop base diameter versus time on WX2100 coated cover glass. Water drops were cooled down by the Peltier element to temperatures of 15 °C, 10 °C, 0 °C, -10 °C and -20 °C.

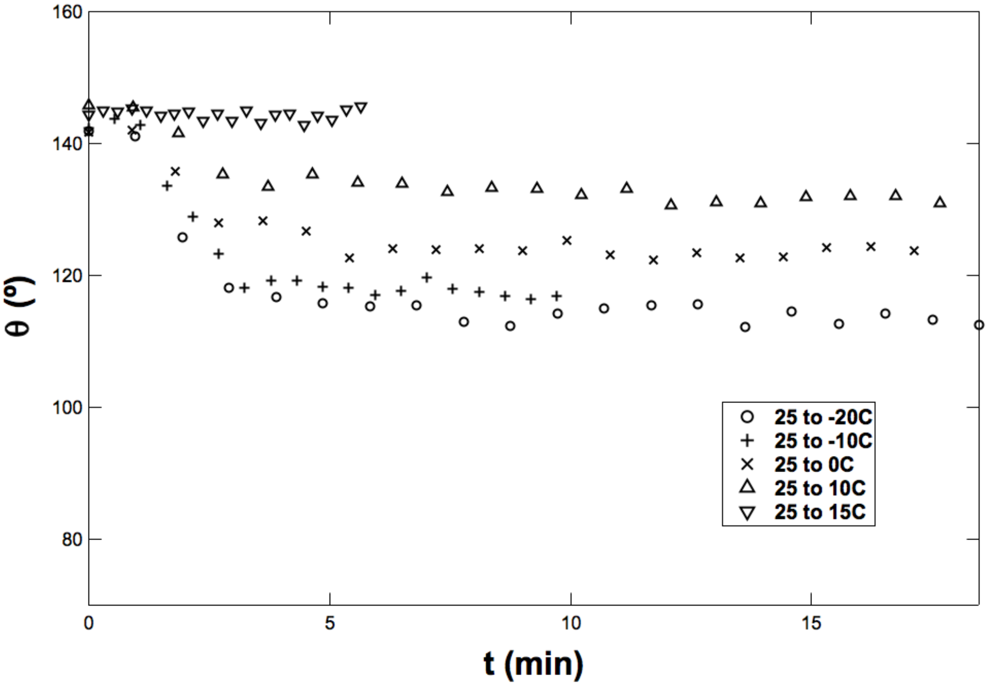

Figure 7.7: Drop contact angle versus time on WX2100 coated substrate. Water drops were cooled down by the Peltier element to temperatures of 15 °C, 10 °C, 0 °C, -10 °C and -20 °C.

7.3.3 Effect of Humidity on Cold-induced Spreading

Relative humidity is defined as the ratio of the partial pressure of water vapor to the saturated vapor pressure of water at any given temperature. Humidity, in general, may have two distinct effects in spreading of the water drops on solid targets: i) condensation on the solid surface which may render the solid substrate prewetted facilitating further spreading; and ii) determining the rate of evaporation, especially at the contact line region, which may induce gradients of surface tension. Lelah and Marmur [150] demonstrated that the rate of spreading of water on glass increased with an increase in the relative humidity.

Here, for a constant change in substrate temperature, from RT to -10 °C, humidity was adjusted using a nitrogen inflow into the DSA100 chamber. Water drops with volume of 9 µl are deposited on a Peltier element at RT. Then, predetermined humidity is reached through the chamber by adjustment of the nitrogen gas followed by the cooling cycle. Drop diameters did not change during humidity adjustment phase, prior to the cooling cycles. Figure 7.8 demonstrates the water drop on the hydrophobic surfaces at different atmospheric humidity levels from 6.5% to 47% during the cooling cycle of 25 °C to -10 °C at $t = 200$ s. Frost formation is mostly evident at 18% and 48% on the solid substrate. For relative humidity of 48%, excessive condensation forms thin liquid film on the hydrophobic substrate and discrete drops are evident on the substrate.

Figures 7.9 and 7.10 illustrate the dynamic contact angle and base diameter for single water drops on WX2100 hydrophobic surface at varying humidities during cooling stage from RT to -10 °C. Humidity effect turned out to be significant in changing drop-spreading dynamics. Higher relative humidity facilitated the spreading onset and increased the final diameter of the water drop especially on WX2100 surface (Figure 7.11). Figure 7.11 is a subplot of the figure 7.10 to clearly depict the effect of humidity. For relative humidities of 6.5%, 18% and 47%, the drops foot-print become 16, 31 and 40% larger after the spreading, respectively. Initial drop diameter drastically increased at 48% humidity for silicon pillars due to extreme condensation that renders the substrate prewetted.

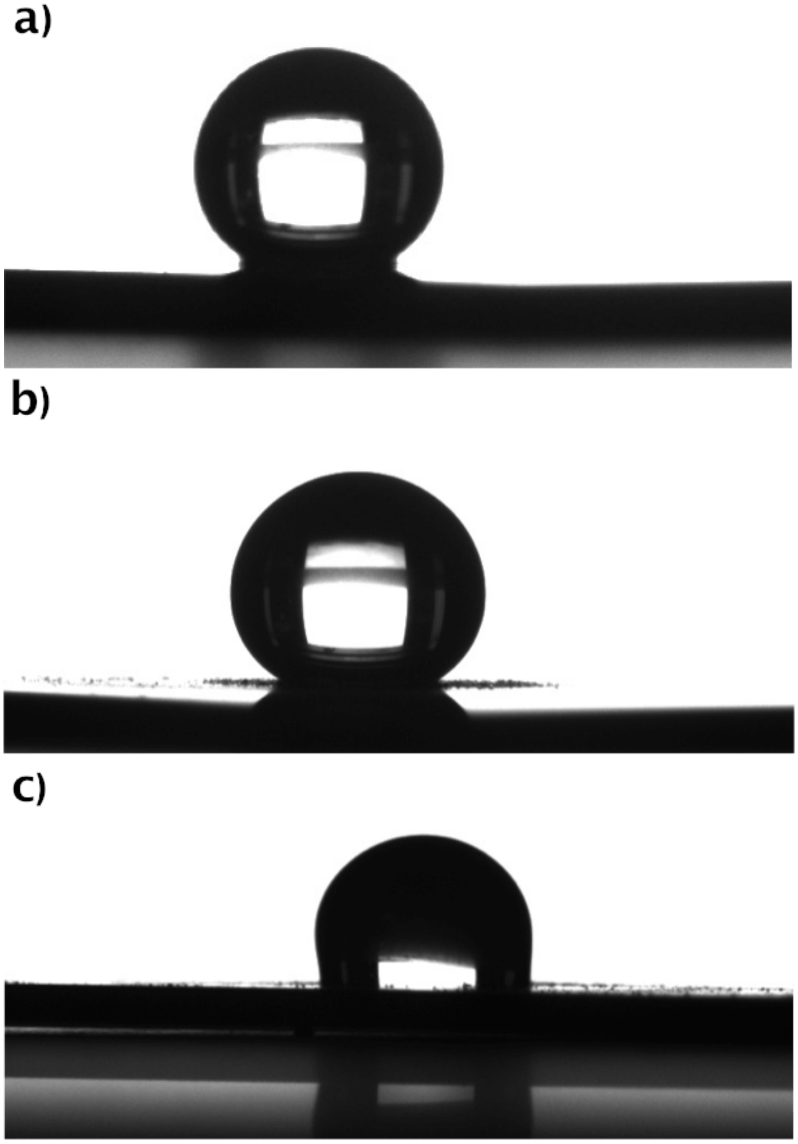

Figure 7.8: Water drops with volume of 9 μL on silicon pillars with atmospheric humidities of a) 6 RH%, b) 18 RH%, and c) 48 RH%. At high values of humidity, thin liquid film is formed on the silicon substrate.

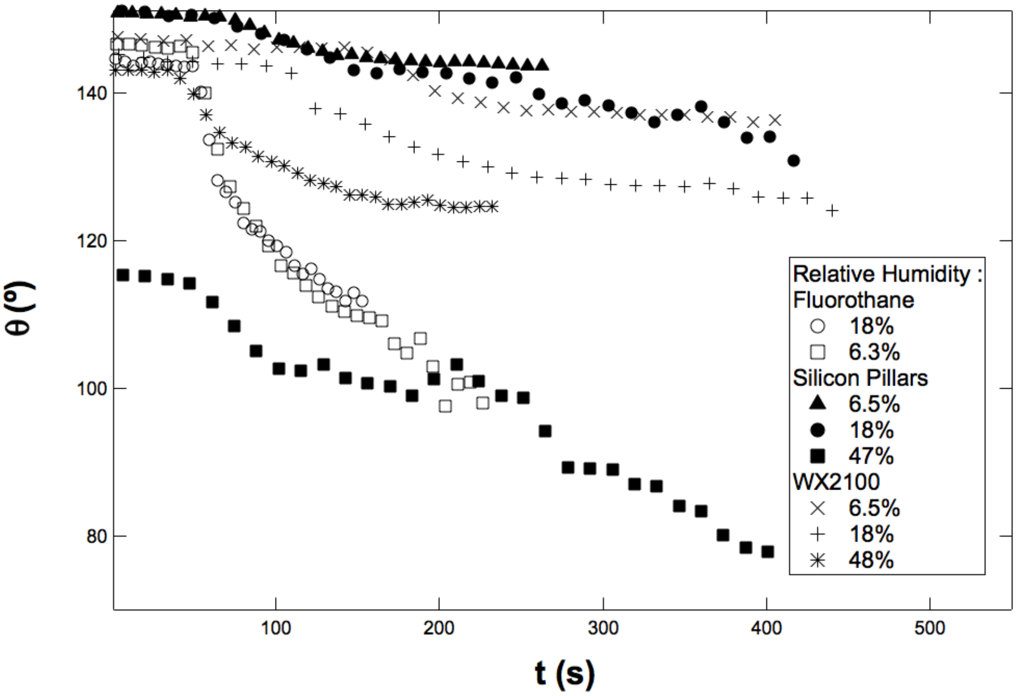

Figure 7.9: Contact angle of water drops with volume of 9 μL versus time of spreading drops cooled to -10 °C with varying relative humidities.

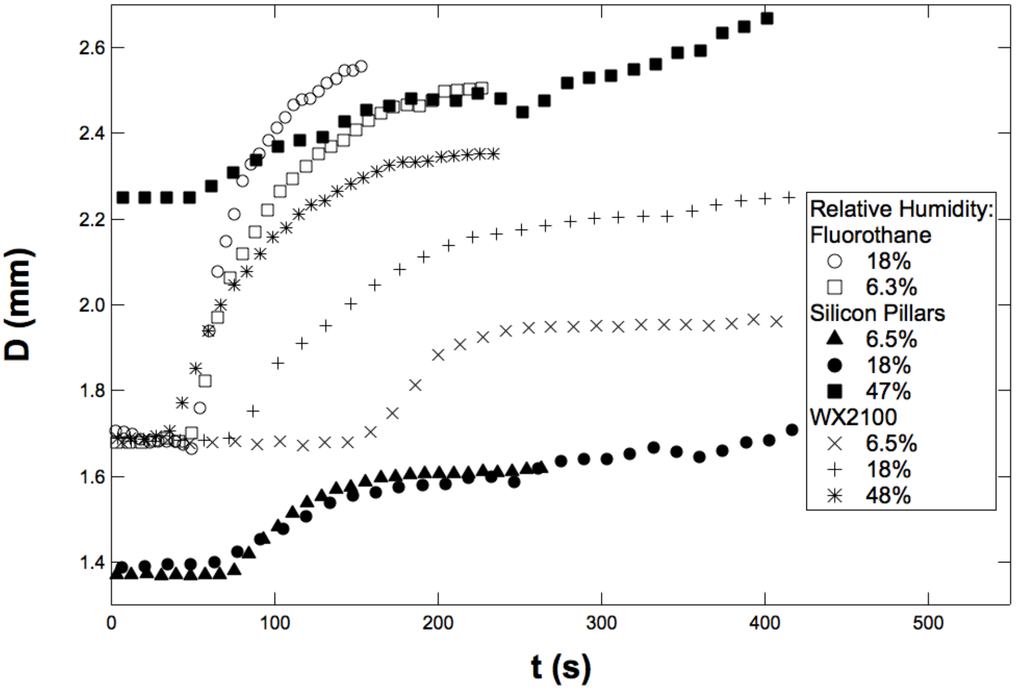

Figure 7.10: Base diameter versus time of spreading drops cooled to -10 °C with different relative humidities for multiple hydrophobic surfaces.

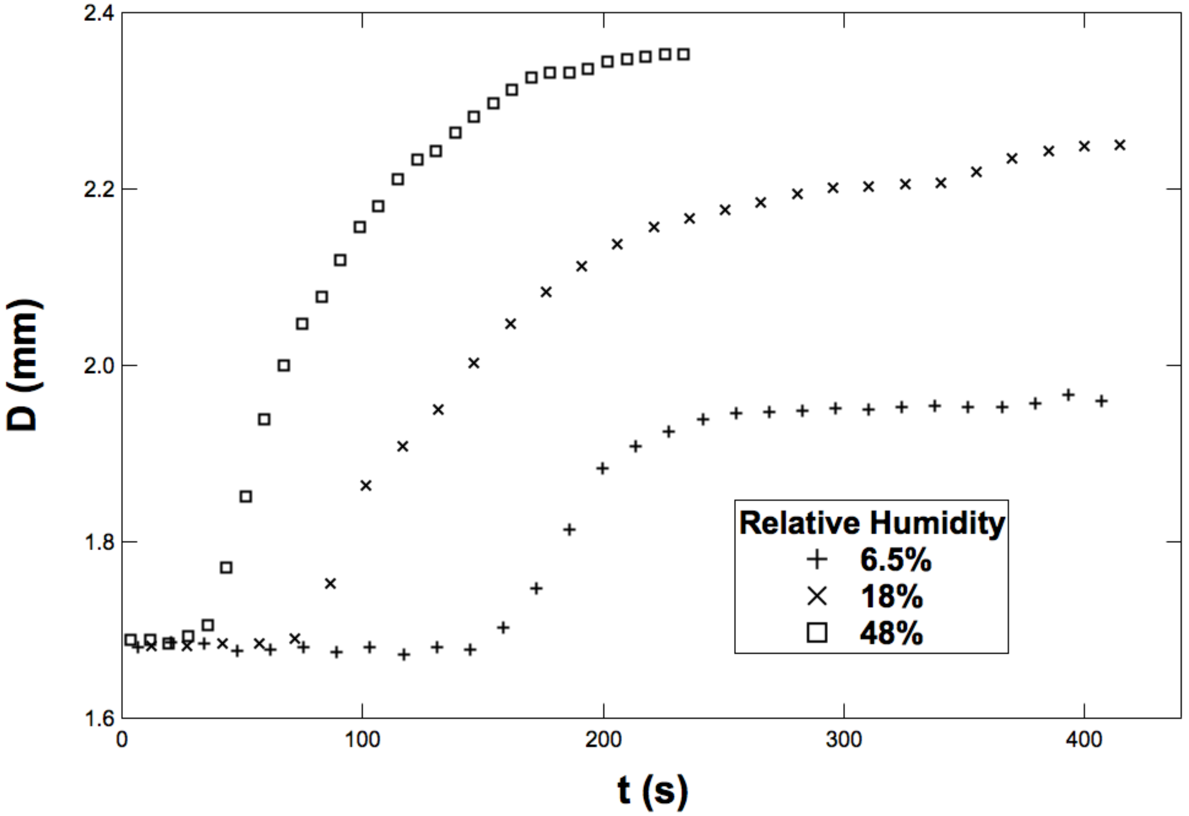

Figure 7.11: Base diameter versus time of water drops cooled to -10 °C on WX2100 surface with relative humidities of 6.5%, 18%, and 48%.

7.3.4 Effect of Roughness on Cold-induced Spreading

To analyze the effect of roughness, a simple and inexpensive method to fabricate hydrophobic surfaces, introduced by Nilsson et al. [151] is followed. In this method, Teflon surfaces are sanded using different grit designations and subsequent cleaning of solid Teflon surfaces. Each Teflon surface is held stationary and sanded by hand for at 20 s. After each sanding, samples were cleaned thoroughly in acetone, methanol and deionized water. After drying the substrates by the air gun, the sanded Teflon samples were heated to 80 °C to remove remaining moist from the roughened Teflon surfaces. A range of commercial sandpaper grit designations between 120-grit to 2000-grit is used to introduce roughness to smooth Teflon surfaces. Grit sizes correspond to the size of the particles and distance of the abrading particles embedded on the sandpaper. The higher the grit number the smoother the sandpaper, and the smaller the grit number the rougher the sandpaper. It is worth mentioning that the final hydrophobic properties were not dependent on additional sanding, in terms of both force and direction.

Constant volume of drops is deposited on a Peltier element situated in the DSA100 machine. The water drops are cooled to -10 °C. Figure 7.12 shows the dimensionless diameter of the spread water drops, ratio of the post-spreading drop diameter $\left(D_f\right)$ to the initial diameter $\left(D_0\right)$, versus grit size. Higher static contact angle for rougher surfaces is caused by decrease in contact angle hysteresis. Six data points are collected for each designated sanded Teflon. A larger standard deviation of static contact angles values is observed for rougher surfaces. Motion of water drops on rougher surfaces is more jerky which accounts for higher data scatter in the data. Static contact angles of the water drops on the 2000-grit sanded Teflon is the same as the Teflon itself, meaning that extremely fine roughness does not impart extra hydrophobicity to the Teflon surfaces. Water drops deposited on a 1000-grit and 2000-grit sanded Teflons do not spread during the cooling cycle; nonetheless, the static contact angle for 1000-grit sanded Teflon is roughly 10 degrees larger than the smooth and 2000-grit sanded Teflons. Ratio of post-spreading diameter versus initial diameter of the water drops increases with the surface roughness reaching ratios as high as 1.25 for 220-grit sanded Teflon, except for 120-grit size. The trend reversal from 600 to 120-grit size is attributed to extra coarse structure that acts as a resisting force to initiation of the spreading.

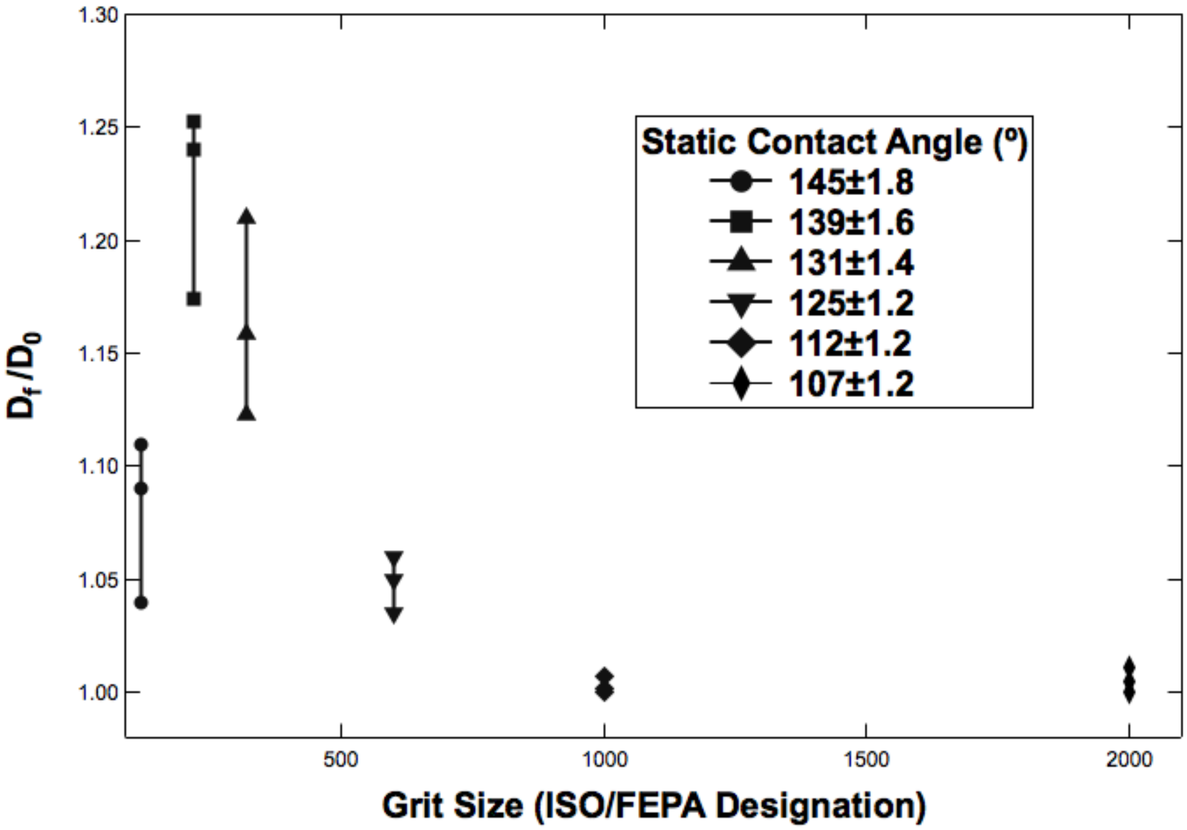

Figure 7.12: Dimensionless diameter of the water drops, ratio of post-spreading diameter (D_f) to initial diameter (D_0), versus grit size. Six data points are collected for each sanded surface.

7.3.5 Effect of Drop Size on Cold-induced Spreading

Different volumes of water drops are deposited on the WX2100 coated surface and cooled to -10°C using a Peltier element. The volume of the drops is measured using Tangent method 1 which is elaborated in Chapter 2.3. The initial contact angle of all the drops with specific volume is nearly the same with 2.4% standard deviation. The water drop diameter ranges from 0.47 mm to 11.22 mm. Figure 7.13 shows the water drop diameter on the cooling WX2100 coated cover glass surface versus time. Each curve represents the average of 3 experiments at assigned drop volumes shown. Data acquisition rate for all of the experiments is 2 Hz, however, for better distinction between data sets, intermittent data points are selectively removed and is illustrated in Figure 7.13.

Table 6 lists the volume of the drops and their associated elapsed time to depinning. Time to spreading initiation for relatively medium or big sized drops is approximately the same. At constant humidity and cooling temperature, the spreading kinetics and initiation at macroscale is only a function of contact angle, however, for water drops smaller than the capillary length, where the capillary length is $L_{cap} = \sqrt{\sigma / \rho g}$ and g is the gravitational acceleration, elapsed time to the drop depinnig increases, because surface forces become more dominant at these length scales. Even, for smaller drops in micrometer range, the van der Waals forces may become controlling. For deionized water, capillary length is 2.7mm. Both water drops with base diameters of 0.48 and 1.14mm showed longer times to depinning with respect to drops larger than capillary length. The importance of pinning effect for spreading small drops is experimentally verified by Perez et al. [152]. Independency of time to depinnig for water drops with respect to various sizes with the same contact angle, except for water drops smaller than capillary number at which capillary and VdW are important, signifies the impact of surface forces such as capillary condensation around the confined region rather than bulk forces depending on the drop volume.

Table 6: Elapsed time to depinning of water drops on WX2100 coated surface for different drop volumes.

Drop Volume (μL)	Drop Diameter (mm)	ETime to depinning (s)
0.4	0.47	126.7±4.5
4.1	1.12	67.6±4.2
39	3.13	37.5±3.3
66.9	3.90	32.05±3.4
180.8	6.556	42.57±2.1
556	11.22	36.3±2.8

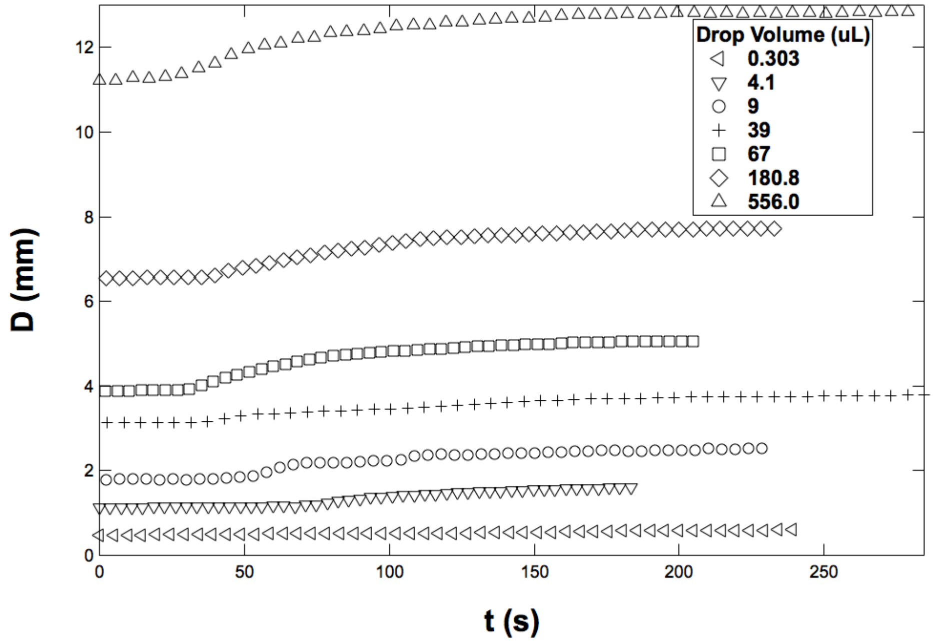

Figure 7.13: Apparent base diameter of the water drops on cooling WX2100 coated surfaces versus time for different drop volumes. The WX2100 coated cover glass is cooled from 25°C to -10°C by a Peltier element.

7.3.6 Qualitative Effect of Contact Angle on Cold-induced Spreading

It is already shown in Chapter 7.3.4 that the initial contact angle of the drop partially dictates the cold-induced dynamics of water drops. However, the adjustment of the initial contact angle in Chapter 7.3.4 is induced by roughness. In order to disentangle the influence of other parameters and solely evaluate the effect of initial contact angle, we deposited single water drops on WX2100 coated surface and decided to impart an uneven distortion to the drops using the 0.5mm injection needle. The injection needle is simply pushing down the left side of the drop. This distortion causes the drop to attain non-equal right and left contact angles (Figure 7.14.a).

Figure 7.15 shows the contact angles of both right and left contact points during the cold-induced spreading. Both contact angles decrease during the cold-induced spreading. Difference between right and left contact angles at initial condition is 17.9°, whereas preferred spreading diminishes this difference leading to 7.8° at final diameter. Figure 7.16 shows the relative right and left contact points movement in time for the experiment shown in Figure 7.14. During cooling of the substrate form 25 °C to -10 °C, the drop depins from the larger contact angle, in this case left contact angle, and start spreading. The left contact point is displaced 0.8 mm while trivial movement is observed at the right contact point. The preferred motion from the larger contact angle of the drop confirms the paramount effect of initial contact angle on cold-induced dynamics. Moreover, this means that the premature condensation and liquid film formation around the larger contact angle precedes the smaller one and confirms the effect of convexity of the trijunction on the enhanced condensation.

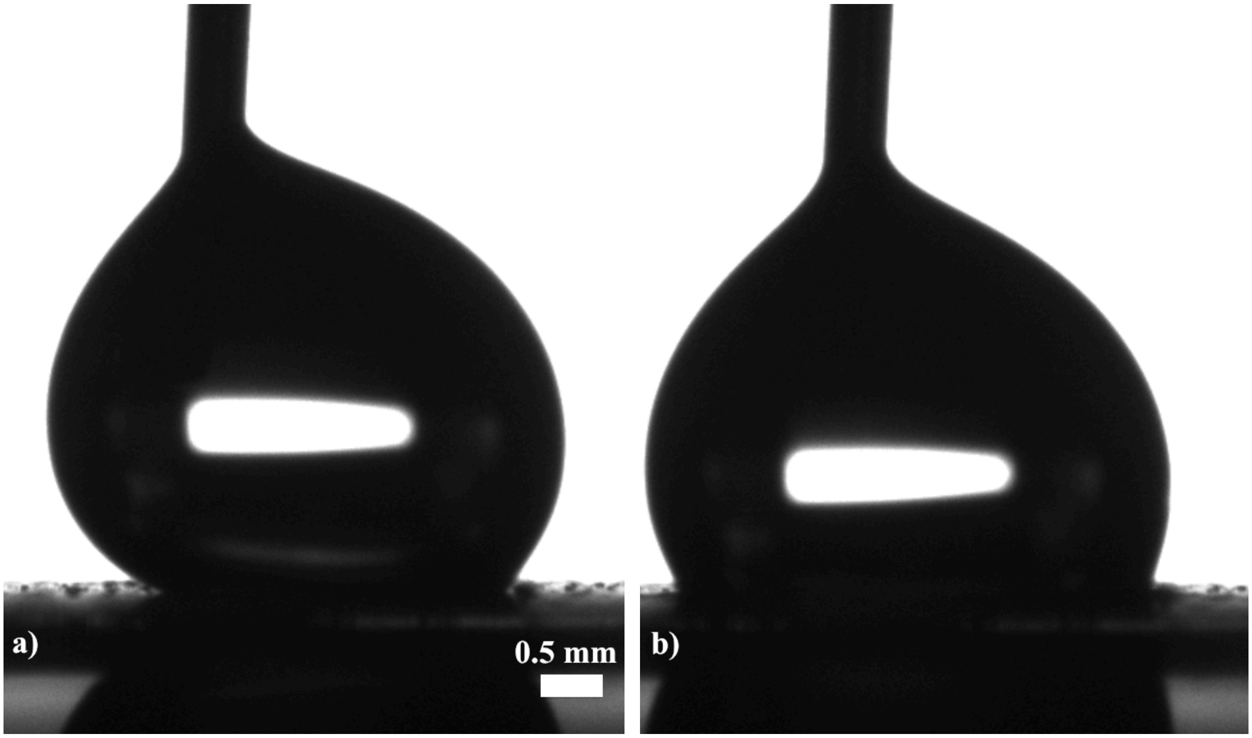

Figure 7.14: Cold-induced spreading of non-axisymmetric water drop, contorted by the injection needle cooled from RT to -10 °C. Depinning initiated from the larger, in this case left, contact angle with a minute movement at the right contact angle. Inset a) shows the drop prior to cooling initiation whereas inset b) depicts the drop after spreading completion.

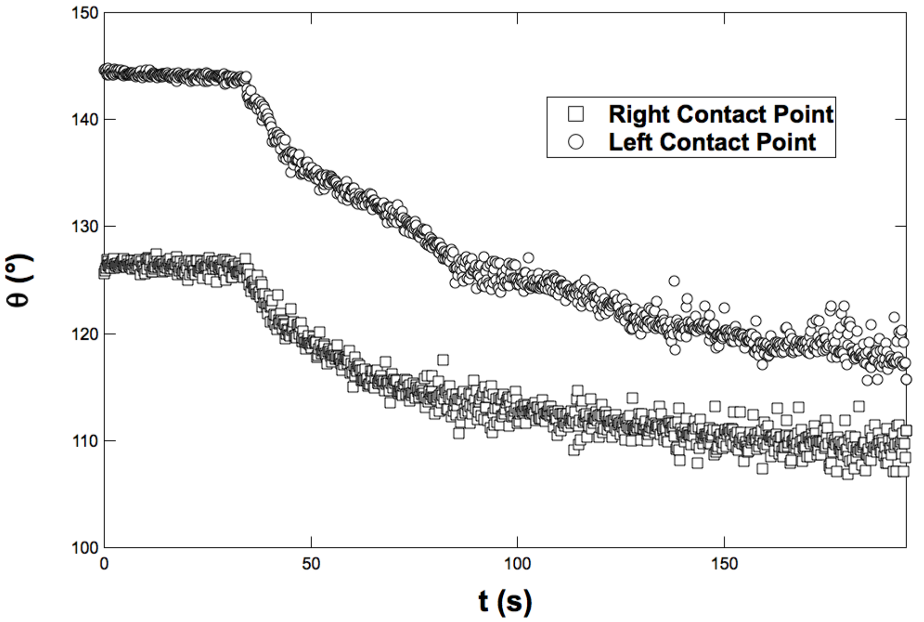

Figure 7.15: Contact angle measurements of right and left contact points during cold-induced spreading of the water drop shown in Figure 7.14 .

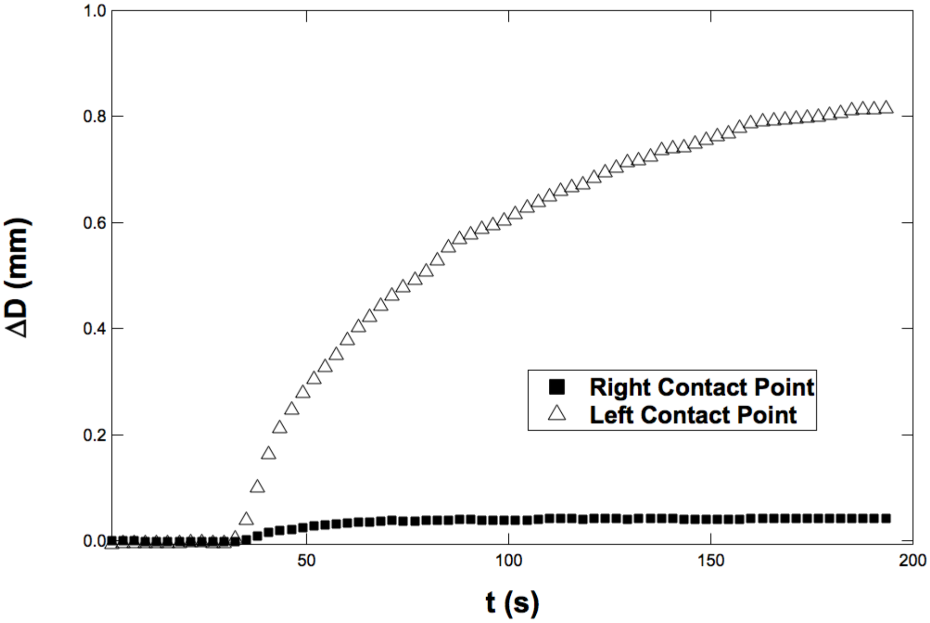

Figure 7.16: Relative right and left contact point movements with respect to time for the experiment in Figure 7.14. *ΔD* is the dynamic base diameter change with respect to the initial position of the contact points.

7.4 Discussion

In our study, cold-induced spreading of water drops on hydrophobic surfaces showed strong dependence on many factors such as the temperature, relative humidity, convexity of the trijunction region, roughness and drop volume. From the physical parameters studied and visually monitoring the trijunction region during spreading, the spreading inception is due to capillary condensation, at early stages, and subsequently controlled by the formation of a liquid rim at the trijunction followed by the film propagation radially away from the drop. Capillary condensation is a ubiquitous phenomenon in nano and even micro-scale [153], involving confined regions. In capillary condensation, vapor condensation occurs below the equilibrium vapor pressure due to higher surface interactions, such as capillary and van der Waals forces, at confined areas. This means that in these constricted regions, condensation transpires at higher temperatures and lower humilities than equilibrium values. Confined regions in the context of capillary condensation are, not limited to, sharp cracks [154], mesoporous media [155,156] and contacts between surfaces [157]. Capillary condensation can be problematic in atomic force microscopy and MEMS fabrication[158], as unwanted stiction ensues and sabotages both measuring and fabrication operations. In addition, capillary condensation amplifies crack propagation in stress-corrosion mechanisms [154,159]. However, capillary condensation can be advantageous in liquid phase sintering of powders which causes bridging effect that accelerates the densification process of the final solid piece [160]. This bridging effect also imparts mechanical stability to newly formed nanoparticles as thin films [161]. From simulations of Dijkstra [162], even capillary freezing is reported following the complete wetting at confined regions.

In our case, trijunction adjacent between water drop and the hydrophobic solid substrate is considered to be confined, if equilibrium contact angle is higher than a threshold value. This value is definitely higher than the equilibrium contact angle of 108 as no spreading is observed for water drops on the Teflon substrate (Figure 7.4). At this region, vapor condensation transpires at higher temperatures and lower humidity values common for condensation. The condensation on the substrate near the trijunction, results in thin film and micro drop formation that ultimately merge with the main water drops leading to spreading initiation along the solid substrate. Some simulations [163,164] reported that confined fluid between a solid sphere and planar solid, in our case liquid water drop, is stable only in the form of concave meniscus. The concavity of the microscale meniscus at the trijunction renders the spreading water drops on hydrophobic surfaces favorable.

In order to better grasp the mechanism of the water drops spreading, we zoomed in at the trijunction region and recorded videos while the drop is being cooled to -10 °C (Figure 7.17). A thin liquid film, composed of tiny water drops, forms around the trijunction during the cooling process and propagates away from the drop. Through the process, the drop starts spreading on the thin liquid film and finally stops. After the water drop becomes immobile, the micro drops around the trijunction becomes larger, with no apparent movement in the water drop. Figure 7.18 qualitatively illustrates the dynamics involving the cold-induced spreading. In the illustration, the condensation at the trijunction is originated from the air vapor phase and evaporation of liquid phase. After condensation at the trijunction and liquid film formation, the water drop depins and starts spreading on the hydrophobic substrate.

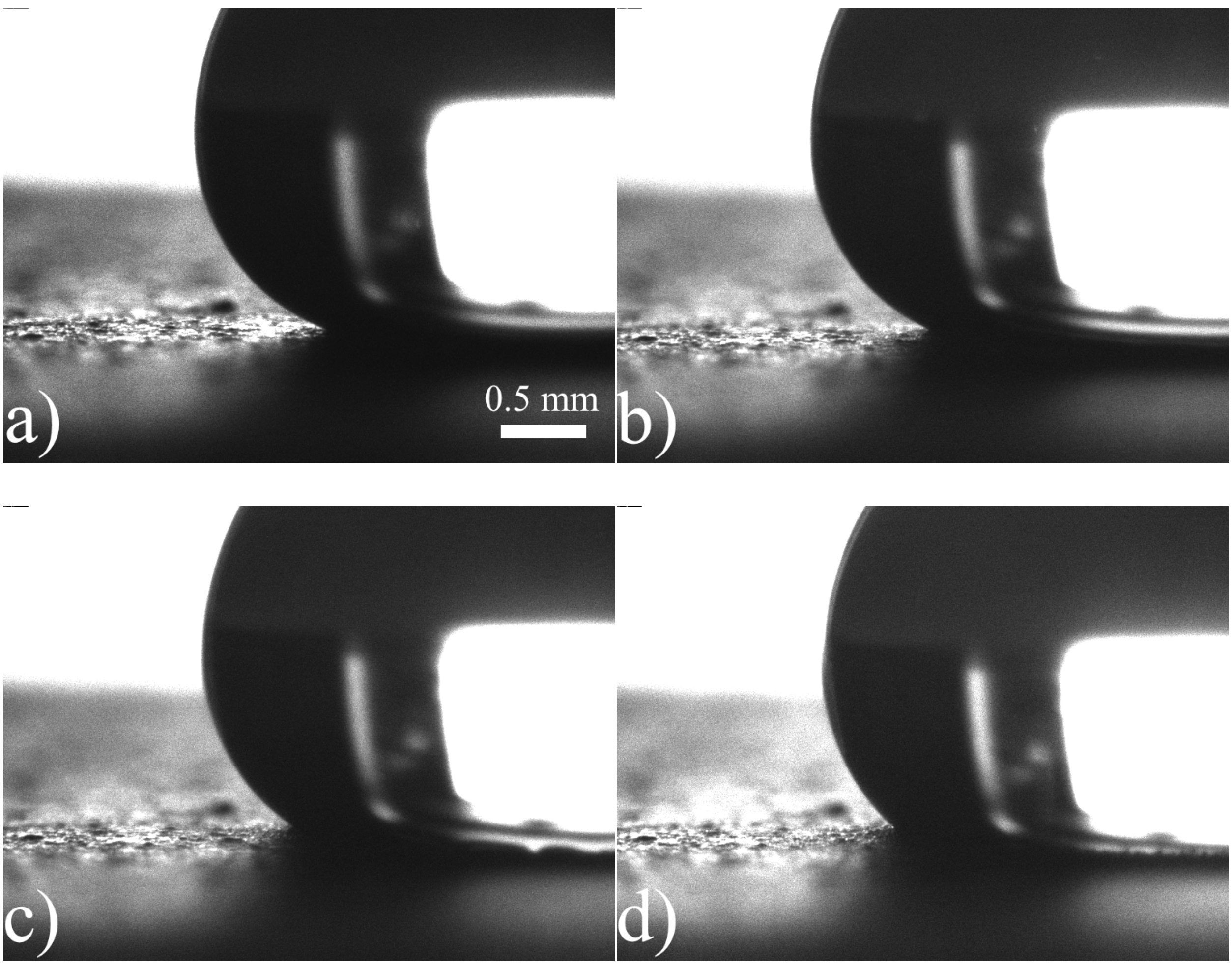

Figure 7.17: Sequence of a cold-induced water drop spreading (a-f) on a cooling WX2100 coated substrate. The premature condensation followed by the thin film formation and propagation at the trijunction initiates the drop spreading. The camera has been adjusted to +4 degrees above the horizon to clearly monitor the solid-liquid-gas region.

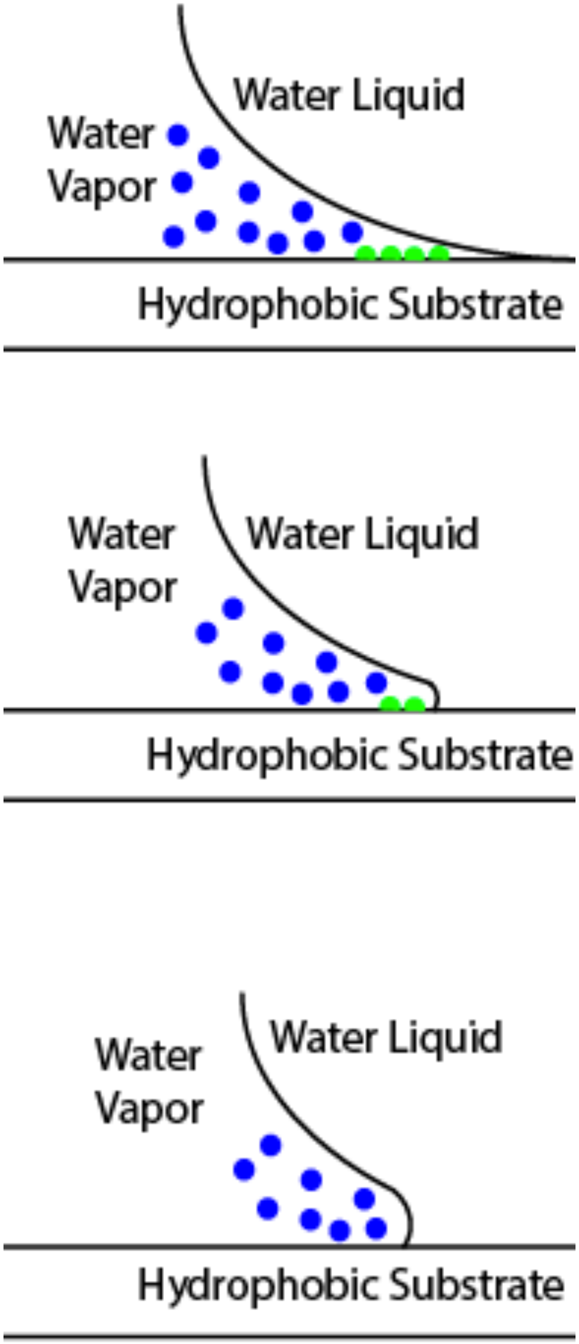

Figure 7.18: Qualitative illustration of the proposed explanation for the observed enhanced spreading of water drops on hydrophobic surfaces. The condensed drops on the substrate can be formed from the water vapor surrounding the trijunction or/and directly from the liquid phase.

7.5 Conclusions

To conclude, we study the temporal evolution of water drops on cooling hydrophobic substrates. Water drops are placed on hydrophobic surfaces using a needle coupled to a computer-controlled liquid-dispenser network, and goniometer optics and a computer with special software are used to measure the base diameter and contact angles of the drops. The water drops on cooling hydrophobic surfaces depin and start to spread (up to 33% of the initial diameter) on cooling hydrophobic surfaces. This cold-induced spreading is found to be strongly dependent on the substrate temperature, relative humidity of the surrounding air, and initial contact angle of the drop. From the physical parameters studied and visually monitoring the trijunction region during spreading, the spreading inception is due to capillary condensation, at early stages, and subsequently controlled by the formation of a liquid rim at the trijunction followed by the film propagation radially away from the drop. During the growth phase of the thin film, the drop depins and starts spreading gradually on the film.

Lower temperatures of the hydrophobic substrate resulted in more spreading of the drops, however, different designated temperatures have not affected the time to spreading initiation. Higher humidity of surrounding air facilitated the onset of spreading with larger final foot-print of the drops. To evaluate the effect of roughness, Teflon targets are roughened using different sizes of sandpapers. Rougher surfaces generate more hydrophobicity on the Teflon substrate. Introducing roughness to the hydrophobic surfaces lead to higher post-spreading diameter during cooling of the solid targets; however, extremely rough surface impedes cold-induced spreading due to higher friction imparted to the drop’s movement. Drops with smaller base diameter than capillary number of water showed more resistance to spreading initiation due to pinning effect stemmed from strong capillary and even vdW forces. In order to evaluate the sole dependence of cold-induced spreading on initial contact angle, the deposited water drop on a hydrophobic surface is distorted using a injection needle to alter the symmetry of the water drop. This contortion by the needle causes the drop to attain different angles at right and left. Spreading transpires at the contact point with larger contact angles confirming the paramount effect of initial contact angle on cold-induced dynamics.

These preliminary results present a new insight into the dynamic behavior of water drops on hydrophobic surfaces at cold conditions. This will be of great importance in the design, evaluate and development of superhydrophobic materials for freezing-delay and anti-icing applications such as maritime industry, aircrafts, antennas, wind turbines, high-voltage power lines, andanemometers.

CHAPTER 8

Conclusions

In this chapter, the main findings and significant conclusions of this thesis are presented and suggestions for future work are mentioned.

8.1 Summary of Results

Liquid spreading on cold solid substrates is ubiquitous in nature and industry. We study the dynamics of non–isothermal spreading of water liquids on cold solid substrates followed by phase change. We conducted experimental studies at different substrate's temperature and fluid flow rates. A few previous studies have not provided any theoretical justification for the observed empirical data primarily due to inaccurate freezing initiation mechanism and growth postulated. A novel hypothesis of the spreading solidifying drops on cold solid substrates is introduced that emphasizes on the origin of early stages of the drop solidification. . We assume that a drop stops spreading when the volume of solid formed at the trijunction, at which effectively infinite heat flux occurs, reaches a critical value, V_c. The heat flux singularity stems from the discontinuous boundary condition of the heat flux vector at the trijunction. The critical solidified volume of this region equals the circular sector bounded by the adjunct isotherm multiplied by the drop's circumference. Classical solidification model is used to relate the growth of the solidified layer to time. Development of this hypothesis followed by integrating with the governing equations of fluid dynamics and heat transfer leads to a formula, relating radius of the solidified drop to Stefan number. The theoretical formula derived comports with the experimental data observed. To further test our proposed hypothesis, we designed two sets of experiments, which will either strengthen or fully negate our presumed hypothesis. First, we performed impact experiments of hexadecane with low to medium Weber numbers on different substrates. In the second set of experiments, we deposited liquid drops on inclined aluminum target and explored the effects of substrate's temperature and inclination angle. By extending our hypothesis to both types of experiments, formulations from our hypothesis by scaling analysis confirm the experimental results. Unprecedently, this derived equation corroborates the experimental data of molten liquid solidification on cold substrates.

In chapter 5, freezing–delay property of hydrophobic surfaces, a current subject of debate in literature, is further explored under forced spreading conditions. We conducted experimental and numerical study of solidification delay on hydrophobic surfaces. In the experimental section, we performed forced spreading of water with different flow rates on cover glass with temperatures of -10°C and -20°C at constant humidity. The spreading rate of water drops on hydrophobic surfaces is slower due to high contact angle of these surfaces as compared to hydrophilic ones. At -10°C and small enough flow rates the freezing inception is postponed on the hydrophobic surfaces as compared to the hydrophilic cover glass. At higher flow rates, no solidification transpires on both surfaces as cooling temperature is not adequate to initiate heterogeneous nucleation and freezing of the drop. At lower temperature of the substrate and lower flow rates, water drops instantly freeze on both surfaces with larger footprint on hydrophilic surface; however, higher flow rates results in longer freezing time scales as compared to hydrophilic cover glass. Numerical analysis is conducted to assess the effect of contact angle on possible delay on freezing of static drops. Wedge-like representation for the water drop on cold solid substrate is postulated. Numerical studies unequivocally confirm that higher static contact angles postpone the solidification inception of the static water drops and the growth rate of the solidified layer is slower for the drops with higher contact angle. Hence, at constant time, the solidified layer ascended less along the drop's liquid-gas interface for hydrophobic surfaces.

In chapter 6, we study the intermittent freezing stage of static supercooled liquids by cold solid hydrophilic and hydrophobic substrates. Using a high-speed camera, we observe a well-known kinetics-driven stage (recalescence) prior to the main freezing stage. The front speed of this intermittent stage is in the range of 50-150 mm/s. This is also confirmed from the temperature measurements acquired by the k-thermocouple and the IR camera, at which cooled drops reached 0°C in less than 20ms and maintained that value until the main solidification interface fully covers the drop from the bottom plane to the top. In all of our 76 experiments, the nucleation fronts initiate from a point on the trijunction and propagate into the drop volume with different structural morphologies dictated by the temperatures and surface hydrophobicity of the substrate. The morphology of the recalescence front varies from planar to dendritic growth depending heavily on the substrate temperatures, whereas, on hydrophobic surfaces, the recalescence interface maintains a convex front. After completion of the main solidification, cooling of ice begins at relatively constant rate. Both the main solidification and ice cooling duration are highly dependent on drop size. However, no conclusive relationship can be made regarding the duration of the supercooling stage with the drop size and the surface hydrophobicity. Using an infrared camera, our main finding in this chapter is that the duration of the supercooling stage is controlled by the collective recalescence of condensed micro-drops surrounding the main drop that manifests itself in a wave-like "front" movement. This front seems fairly straight with some instability-induced bumps. The moment at which the recalescence wave reaches the main drop circumference, recalescence is triggered in the main drop.

In chapter 7, we systematically investigate the temperature–induced spreading of water drops on cooling hydrophobic surfaces that we observed during the experiments of previous chapters. We deposited water drops on different hydrophobic surfaces and cooled the hydrophobic surfaces using a Peltier element situated in the DSA100 machine. The water drops depin during the cooling stage and start to spread (up to 33% of the initial diameter). This cold-induced spreading is found to be strongly dependent on the substrate temperature, relative humidity, volume of the drops, and initial contact angle of the drop. From the physical parameters studied and visually monitoring the trijunction region during spreading, the spreading is believed to be from the capillary condensation and formation of a liquid rim at the trijunction followed by the film propagation radially away from the drop. During the growth phase of the thin film, the drop depins and starts spreading gradually on the film. Lower temperatures of the hydrophobic substrates resulted in increased spreading of the water drops, however different designated temperatures have not affected the elapsed time to spreading initiation. Higher relative humidity facilitated the onset of the spreading with larger post–spreading base diameter of the water drops. To evaluate the effect of roughness, Teflon targets are roughened using different sizes of sandpapers. Rougher surfaces generate more hydrophobicity on the Teflon substrates. Introducing roughness to the hydrophobic surfaces lead to higher post-spreading diameter during cooling of the solid targets; however, extremely rough surface impedes cold-induced spreading. Water drops with smaller base diameter than Capillary number of water showed more resistance to spreading inception due to the pinning effect stemmed from strong capillary and even VdW forces at microscale; however, for water drops larger than capillary number, elapsed time to depinng is independent from the drop base diameter.

The experimental results of Chapter 7 corroborate the influence of many parameters such as the relative humidity, surface roughness, initial contact angle and the drop volume on the cold-induced spreading of water drops on hydrophobic surfaces. It is hoped that our experimental results and provided explanation presented in Chapter 7 provide some insight into the cold-induced spreading of water on cooling hydrophobic surfaces and stimulate more studies on this subject.

8.2 Future Work

As mentioned by a few previous works on solidifying molten drops on solid targets, heat flux singularity needs a fundamental adjustment in continuum theory to get resolved. This is the main obstacle to solve the heat transfer equation in non-isothermal spreading with or without phase change, nonetheless, the molten contact line is unaware of this mathematical complication. A complete understanding of the problem could potentially be resolved through the physics at molecular scale. In addition, intrinsic nature of critical solidified volume (V_c) needs to be defined. High–speed visualization of the trijunction during solidification initiation would unravel the mystery.

The initiation mechanism and kinetics of recalescence front of the dropwise micro–condensates, which effectively dictates the freezing initiation of other water drops present, need to be understood. The effect of the condensates' sizes and distances from one another on the "front" speed needs to be investigated. A newly observed phenomenon of cold-induced spreading of water drops on hydrophobic surfaces requires more thorough experiments to test the different physical parameters especially on roughness-induced hydrophobic surfaces. The interplay and competition of both governing driving forces, condensation from the vapor or the liquid drop liquid itself, should be quantified and controlling regimes at different stages need to be determined.

Bibliography

[1] Vardelle M., Vardelle A., Leger A. C., Fauchais P., and Gobin D., "Influence of particle parameters at impact on splat formation and solidification in plasma spraying processes", *J. Therm. Spray Technol.*, **4** (1995) 50-58.

[2] Amon C. H., Schmaltz K. S., Merz R., and Prinz F. B., "Numerical and experimental investigation of interface bonding via substrate remelting of an impinging molten metal droplet", *J. Heat Transfer*, **118** (1996) 164-172.

[3] Gao F. Q. and Sonin A. A., "Precise deposition of molten microdrops - the physics of digital microfabrication", *Proc. R. Soc. London, Ser. A*, **444** (1994) 533-554.

[4] Kullmann C., Schirmer N. C., Lee M.-T., Ko S. H., Hotz N., Grigoropoulos C. P., and Poulikakos D., "3d micro-structures by piezoelectric inkjet printing of gold nanofluids", *Journal of Micromechanics and Microengineering*, **22** (2012) 1-11.

[5] Sirringhaus H., Kawase T., Friend R. H., Shimoda T., Inbasekaran M., Wu W., and Woo E. P., "High-resolution inkjet printing of all-polymer transistor circuits", *Science*, **290** (2000) 2123-2126.

[6] Waldvogel J. M. and Poulikakos D., "Solidification phenomena in picoliter size solder droplet deposition on a composite substrate", *Int. J. Heat Mass Transfer*, **40** (1997) 295-309.

[7] Griffiths R. W., "The dynamics of lava flows", *Annu. Rev. Fluid Mech.*, **32** (2000) 477-518.

[8] Hutter K., *Theoretical glaciology: Material science of ice and the mechanics of glaciers and ice sheets*. Theoretical glaciology. Material science of ice and the mechanics of glaciers and ice sheets, 1983: Springer.

[9] Meng-Jiy W., Fang-Hsing L., Jun Yan O., and Shi-Yow L., "Dynamic behaviors of droplet impact and spreading: Water on glass and paraffin", *Colloids Surf., A*, **339** (2009) 224-231.

[10] Xia Hong W. and Conrad H., "Effect of sn content of pb-sn solder alloys on wetting dynamics", *Scripta Metallurgica et Materialia*, **31** (1994) 375-380.

[11] Wang H. Q., Gao F., Ma X., and Qian Y. Y., "Reactive wetting of solders on cu and cu6sn5/cu3sn/cu substrates using wetting balance", *Scripta Materialia*, **55** (2006) 823-826.

[12] Cummins G. and Desmulliez M. P. Y., "Inkjet printing of conductive materials: A review", *Circuit World*, **38** (2012) 193-213.

[13] Fang M., Chandra S., and Park C. B., "Heat transfer during deposition of molten aluminum alloy droplets to build vertical columns", *Journal of Heat Transfer*, **31** (2009) 112101.

[14] Ghafouri-Azar R., Mostaghimi J., and Chandra S., "Numerical study of impact and solidificatin of a droplet over a deposited frozen splat", *International Journal of Computational Fluid Dynamics* **18** (2004) 133-138.

[15] Orme M. E. and Natl Sci F. D. N., *Microstructure refinement and net-form materials synthesis with controlled nano-liter droplet deposition*. Proceedings of the 1995 nsf design and manufacturing grantees conference, 1994, Dearborn: Soc Manufacturing Engineers. 467-468.

[16] Orme M. and Smith R. F., "Enhanced aluminum properties by means of precise droplet deposition", *Journal of Manufacturing Science and Engineering-Transactions of the Asme*, **122** (2000) 484-493.

[17] Chapuis J., Romero E., Soulie F., Bordreuil C., and Fras G., "Behaviour of spreading molten metal drops deposited by fusion", *Experimental Thermal and Fluid Science*, **48** (2013) 29-36.

[18] Lim Y. C., Farson D. F., Cho M. H., and Cho J. H., "Stationary gmaw-p weld metal deposit spreading", *Science and Technology of Welding and Joining*, **14** (2009) 626-635.

[19] Quintella M. A., *Numerical investigation of the heat flux singularity at an advancing molten contact line*, 1997, Massachusetts Institute of Technology. p. 105.

[20] Sanz A., Meseguer J., and Mayo L., "The influence of gravity on the solidification of a drop", *Journal of Crystal Growth*, **82** (1987) 81-88.

[21] Anderson D. M., Worster M. G., and Davis S. H., "The case for a dynamic contact angle in containerless solidification", *J. Cryst. Growth*, **163** (1996) 329-338.

[22] Satunkin G. A., Tatarchenko V. A., and Shaitanov V. I., "Determination of the growth angle from the shape of a crystal lateral face and solidified separation drops", *Journal of Crystal Growth*, **50** (1980) 133-139.

[23] Shukla P., Mandal R. K., and Ojha S. N., "Non-equilibrium solidification of undercooled droplets during atomization process", *Bulletin of Materials Science*, **24** (2001) 547-554.

[24] Wadley H. N. G., Queheillalt D. T., and Lu Y. C., *Laser ultrasonic sensing of solid-liquid interfaces during bridgman single crystal growth*. Sensors and modeling in materials processing: Techniques and applications, ed. S. Viswanathan, R.G. Reddy, and J.C. Malas, 1997, New York: Masson Int Nursing Publications. 279-293.

[25] Schiaffino S. and Sonin A. A., "Molten droplet deposition and solidification at low weber numbers", *Phys. Fluids*, **9** (1997) 3172-3187.

[26] Worthington A. M. *On the forms assumed by drops of liquids falling vertically on horizontal plate*. in *Proc. Royal Soc.* 1876. London.

[27] Oron A., Davis S. H., and Bankoff S. G., "Long-scale evolution of thin liquid films", *Reviews of Modern Physics*, **69** (1997) 931-980.

[28] Tanner L. H., "Spreading of silicone oil drops on horizontal surfaces", *J. Phys. D: Appl. Phys.*, **12** (1979) 1473-1484.

[29] Kistler S. F., *Hydrodynamics of wetting*, in *Wettability,*1993, Marcel Dekker: New York.

[30] Hoffman R. L., "Study of advancing interface .1. Interface shape in liquid-gas systems", *J. Colloid Interface Sci.*, **50** (1975) 228-241.

[31] Strom G., Fredriksson M., Stenius P., and Radoev B., "Kinetics of steady-state wetting", *Journal of Colloid and Interface Science*, **134** (1990) 107-116.

[32] Seebergh J. E. and Berg J. C., "Dynamic wetting in the low capillary number regime", *Chemical Engineering Science*, **47** (1992) 4455-4464.

[33] Dussan V. E. B., *On the spreading of liquids on solid surfaces: Static and dynamic contact lines*, in *Annual review of fluid mechanics*1979. p. 371-400.

[34] Blake T. D. and Haynes J. M., "Kinetics of liquid/liquid displacement", *Journal of Colloid and Interface Science*, **30** (1969) 421-423.

[35] Ju-xing Y., Koplik J., and Banavar J. R., "Molecular dynamics of drop spreading on a solid surface", *Physical Review Letters*, **67** (1991) 3539-3542.

[36] Elliott G. E. P. and Riddifor.Ac, "Dynamic contact angles .1. Effect of impressed motion", *Journal of Colloid and Interface Science*, **23** (1967) 389-398.

[37] Cox R. G., "The dynamics of the spreading of liquids on a solid-surface .1. Viscous-flow", *Journal of Fluid Mechanics*, **168** (1986) 169-194.

[38] Huh C. and Scriven L. E., "Hydrodynamic model of steady movement of a solid/liquid/fluid contact line", *Journal of Colloid and Interface Science*, **35** (1971) 85-101.

[39] Dussan E. B. and Davis S. H., "On the motion of a fluid-fluid interface along a solid surface", *Journal of Fluid Mechanics*, **65** (1974) 71-95.

[40] Hocking L. M., "Sliding and spreading of thin 2d drops", *Quarterly Journal of Mechanics and Applied Mathematics*, **34** (1981) 37-55.

[41] Haley P. J. and Miksis M. J., "The effect of the contact line on droplet spreading", *Journal of Fluid Mechanics*, **223** (1991) 57-81.

[42] Hoang A. and Kavehpour H. P., "Dynamics of nanoscale precursor film near a moving contact line of spreading drops", *Physical Review Letters*, **106** (2011)

[43] Heslot F., Cazabat A. M., and Levinson P., "Dynamics of wetting of tiny drops - ellipsometric study of the late stages of spreading", *Physical Review Letters*, **62** (1989) 1286-1289.

[44] Kavehpour H. P., Ovryn B., and McKinley G. H., "Microscopic and macroscopic structure of the precursor layer in spreading viscous drops", *Physical Review Letters*, **91** (2003)

[45] Degennes P. G., "Wetting - statics and dynamics", *Reviews of Modern Physics*, **57** (1985) 827-863.

[46] Bou Zeid W. and Brutin D., "Influence of relative humidity on spreading, pattern formation and adhesion of a drying drop of whole blood", *Colloids and Surfaces A: Physicochemical and Engineering Aspects*, **430** (2013) 1-7.

[47] Marmur A. and Lelah M. D., "The dependence of drop spreading on the size of the solid-surface", *Journal of Colloid and Interface Science*, **78** (1980) 262-265.

[48] Yang Y. and Cho T., "Effect of annealing temperature on the water contact angle of pvd hard coatings", *Materials*, **6** (2013) 3373-3386.

[49] Lelah M. D. and Marmur A., "Wettability of soda-lime glass - effect of cleaning procedures", *American Ceramic Society Bulletin*, **58** (1979) 1121-1124.

[50] Lopez V. H., Kennedy A. R., and Garcia R., "Flux-assisted spreading of an al-7 wt%si alloy on tic", *Journal of Materials Science*, **45** (2010) 4321-4331.

[51] Burelbach J. P., Bankoff S. G., and Davis S. H., "Nonlinear stability of evaporating condensing liquid films", *J. Fluid Mech.*, **195** (1988) 463-494.

[52] Ehrhard P., "Experiments on isothermal and nonisothermal spreading", *J. Fluid Mech.*, **257** (1993) 463-483.

[53] Ehrhard P. and Davis S. H., "Nonisothermal spreading of liquid drops on horizontal plates", *J. Fluid Mech.*, **229** (1991) 365-388.

[54] Krahl R., Gerstmann J., Behruzi P., Bansch E., and Dreyer M. E., "Dependency of the apparent contact angle on nonisothermal conditions", *Physics of Fluids*, **20** (2008)

[55] Kabova Y. O. and Kuznetsov V. V., "Downward flow of a nonisothermal thin liquid film with variable viscosity", *Journal of Applied Mechanics and Technical Physics*, **43** (2002) 895-901.

[56] Schiaffino S. and Sonin A. A., "On the theory for the arrest of an advancing molten contact line on a cold solid of the same material", *Phys. Fluids*, **9** (1997) 2227-2233.

[57] Ajaev V. S. and Davis S. H., "Boundary-integral simulations of containerless solidification", *J. Comput. Phys.*, **187** (2003) 492-503.

[58] Ajaev V. S. and Davis S. H., "The effect of tri-junction conditions in droplet solidification", *J. Cryst. Growth*, **264** (2004) 452-462.

[59] Bennett T. and Poulikakos D., "Heat-transfer aspects of splat-quench solidification - modeling and experiment", *J. Mater. Sci.*, **29** (1994) 2025-2039.

[60] Madejski J., "Solidification of droplets on a cold surface", *Int. J. Heat Mass Transfer*, **19** (1976) 1009-1013.

[61] Pasandideh-Fard M., Bhola R., Chandra S., and Mostaghimi J., "Deposition of tin droplets on a steel plate: Simulations and experiments", *Int. J. Heat Mass Transfer*, **41** (1998) 2929-2945.

[62] Watanabe T., Kuribayashi I., Honda T., and Kanzawa A., "Deformation and solidification of a droplet on a cold substrate", *Chemical Engineering Science*, **47** (1992) 3059-3065.

[63] Haferl S., Butty V., Poulikakos D., Giannakouros J., Boomsma K., Megaridis C. M., and Nayagam V., "Freezing dynamics of molten solder droplets impacting onto flat substrates in reduced gravity", *International Journal of Heat and Mass Transfer*, **44** (2001) 3513-3528.

[64] Attinger D., Zhao Z., and Poulikakos D., "An experimental study of molten microdroplet surface deposition and solidification: Transient behavior and wetting angle dynamics", *J. of Heat Transf.*, **122** (2000) 544-556.

[65] Schiaffino S. and Sonin A. A., "Motion and arrest of a molten contact line on a cold surface: An experimental study", *Phys. Fluids*, **9** (1997) 2217-2226.

[66] Bhola R. and Chandra S., "Parameters controlling solidification of molten wax droplets falling on a solid surface", *J. Mater. Sci.*, **34** (1999) 4883-4894.

[67] Fukanuma H. and Ohmori A. *Behavior of molten droplets impinging on flat surfaces*. in *Proceedings of the 7th National Thermal Spray Conference*. 1994. Boston, Massachusetts.

[68] Li R., Ashgriz N., Chandra S., and Andrews J. R., "Solidification contact angles of molten droplets deposited on solid surfaces", *J. Mater. Sci.*, **42** (2007) 9511-9523.

[69] Smith W. R., "The propagation and basal solidification of two-dimensional and axisymmetric viscous gravity currents", *Journal of Engineering Mathematics*, **50** (2004) 359-378.

[70] Bunk M. A. and King J. R., "Spreading melts with basal solidification", *Zeitschrift Fur Angewandte Mathematik Und Mechanik*, **83** (2003) 820-843.

[71] Zadrazil A., Stepanek F., and Matar O. K., "Droplet spreading, imbibition and solidification on porous media", *Journal of Fluid Mechanics*, **562** (2006) 1-33.

[72] Duthaler G. M., *Molten drop deposition and the dynamics of the molten contact line*, 1999, Massachusetts Institute of Technology. p. 161.

[73] Wang G. X. and Matthys E. F., "Experimental investigation of interfacial thermal conductance for molten metal solidification on a substrate", *Journal of Heat Transfer-Transactions of the Asme*, **118** (1996) 157-163.

[74] Liu W., Wang G. X., and Matthys E. F., "Thermal analysis and measurements for a molten metal drop impacting on a substrate: Cooling, solidification and heat transfer coefficient", *International Journal of Heat and Mass Transfer*, **38** (1995) 1387 - 1395.

[75] Nagashio K., Murata H., and Kuribayashi K., "Spreading and solidification behavior of molten si droplets impinging on substrates", *Acta Materialia*, **52** (2004) 5295-5301.

[76] Nagashio K., Kodaira K., Kuribayashi K., and Motegi T., "Spreading and solidification of a highly undercooled y3al5o12 droplet impinging on a substrate", *International Journal of Heat and Mass Transfer*, **51** (2008) 2455-2461.

[77] Sharma S. D. and Sagara K., "Latent heat storage materials and systems: A review", *International Journal of Green Energy*, **2** (2005) 1-56.

[78] Bessieres D., Saint-Guirons H., and Daridon J. L., "Thermodynamic properties of liquid n-pentadecane", *Physics and Chemistry of Liquids*, **39** (2001) 301-313.

[79] Duan Q., Tan F. L., and Leong K. C., "A numerical study of solidification of n-hexadecane based on the enthalpy formulation", *Journal of Materials Processing Technology*, **120** (2002) 249-258.

[80] Khasanshin T. S., Shchamialiou A. P., and Poddubskij O. G., "Thermodynamic properties of heavy n-alkanes in the liquid state: N-dodecane", *International Journal of Thermophysics*, **24** (2003) 1277-1289.

[81] Incropera F. P., Dewitt D. P., Bergman T. L., and Lavine A. S., *Introduction to heat transfer*. 5th ed, 2007: John Wiley and Sons.

[82] Wang M.-J., Lin F.-H., Hung Y.-L., and Lin S.-Y., "Dynamic behaviors of droplet impact and spreading: Water on five different substrates", *Langmuir*, **25** (2009) 6772-6780.

[83] Starov V. M., Holdich R., Prokopovich P., Njobuenwu D. O., Rubio R. G., Zhdanov S., and Velarde M. G., "Spreading of liquid drops from a liquid source", *Colloids and Surfaces A (Physicochemical and Engineering Aspects)*, **282-283** (2006) 247-55.

[84] Griffiths R. W. and Fink J. H., "Solidifying bingham extrusions: A model for the growth of silicic lava domes", *Journal of Fluid Mechanics*, **347** (1997) 13-36.

[85] Anderson D. M. and Davis S. H., "Local fluid and heat flow near contact lines", *J. Fluid Mech.*, **268** (1994) 231-265.

[86] Anderson D. M., Forest M. G., and Superfine R., "A model for a spreading and melting droplet on a heated substrate", *Siam Journal on Applied Mathematics*, **61** (2001) 1502-1525.

[87] Anderson D. M. and Davis S. H., "Fluid-flow, heat-transfer, and solidification near tri-junctions", *Journal of Crystal Growth*, **142** (1994) 245-252.

[88] Bhardwaj R., *A numerical study of droplet deposition on a solid substrates*, 2006, Stony Brook University.

[89] Mills A. F., *Heat transfer*. 2nd ed, 1998: Prentice Hall Inc.

[90] Sivakumar D. and Nishiyama H., "Spreading and solidification of a molten metal droplet impinging on a heated surface", *Int. J. Heat Mass Tran.*, **47** (2004) 4469-4478.

[91] Bouchard D., Leboeuf S., Nadeau J.-P., Guthrie R. I. L., and Isac M., "Dynamic wetting and heat transfer at the initiation of aluminum solidification on copper substrates", *J. Mater. Sci.*, **44** (2009) 1923-1933.

[92] Yarin A. L., *Drop impact dynamics: Splashing, spreading, receding, bouncing*, in *Annual review of fluid mechanics*2006. p. 159-192.

[93] Bartell L. S. and Huang J., "Supercooling of water below the anomalous range near 226 k", *J. Phys. Chem.*, **98** (1994) 7455-7457.

[94] Lee S. and Bragg M. B., "Investigation of factors affecting iced-airfoil aerodynamics", *Journal of Aircraft*, **40** (2003) 499-508.

[95] Parent O. and Ilinca A., "Anti-icing and de-icing techniques for wind turbines: Critical review", *Cold Regions Science and Technology*, **65** (2011) 88-96.

[96] Dutta P. K., Ryerson C. C., and Pergantis C., *Thermal deicing of polymer composite helicopter blades*, in *Materials for space applications*, M. Chipara, et al., Editors. 2005, Materials Research Society: Warrendale. p. 563-574.

[97] Cao L. L., Jones A. K., Sikka V. K., Wu J. Z., and Gao D., "Anti-icing superhydrophobic coatings", *Langmuir*, **25** (2009) 12444-12448.

[98] Liang G., Guifu D., Hong W., Jinyuan Y., Ping C., and Yan W., "Anti-icing property of superhydrophobic octadecyltrichlorosilane film and its ice adhesion strength", *Journal of Nanomaterials*, (2013) 278936 (5 pp.)-278936 (5 pp.).

[99] Croutch V. K. and Hartley R. A., "Adhesion of ice to coatings and the perfomance of ice release coatings", *Journal of Coatings Technology*, **64** (1992) 41-53.

[100] Li K. Y., Xu S., Shi W. X., He M., Li H. L., Li S. Z., Zhou X., Wang J. J., and Song Y. L., "Investigating the effects of solid surfaces on ice nucleation", *Langmuir*, **28** (2012) 10749-10754.

[101] Tourkine P., Le Merrer M., and Quere D., "Delayed freezing on water repellent materials", *Langmuir*, **25** (2009) 7214-7216.

[102] He M., Wang J., Li H., Jin X., Wang J., Liu B., and Song Y., "Super-hydrophobic film retards frost formation", *Soft Matter*, **6** (2010) 2396-2399.

[103] Jung S., Dorrestijn M., Raps D., Das A., Megaridis C. M., and Poulikakos D., "Are superhydrophobic surfaces best for icephobicity?", *Langmuir*, **27** (2011) 3059-3066.

[104] Jung S., Tiwari M. K., Doan N. V., and Poulikakos D., "Mechanism of supercooled droplet freezing on surfaces", *Nature Communications*, **3** (2012) 1-8.

[105] Varanasi K. K., Deng T., Smith J. D., Hsu M., and Bhate N., "Frost formation and ice adhesion on superhydrophobic surfaces", *Applied Physics Letters*, **97** (2010)

[106] Hao W., Liming T., Xiaomin W., Wantian D., and Yipeng Q., "Fabrication and anti-frosting performance of super hydrophobic coating based on modified nano-sized calcium carbonate and ordinary polyacrylate", *Applied Surface Science*, **253** (2007) 8818-8824.

[107] Singh D. P. and Singh J. P., "Delayed freezing of water droplet on silver nanocolumnar thin film", *Applied Physics Letters*, **102** (2013)

[108] Alizadeh A., Yamada M., Li R., Shang W., Otta S., Zhong S., Ge L., Dhinojwala A., Conway K. R., Bahadur V., Vinciquerra A. J., Stephens B., and Blohm M. L., "Dynamics of ice nucleation on water repellent surfaces", *Langmuir*, **28** (2012) 3180-3186.

[109] Meuler A. J., McKinley G. H., and Cohen R. E., "Exploiting topographical texture to impart icephobicity", *Acs Nano*, **4** (2010) 7048-7052.

[110] Bahadur V., Mishchenko L., Hatton B., Taylor J. A., Aizenberg J., and Krupenkin T., "Predictive model for ice formation on superhydrophobic surfaces", *Langmuir*, **27** (2011) 14143-14150.

[111] Kulinich S. A., Farhadi S., Nose K., and Du X. W., "Superhydrophobic surfaces: Are they really ice-repellent?", *Langmuir*, **27** (2011) 25-29.

[112] Guo Z. G., Liu W. M., and Su B. L., "Superhydrophobic surfaces: From natural to biomimetic to functional", *Journal of Colloid and Interface Science*, **353** (2011) 335-355.

[113] Porter D. A. and Easterling K. E., *Phase transformations in metals and alloys*, 1981: Van Nostrand Reinhold (UK) Co. Ltd.

[114] Toschev S. and Gutzow I., "Time lag in heterogeneous nucleation due to nonstationary effects", *Physica Status Solidi*, **21** (1967) 683-691.

[115] Davies H. A. and Hull J. B., "Non-crystalline phase in splat-quenched germanium", *Scr. Metall.*, **7** (1973) 637-641.

[116] Davies H. A., Aucote J., and Hull J. B., "Amorphous nickel produced by splat quenching", *Nature-Physical Science*, **246** (1973) 13-14.

[117] Windhab E. J., "New developments in crystallization processing", *J. Therm. Anal. Calorim.*, **57** (1999) 171-180.

[118] Hindmarsh J. P., Russell A. B., and Chen X. D., "Experimental and numerical analysis of the temperature transition of a suspended freezing water droplet", *Int. J. Heat Mass Transfer*, **46** (2003) 1199-1213.

[119] Macklin W. C. and Ryan B. F., "Structure of ice grown in bulk supercooled water", *J. Atmos. Sci.*, **22** (1965) 452-459.

[120] Hindmarsh J. P., Wilson D. I., and Johns M. L., "Using magnetic resonance to validate predictions of the solid fraction formed during recalescence of freezing drops", *Int. J. Heat Mass Transfer*, **48** (2005) 1017-1021.

[121] Bauerecker S., Ulbig P., Buch V., Vrbka L., and Jungwirth P., "Monitoring ice nucleation in pure and salty water via high-speed imaging and computer simulations", *J. Phys. Chem. C*, **112** (2008) 7631-7636.

[122] Gurganus C., Kostinski A. B., and Shaw R. A., "Fast imaging of freezing drops: No preference for nucleation at the contact line", *J. Phys. Chem. Lett.*, **2** (2011) 1449-1454.

[123] Libbrecht K. G., "The physics of snow crystals", *Rep. Prog. Phys.*, **68** (2005) 855-895.

[124] Djikaev Y. S. and Ruckenstein E., "Thermodynamics of heterogeneous crystal nucleation in contact and immersion modes", *J. Phys. Chem. A*, **112** (2008) 11677-11687.

[125] Suzuki S., Nakajima A., Yoshida N., Sakai M., Hashimoto A., Kameshima Y., and Okada K., "Freezing of water droplets on silicon surfaces coated with various silanes", *Chem. Phys. Lett.*, **445** (2007) 37-41.

[126] Duft D. and Leisner T., "Laboratory evidence for volume-dominated nucleation of ice in supercooled water microdroplets", *Atmospheric Chemistry and Physics*, **4** (2004) 1997-2000.

[127] Snoeijer J. H. and Brunet P., "Pointy ice-drops: How water freezes into a singular shape", *Am. J. Phys.*, **80** (2012) 764-771.

[128] Sanz A., Meseguer J., and Mayo L., "The influence of gravity on the solidification of a drop", *J. Cryst. Growth*, **82** (1987) 81-88.

[129] Enriquez O. R., Marin A. G., Winkels K. G., and Snoeijer J. H., "Freezing singularities in water drops", *Physics of Fluids*, **24** (2012.)

[130] Schultz W. W., Worster M. G., and Anderson D. M., *Solidifying sessile water droplets*, in *Interactive dynamics of convection and solidification*, P. Ehrhard, D.S. Riley, and P.H. Steen, Editors. 2001, Kluwer Academic Publishers p. 209-226.

[131] Blanchard D. *The supercooling, freezing and melting of giant water drops at terminal velocity in air*. in *Artificial Stimulation of Rain Proceedings of the First Conference on the Physics of Clouds and Precipitation Particles*. 1955. New York: Pergamon Press.

[132] Eckler K. and Herlach D. M., "Measurements of dendrite growth velocities in undercooled pure ni-melts - some new results", *Mater. Sci. Eng., A*, **178** (1994) 159-162.

[133] Camp P. R., "Formation of ice at water-solid interfaces", *Annals of the New York Academy of Sciences*, **125** (1965) 317-343.

[134] Shibkov A. A., Golovin Y. I., Zheltov M. A., Korolev A. A., and Leonov A. A., "Morphology diagram of nonequilibrium patterns of ice crystals growing in supercooled water", *Physica a-Statistical Mechanics and Its Applications*, **319** (2003) 65-79.

[135] Zhu S., Miller W. G., Scriven L. E., and Davis H. T., "Superspreading of water-silicone surfactant on hydrophobic surfaces", *Colloids and Surfaces a-Physicochemical and Engineering Aspects*, **90** (1994) 63-78.

[136] Hill R. M., "Superspreading", *Current Opinion in Colloid & Interface Science*, **3** (1998) 247-254.

[137] Chengara A., Nikolov A., and Wasan D., "Surface tension gradient driven spreading of trisiloxane surfactant solution on hydrophobic solid", *Colloids and Surfaces a-Physicochemical and Engineering Aspects*, **206** (2002) 31-39.

[138] Lim H. S., Han J. T., Kwak D., Jin M. H., and Cho K., "Photoreversibly switchable superhydrophobic surface with erasable and rewritable pattern", *Journal of the American Chemical Society*, **128** (2006) 14458-14459.

[139] Li C., Guo R. W., Jiang X., Hu S. X., Li L., Cao X. Y., Yang H., Song Y. L., Ma Y. M., and Jiang L., "Reversible switching of water-droplet mobility on a superhydrophobic surface based on a phase transition of a side-chain liquid-crystal polymer", *Advanced Materials*, **21** (2009) 4254-4258.

[140] Hong X., Gao X. F., and Jiang L., "Application of superhydrophobic surface with high adhesive force in no lost transport of superparamagnetic microdroplet", *Journal of the American Chemical Society*, **129** (2007) 1478-1479.

[141] Mugele F. and Baret J. C., "Electrowetting: From basics to applications", *Journal of Physics-Condensed Matter*, **17** (2005) 705-774.

[142] Sun T. L., Wang G. J., Feng L., Liu B. Q., Ma Y. M., Jiang L., and Zhu D. B., "Reversible switching between superhydrophilicity and superhydrophobicity", *Angewandte Chemie-International Edition*, **43** (2004) 357-360.

[143] Crevoisier G. B., Fabre P., Corpart J. M., and Leibler L., "Switchable tackiness and wettability of a liquid crystalline polymer", *Science*, **285** (1999) 1246-1249.

[144] Huang L. Y., Liu Z. L., Liu Y. M., Gou Y. J., and Wang L., "Effect of contact angle on water droplet freezing process on a cold flat surface", *Experimental Thermal and Fluid Science*, **40** (2012) 74-80.

[145] Mobarakeh L. F., Jafari R., and Farzaneh M., "The ice repellency of plasma polymerized hexamethyldisiloxane coating", *Applied Surface Science*, **284** (2013) 459-463.

[146] Dotan A., Dodiuk H., Laforte C., and Kenig S., "The relationship between water wetting and ice adhesion", *Journal of Adhesion Science and Technology*, **23** (2009) 1907-1915.

[147] Meuler A. J., Smith J. D., Varanasi K. K., Mabry J. M., McKinley G. H., and Cohen R. E., "Relationships between water wettability and ice adhesion", *Acs Applied Materials & Interfaces*, **2** (2010) 3100-3110.

[148] Mockenhaupt B., Ensikat H. J., Spaeth M., and Barthlott W., "Superhydrophobicity of biological and technical surfaces under moisture condensation: Stability in relation to surface structure", *Langmuir*, **24** (2008) 13591-13597.

[149] Wang F. C., Li C. R., Lv Y. Z., Lv F. C., and Du Y. F., "Ice accretion on superhydrophobic aluminum surfaces under low-temperature conditions", *Cold Regions Science and Technology*, **62** (2010) 29-33.

[150] Lelah M. D. and Marmur A., "Spreading kinetics of drops on glass", *Journal of Colloid and Interface Science*, **82** (1981) 518-525.

[151] Nilsson M. A., Daniello R. J., and Rothstein J. P., "A novel and inexpensive technique for creating superhydrophobic surfaces using teflon and sandpaper", *Journal of Physics D-Applied Physics*, **43** (2010)

[152] Perez E., Schaffer E., and Steiner U., "Spreading dynamics of polydimethylsiloxane drops: Crossover from laplace to van der waals spreading", *Journal of Colloid and Interface Science*, **234** (2001) 178-193.

[153] Grimaldi A., George M., Pallares G., Marliere C., and Ciccotti M., "The crack tip: A nanolab for studying confined liquids", *Physical Review Letters*, **100** (2008)

[154] Ciccotti M., George M., Ranieri V., Wondraczek L., and Marliere C., "Dynamic condensation of water at crack tips in fused silica glass", *Journal of Non-Crystalline Solids*, **354** (2008) 564-568.

[155] Machin W. D., "Capillary condensation of hexafluoroethane in an ordered mesoporous silica", *Physical Chemistry Chemical Physics*, **5** (2003) 203-207.

[156] Pellenq R. J. M. and Levitz P. E., "Capillary condensation in a disordered mesoporous medium: A grand canonical monte carlo study", *Molecular Physics*, **100** (2002) 2059-2077.

[157] Chen Y. C., Zhao Y. Z., Gao H. L., and Zheng J. Y., "Liquid bridge force between two unequal-sized spheres or a sphere and a plane", *Particuology*, **9** (2011) 374-380.

[158] Tas N., Sonnenberg T., Jansen H., Legtenberg R., and Elwenspoek M., "Stiction in surface micromachining", *Journal of Micromechanics and Microengineering*, **6** (1996) 385-397.

[159] Ciccotti M., "Stress-corrosion mechanisms in silicate glasses", *Journal of Physics D-Applied Physics*, **42** (2009)

[160] German R. M., *Powder metallurgy and particulate materials processing*, 2005: Metal Powder Industries Federation.

[161] Gemici Z., *Effects and applications of capillary condensation in ultrathin nanoparticle assemblies*, 2010, Cornell University. p. 182.

[162] Dijkstra M., "Capillary freezing or complete wetting of hard spheres in a planar hard slit?", *Physical Review Letters*, **93** (2004)

[163] Tselishchev Y. G. and Val'tsifer V. A., "Influence of the type of contact between particles joined by a liquid bridge on the capillary cohesive forces", *Colloid Journal*, **65** (2003) 385-389.

[164] Zargarzadeh L. and Elliott J. A. W., "Comparative surface thermodynamic analysis of new fluid phase formation between a sphere and a flat plate", *Langmuir*, **29** (2013) 3610-3627.